Blooming Boundaries
Zooming in on Plant-Atmosphere Energy Exchange

Boekee, J.

DOI
10.4233/uuid:7b3820e4-dd27-4c15-81ce-385da8b9d222

Publication date
2026

Document Version
Final published version

Citation (APA)
Boekee, J. (2026). *Blooming Boundaries: Zooming in on Plant-Atmosphere Energy Exchange*. [Dissertation (TU Delft), Delft University of Technology]. https://doi.org/10.4233/uuid:7b3820e4-dd27-4c15-81ce-385da8b9d222

Blooming Boundaries

Zooming in on Plant-Atmosphere Energy Exchange

J. Jongen-Boekee

BLOOMING BOUNDARIES

ZOOMING IN ON PLANT-ATMOSPHERE ENERGY EXCHANGE

BLOOMING BOUNDARIES

ZOOMING IN ON PLANT-ATMOSPHERE ENERGY EXCHANGE

Dissertation

for the purpose of obtaining the degree of doctor
at Delft University of Technology,
by the authority of the Rector Magnificus prof. dr. ir. H. Bijl,
chair of the Board of Doctorates,
to be defended publicly on
Thursday 29 January 2026 at 12:30

by

Judith JONGEN - BOEKEE

Master of Science in Earth and Environment,
Wageningen University and Research, Wageningen, The Netherlands,
born in Roosendaal, The Netherlands.

This dissertation has been approved by the promotors.

Composition of the doctoral committee:

Rector Magnificus,	chairperson
Dr. ir. J. A. E. ten Veldhuis	Delft University of Technology, promotor
Prof. dr. ir. B. J. H. van de Wiel	Delft University of Technology, copromotor
Independent members:	
Dr. ir. A. M. J. Coenders	Delft University of Technology
Prof. dr. H. J. J. Jonker	Delft University of Technology
Prof. dr. ir. N. C. van de Giesen	Delft University of Technology
Prof. dr. J. Vilà-Guerau de Arellano	Wageningen University & Research
Dr. J. P. Londo	Cornell University, United States of America

The author received financial support from the Netherlands Organization for Scientific Research (NWO) project EN-WSS.2018.006 with Prof. dr. ir. B.J.H. van de Wiel as principal investigator.

Keywords: atmosphere, vegetation, frost, atmospheric surface layer

Printed by: ProefschriftMaken

Front & Back: Judith Jongen - Boekee

DOI 10.4233/uuid:7b3820e4-dd27-4c15-81ce-385da8b9d222

An electronic version of this dissertation is available at
http://repository.tudelft.nl/record/uuid:7b3820e4-dd27-4c15-81ce-385da8b9d222

"Everyone here is smart,
distinguish yourself by being kind"

Emily Bernhardt, *Nature* (2016)

CONTENTS

SUMMARY

This dissertation addresses the challenge of spring frost damage in fruit orchards. Frost events during the growing season can cause significant damage to blossoms and young fruit, leading to substantial yield losses. The study evaluates two protective strategies to mitigate such damage: 1) the use of wind machines and 2) the manipulation of surface vegetation. Both approaches are investigated through experimental observations and conceptual modelling.

During a frost night, the surface cools radiatively, creating a stable stratified layer of cold air between the fruit trees. In Chapter 2 , we investigate how wind machines break down this stratification. Wind machines generate a jet that mixes warm overlying air down to the vegetation and erodes the leaf boundary layer.

Using a grid of fibre optic cables, we demonstrated that the foliage reduces the jet penetration to the ground. Multiple rotations (~ 15) were needed to reach optimal mixing, and only the upper 30% – 60% of the canopy layer was well-mixed, depending on the distance to the wind machine. As the foliage becomes denser throughout the season, these effects become stronger.

Over every rotation cycle, leaves that radiatively cooled below air temperature are warmed up to air temperature, as strong convective warming repeatedly dominates over radiative cooling. Thinner flower petals closely follow air temperature, in contrast to thicker shoots that show a strongly dampened response, as they act as heat reservoirs and retain warmth from daytime heating.

However, below-zero plant temperatures are not per se lethal to plant organs. Frost damage results from extracellular ice formation, which increases solute concentration outside the cells and drives water out, causing severe dehydration and potential cell death. Whether a flower or bud survives depends on the extent of damage to vital tissues and the regenerative capacity of remaining cells.

In Chapter 3, we explore the potential of using thermal cameras to detect freezing events for field applications, by measuring the exotherm released as ice crystals form. The temperatures at which damage occurs are currently determined under controlled conditions in cold chambers. These chambers are not always representative of the outside conditions. We show that thermal cameras have a high potential for in situ monitoring and can thus be applied to study frost formation during actual frost conditions in the field.

Since the cooling originates at the surface, another frost mitigation technique is to suppress the surface cooling. An airy cover crop works as an isolator, limiting energy exchange between air and soil. Growers therefore often keep the grass short to enhance energy release at night. To understand the effect of grass height in an orchard setting, we must first understand the effect of grass height in an open field. This is the topic of Chapter 4.

Using distributed temperature sensing (DTS) cables, we record temperature gradients within and above the grass layer, revealing a transition from classical logarithmic profiles to near-linear behaviour within the lowest 1 – 2 m above the surface. Inspired by the Van Driest formulation for velocity gradients over smooth surfaces, we derive an analogous temperature-gradient model that introduces a length scale tied directly to vegetation dimensions. The model provides an improved, more robust description of near-surface temperature profiles above the vegetation canopy.

An accurate description of the conditions near the surface is not only important for surface sensible heat fluxes, but also for predictions of the surface latent heat fluxes. In Chapter 5 the Penman-Monteith (PM) model, widely used for estimating evaporation, is evaluated against long-term eddy covariance (EC) data from grassland and forest sites.

PM tends to overestimate evaporation under high radiation, temperature, and low humidity. Possible explanations include EC underestimation of high fluxes, inadequate representation of leaf-level processes (e.g., stomatal behaviour and leaf boundary layer conductance), and the model's omission of canopy-atmosphere decoupling.

The findings of this thesis highlight the importance of considering air-vegetation interactions for both applied and fundamental research. In 'complex' fruit orchards, cover crops alter ground-atmosphere energy exchange, while tree rows can block air flow and create thick leaf boundary layers. Varying leaf shape, organ thickness, and water content determine variations in thermal inertia, while freeze tolerance changes through the seasons, leading to spatially and temporally changing frost risk. Above 'simple' grass canopies, surface energy transport is often modelled too simplistically. Grass too, disrupts and blocks air flow, and has strong thermal insulation effects. Neglecting to consider this results in erroneous surface temperature estimates, and can translate into disagreement between evapotranspiration models and measurements.

These insights emphasise that vegetation is far from a passive backdrop, but actively governs microclimate and surface processes. Recognising this may improve crop protection from both abiotic and biotic stresses, support more sustainable agriculture, and help to meet the rising food demand in a changing world.

SAMENVATTING

Dit proefschrift gaat over vorstschade in fruitboomgaarden. Nachtvorst tijdens het groeiseizoen kan leiden tot aanzienlijke schade aan bloemknoppen en jonge vruchten, wat een directe impact heeft op de opbrengst en kwaliteit van het fruit. In dit onderzoek richten we ons op twee methoden om deze schade te beperken: 1) het gebruik van windmachines en 2) het "manipuleren"van de bodembedekkers. Daarbij maken we gebruik van zowel veldexperimenten als conceptuele modellen.

Tijdens een vorstnacht koelt het oppervlak af door uitgaande langgolvige straling. Dit creëert een stabiele koude luchtlaag die tussen de bomen blijft hangen. In hoofdstuk 2 onderzoeken we hoe windmachines deze stabiele laag afbreken. Een windmachine genereert een sterke luchtstroming, een zogenoemde jet, die ervoor zorgt dat de relatieve warme lucht die boven de bomen hangt, wordt gemengd met de koude lucht tussen de bomen. Hierdoor warmt de lucht rondom de kwetsbare bloesem dus op. Daarnaast zorgt deze jet ervoor dat de grenslaag rondom de bloemen en bladeren wordt weg geërodeerd.

Met een raster van temperatuurmetingen langs glasvezelkabels hebben we laten zien dat het gebladerte de jet blokkeert. Meerdere rotaties van de windmachine waren nodig om de lucht maximaal te mengen, en slechts de bovenste 30–60% van de lucht in de vegetatie werd goed gemengd, afhankelijk van de afstand tot de windmachine. Door het groeiseizoen heen werd dit effect sterker, aangezien er meer en groter blad aan de bomen kwam.

Daarnaast hebben we laten zien dat de bladeren kouder worden dan de lucht door langgolvige stralingskoeling. Tijdens een rotatie van de machine warmen de bladeren op tot luchttemperatuur en koelen vervolgens weer af. Dit is anders voor bloemen, die met hun dunne blaadjes de luchttemperatuur nauw volgen. Dikke takken daarentegen houden nog warmte vast van de dag en blijven daardoor relatief warm.

Dat de temperatuur van de plant onder nul komt, betekent niet dat er ook direct schade zal optreden. Vorstschade is het gevolg van ijsvorming buiten de cellen. Hierdoor nemen zout- en suikerconcentraties buiten de cellen toe, en wordt water door osmose uit de cellen getrokken. De hierop volgende uitdroging kan dodelijk zijn voor de cellen. Of dit ook tot het afsterven van de bloemen leidt, hangt af van de locatie van de uitdroging en het herstellend vermogen van de omringende cellen.

In hoofdstuk 3 verkennen we de mogelijkheden voor het gebruik van thermische camera's om bevriezing te detecteren onder veld condities. Hierbij meten we de warmtepiek die vrijkomt als water bevriest. Bij welke temperatuur schade optreedt, wordt normaal gesproken gemeten onder gecontroleerde omstandigheden in een laboratorium. De omstandigheden in deze koelcellen zijn echter niet direct vergelijkbaar met die in het veld. Thermische camera's lijken een aantrekkelijk alternatief om vorst in het veld te onderzoeken.

Aangezien de vorst ontstaat aan de grond, kan vorstschade ook beperkt worden door de oppervlaktekoeling te beperken. Een vegetatielaag kan werken als een soort deken

op de bodem (een isolatielaag) en beperkt de warmte-uitwisseling tussen de bodem en de lucht. Fruittelers houden daarom vaak het gras kort in het voorjaar, om te zorgen dat zoveel mogelijk warmte die overdag wordt opgeslagen in de bodem, ’s nachts weer vrijkomt. Om te begrijpen of dit inderdaad een effectieve methode is in boomgaarden, bestuderen we eerst het effect van grashoogte in een open veld.

In hoofdstuk 4 gebruiken we glasvezelkabel om de temperatuurgradiënten boven en in het gras te meten. Hiermee ontdekten we een overgang van het klassieke logaritmische naar een lineair profiel in de onderste 1 tot 2 meter vanaf het oppervlak. Geïnspireerd door de Van Driest-vergelijking voor stroming over een glad oppervlak, ontwikkelden we een gelijksoortig model voor de temperatuurprofielen boven een ruw (vegetatie) oppervlak. Dit model introduceert een lengteschaal die direct aan de grasdimensies kan worden gelinkt.

Een betere beschrijving van de temperatuur boven gras is niet alleen belangrijk voor de uitwisseling van sensibele, maar ook van latente warmte. In hoofdstuk 5 vergelijken we het Penman-Monteith model (PM), een veelgebruikte verdampingsmodels, met eddy-covariantiemetingen boven grasland en bos. Het PM-model overschat vooral bij hoge straling en temperaturen en lage luchtvochtigheid. Mogelijke verklaringen daarvoor zijn een meetfouten en een incorrecte representatie van processen op bladniveau: zoals onverzadigde stomata en een onderschattting van het effect van de bladgrenslaag. Ten slotte, neemt PM ook de mogelijke ontkoppeling tussen de vergetatielaag en de overhangende lucht niet mee. Dit kan vooral bij gras voor grote verschillen zorgen, door de lagere ruwheid ten opzichte van bos.

Dit proefschrift benadrukt dus het belang van vegetatie-atmosfeerinteractie voor zowel toegepast als fundamenteel onderzoek. In ‘complexe’ boomgaarden bepalen bodembedekkers de warmte-uitwisseling tussen bodem en lucht, terwijl de boomrijen de luchtstroming blokkeren en dikke grenslagen zich vormen om bladeren. Bladvorm, dikte en vochtgehalte beïnvloeden de thermische traagheid, terwijl de vorstbestendigheid verandert door de seizoenen. Dit resulteert in variatie in vorstgevoeligheid, zowel in tijd als ruimte. Boven ‘simpele’ grasvelden wordt energie-uitwisseling vaak te sterk versimpeld. Ook gras verstoort en blokkeert luchtstroming. Door dit te negeren, maken we fouten in het bepalen van de oppervlaktetemperatuur. Dit kan zich vervolgens weer vertalen naar fouten in verdampingsmodellen.

Deze inzichten benadrukken dat vegetatie allesbehalve een passieve achtergrond is, maar juist actief het microklimaat en oppervlakteprocessen beïnvloedt. Door dit te erkennen, kunnen we gewassen beter beschermen tegen zowel abiotische als biotische stress, duurzamere landbouw ondersteunen en helpen voldoen aan de groeiende voedselvraag in een veranderende wereld.

1

INTRODUCTION

1.1. PLANT-ENVIRONMENT INTERACTIONS

For organisms to grow and reproduce, they must adapt to their environment. Some microorganisms can thrive in extreme conditions, ranging from -6 °C and 120 °C, and even survive down to -272 °C in their dessicated form (Hopkins, Hüner, et al., 1995). Higher forms of life however, like plants (and humans), have adapted to a relatively narrow range of conditions by evolving physiological responses. When environments change, e.g because of human interference or natural variation, plants may or may not be flexible enough to survive.

However, plants are not merely at the mercy of their environment, they also modify it. The physical stimuli received *from* the environment are partly determined by the physiological response *to* the environment. For example, plants protect themselves from dehydration by limiting water loss during warm and dry conditions (Jarvis, 1976; Stewart, 1988), resulting in even drier air (Van Heerwaarden & Teuling, 2014).

Despite this evolutionary development, natural conditions are often far from optimal. In the agricultural sector, this can result in damage to crops, reduced yields and economic losses. For instance, a late frost in spring can damage young flowers, significantly lowering yields in the fruit and wine industry (Snyder & De Melo-abreu, 2005). A prolonged dry period in summer can stimulate staple crops such as corn to grow fewer flowers, thus producing less seed and lowering harvest (Prasad et al., 2017; Djalovic et al., 2024).

In order to minimise these damages, passive and active protection methods have been developed. To keep up with the growing food demand of the expanding world population and changing environmental conditions due to global warming, we need to improve our understanding of the interaction between plants and their environment.

These interactions are rarely straightforward. The governing physical processes are complex, and physiological mechanisms are often poorly understood. Meteorologists therefore describe these processes in terms of *models*: simplified representations of reality. The art lies in choosing robust approximations that obey physical laws (such as conservation of energy (Châtelet, 1740)[1], mass (Lavoisier, 1789) and momentum (Wallis, 1670)), while still accurately describing the natural world without unnecessary complexity. An example of such a model that will play a central role in this thesis is Ohm's law (Ohm, 1827); which introduces the concept of resistance as a proportionality factor between a driving gradient and the resulting flux. Resistances have been used by plant physiologists as a way of expressing the physical factors that control rates of transpiration. In micrometeorology, aerodynamic resistances are used to describe turbulent water transport from the surface to the atmosphere (Monin & Obukov, 1954; Monteith & Unsworth, 1990).

1.2. ATMOSPHERIC BOUNDARY LAYER

The interaction between the vegetation and the atmosphere happens in the lowest ~1% of the atmosphere, the atmospheric boundary layer (ABL). The ABL typically extends to about 1 km in height, but this can vary strongly in time and space. The atmospheric surface layer (ASL, Figure 1.1) is the lowest 5-10% of the atmospheric boundary layer, extending tens of meters above the surface (Stull, 2012). Here the fluxes differ by less than 10% from their surface values. Surface layer models act as the interface between the land surface and the lowest atmospheric model layer. A thorough understanding of this layer is crucial for accurately simulating near-surface weather conditions, such as temperature, humidity, and wind speed, which directly influence human and ecological systems.

1.2.1. SURFACE ENERGY BALANCE

Energy enters the ASL as radiation (R_n). Atmospheric radiation is usually separated into shortwave (SW) and longwave (LW) radiation, with the divide at a wavelength of 4 μm. SW originates from the sun, while LW is re-emitted by the earth-atmosphere system following its temperature. The net SW is the sum of incoming solar radiation SW_{in} and reflected (outgoing) shortwave radiation $SW_{in} * \alpha$, where α is the surface albedo. Net LW is the sum of the radiation emitted at the surface $LW_{out} = \varepsilon_s \sigma T_s$ and radiation received from the air $LW_{in} = \varepsilon_a \sigma T_a$. Here, σ is the Stefan-Boltzmann constant and ε is the emissivity.

Solar radiation heats the surface during the day, creating a temperature gradient between the warm surface and the cooler air above. This gradient drives an upward sensible heat flux (H). At the same time, energy is transported into the soil (ground heat flux G) and used to evaporate water (latent heat flux (LE)). During nighttime, the situation reverses as the surface cools by emitting longwave radiation. The reversed temperature gradient drives a downward sensible heat flux, energy is transported from the soil to the surface and dew fall can occur. The distribution of this energy is determined by meteorological conditions and surface properties and described by the surface energy balance (Jacobs et al., 2008):

$$(1-\alpha)SW_{in} + \varepsilon_a \sigma T_a - \varepsilon_s \sigma T_s = H + LE + G \tag{1.1}$$

---

[1] Émilie du Châtelet was an 18th-century physicist and mathematician, and unlike many scientists in this time: a woman. Born into a wealthy family, she was well educated by tutors. As she was not allowed to enter university, she continued learning at a later age from the 'clever young men' with whom she maintained intimate relationships. One of these men was Voltaire, who wrote: *'He was a great man whose only fault was being a woman.'* (Fara, 2011).

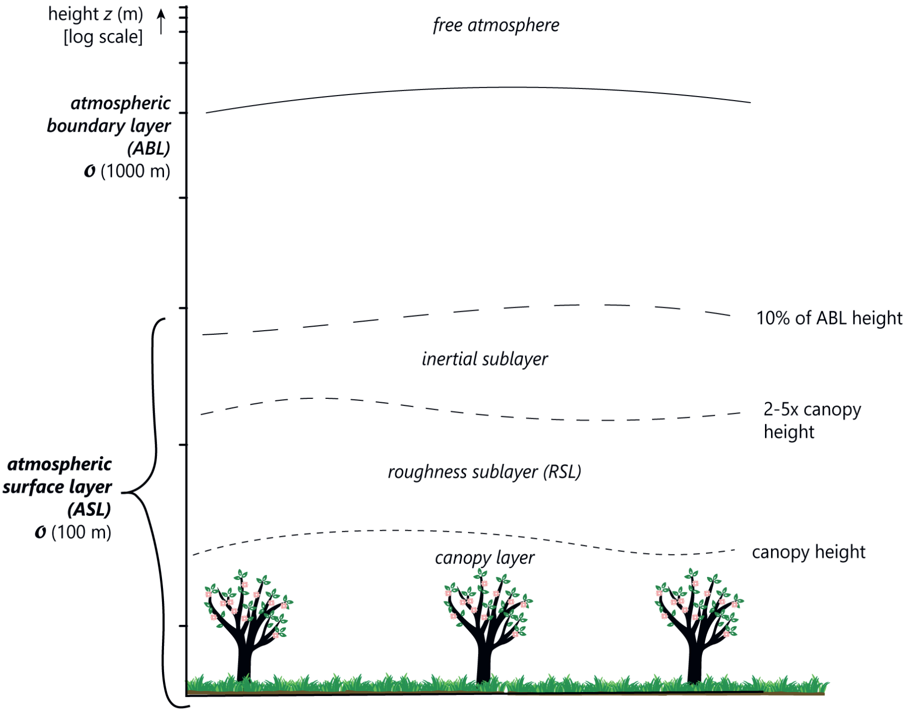

Figure 1.1: Definition of the layers of the atmospheric boundary layer. The vertical axis represents the height, and should be interpreted as a logarithmic scale.

Note that this is a simplified version of the full balance. We neglect advection and smaller terms such as heat storage in vegetation, photosynthetic energy and the reflection of incoming longwave radiation

1.2.2. SURFACE FLUXES

The main transport mechanism in the atmospheric boundary layer is turbulent transport: heat, water vapour (and other gases) as well as momentum are transported by the movement of parcels of air by turbulent eddies (Stull, 2012). Atmospheric turbulence can be generated by two sources: 1) surface friction (i.e. mechanical turbulence) and 2) buoyancy, vertical acceleration of air as a result of density fluctuations (i.e. thermal turbulence) (Rotach & Holtslag, 2025). Surface friction is always a source of turbulence. Buoyancy, however, can increase or dampen turbulence. During the day, the atmosphere is generally *unstable*. Since the surface is heated by solar radiation, the surface warms the air above it. This warm air is buoyant and wants to rise, increasing turbulence. On the other hand, during the night, the surface cools radiatively, cooling the air above it. This dampens turbulence and creates a *stable* atmosphere, with warm air on top of cool air. When these stable nighttime conditions occur during the spring, the cold air near the surface can create dangerous conditions for agricultural crops. This will be discussed in depth in Chapter 2 and 3 of this thesis.

To describe the complex and chaotic behaviour of atmospheric turbulent transport, micrometeorologists draw a parallel with molecular diffusion, where molecules move from high concentrations to low concentrations. Larger gradients therefore result in larger fluxes. These flux-gradient laws result in logarithmic profiles for temperature, moisture and momentum near the surface (Figure 1.2). These shapes and profiles are described by the Monin-Obukhov Similarity Theory (MOST) (Monin & Obukov, 1954; Foken, 2006).

MONIN-OBUKHOV'S SIMILARITY THEORY

It is not possible to derive the relationship between turbulent fluxes and gradients purely from first principles (Rotach & Holtslag, 2025). To overcome this, fluid dynamics often relies on similarity theory, which posits that flows can be considered similar when certain non-dimensional parameters are identical. For ASL flow, this non-dimensional parameter is the stability parameter: $\zeta = z/L$. Here the Obukhov length L is introduced, a scale of the surface layer that expresses the relative importance of shear and buoyancy in turbulent production/consumption (American Meteorological Society, 1959). The central assumption of MOST is that gradients (when made dimensionless through the fluxes) are universal functions of z/L. For example, the dimensionless gradient of potential temperature with height $\left(\frac{\partial\theta}{\partial z}\right)$ corresponding to the dimensionless sensible heat flux is expressed as:

$$\frac{\partial\theta}{\partial z}\frac{\kappa z}{\theta_*} = \phi_h(z/L). \tag{1.2}$$

Similarly, the moisture gradient $\left(\frac{\partial q}{\partial z}\right)$ corresponding to latent heat flux is given by:

$$\frac{\partial q}{\partial z}\frac{\kappa z}{q_*} = \phi_q(z/L). \tag{1.3}$$

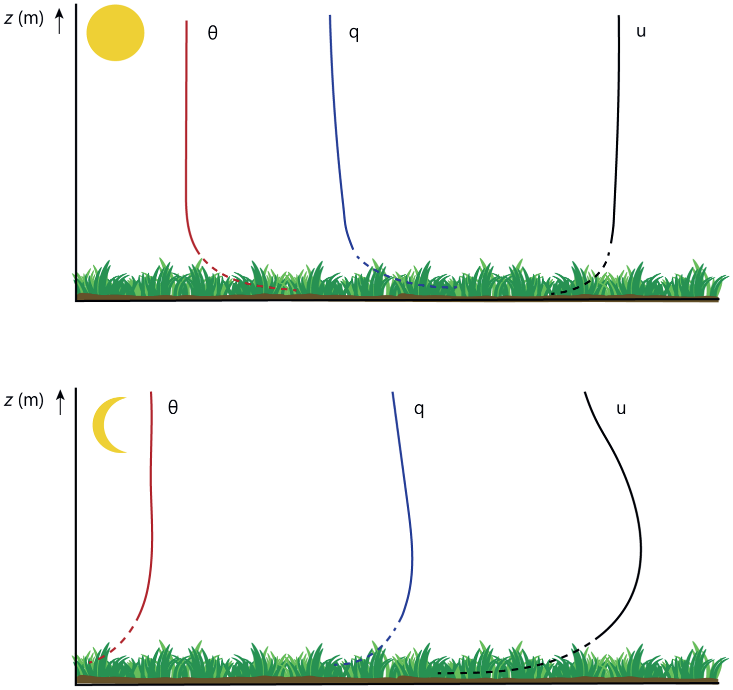

Figure 1.2: Typical profiles for potential temperature (red), moisture (blue) and wind (black) during the day (top) and night (bottom). The dashed lines indicate where the profiles are extrapolated into the roughness sublayer and the surface layer profiles are not valid.

Here, $\kappa = 0.4$ and $q_* \equiv -\frac{LE}{\rho L_v u_*}$ and $\theta_* \equiv= -H/\rho c_p u_*$ are the normalised sensible and latent heat flux respectively, in which u_* is the friction velocity, a measure of the surface shear stress.

The ϕ-functions are called the flux-gradient functions. Their shape was determined during the famous Kansas 1968 experiment (Dyer, 1974)[2]. These functions can now be used universally to estimate turbulent fluxes using observed vertical gradients of temperature or humidity.

PENMAN-MONTEITH

Applying MOST to estimate latent and sensible heat fluxes requires observations at least at two heights, which are not always available in operational settings. The Penman equation is a solution to overcome this problem by using observations at only one height. By making a clever link between the flux-gradient law and the surface energy balance. A complete derivation of Penman's equation is given in Chapter 5. The resulting expression is:

$$LE = \underbrace{\frac{s(R_n - G)}{s+\gamma}}_{\text{available energy}} + \underbrace{\frac{\rho c_p (e_s(T_a) - e_a)}{r_a(s+\gamma)}}_{\text{atmospheric demand}} \tag{1.4}$$

This formulation captures the two essential components of evaporation: the energy available at the surface for flux transport and the atmospheric demand for moisture through the vapour pressure deficit. Penman's original work (Penman, 1948) focused on wet surfaces, providing estimates of potential evaporation under unlimited water supply. Monteith (1965) later extended this model by incorporating a surface resistance term to account for vegetation behaviour. Recognizing that plants respond dynamically to their environment, Jarvis (1976) proposed making the surface resistance r_s variable based on environmental controls, such as light, humidity, and soil moisture. This allows the model to reflect the active regulation of water loss through stomatal control.

EDDY-COVARIANCE

Besides indirect turbulent estimates based on MOST, a technique called eddy-covariance (EC) can be used to directly measure turbulent transport (Rotach & Holtslag, 2025). These measurements are used as a reference in Chapter 5.

An eddy-covariance instrument typically combines a sonic anemometer to record (fluctuations of) wind and air temperature, with an instrument for measuring humidity: a fast-response hygrometer. A sonic anemometer emits sound waves in three spatial directions and measures their travel times, which are influenced by the wind speed along the path and the air temperature—sound travels faster with a tailwind and in warmer air. Moisture can be measured with a gas analyser that uses the absorption of radiation

---

[2] The attentive reader will notice the gap in time between the description of the Monin-Obukhov Similarity Theory (1954) and the definition of the flux gradient functions (1968). Prior to the Kansas experiment, the required high-frequency, fast-response instruments were not available (Moene & van Dam, 2014). I was told the following anekdote about this experiment by John Finnigan. The researchers at the time experienced difficulties finding an appropriate measurement location. The fieldwork was held back by one of the farmers owning the land, and could only be conducted once the land was passed on from father to son.

to determine the number of H_2O molecules between a transmitter and receiver. The turbulent fluxes can be derived from the EC measurements as the covariance of the fluctuations in vertical wind (w'), potential temperature (θ') for the sensible heat flux, and specific humidity (q') for the latent heat flux.

As attractive as a direct measurement of the turbulent fluxes may sound, EC has serious limitations and drawbacks, particularly its sensitivity to the “footprint” – the upwind area that contributes to the measurements. This area changes over time, depending on the atmospheric stability, wind speed and direction. These variations make the interpretation and processing of EC data particularly complex in heterogeneous landscapes (Jongen et al., 2024; Rannik et al., 2012).

1.2.3. ROUGHNESS SUBLAYERS

Directly at the surface, the air does not neatly follow the logarithmic shape described by the flux-gradient models. Individual roughness elements disrupt the flow and the air has to flow around obstacles. This layer (roughly 1.5 x the obstacle height) is referred to as the roughness sublayer (RSL, Figure 1.1) (Raupach et al., 1980). This roughness sublayer is the topic of Chapter 4 of this thesis.

Recent efforts have focused on describing this roughness sublayer over urban (Barlow & Coceal, 2008) or natural vegetation, such as forest in the order of 20-30 meters high (Harman & Finnigan, 2007, 2008, e.g). However, many climate zones consist of shorter vegetation (e.g. tundra, steppe, etc) and most agricultural crops can be characterised as short canopies. Moreover, a classical meteorological measurement field is covered with a grass layer of “precisely” 10 cm (World Meteorological Organization, 2023). For such low vegetation layers roughness sublayer models are generally deemed unnecessary or overly complex. Instead, surface-layer models are extrapolated down to the surface, despite the fact that its well known that they do not hold in the RSL.

A small change in the description of the temperature profile near the surface can have large effects on the corresponding sensible and latent heat fluxes due to the logarithmic nature of the profiles. Until recently, no measurement methods were available to resolve temperature profiles in and near the grass surface. Traditional thermometers are too large and would disturb the air they are trying to measure. Fine-scale thermocouples are more suitable for these purposes, but many would be needed to achieve a high coverage. In this thesis, we will however show that there is an alternative: Distributed Temperature Sensing (DTS).

DISTRIBUTED TEMPERATURE SENSING

DTS measurements are performed using one or more fiber optic cables attached to a specialised computer. The machine pulses laser light into the optical fibres and analyses the light scattered back to the machine (Thomas et al., 2012a). The time-of-flight is used to determine the distance along the cable where the scattering took place (Hartog, 2017). This backscatter forms because the fibre does not transmit the laser perfectly. Some of the light will interact with the glass molecules and is redirected in random directions. Most of the scattering is elastic, the light “bounces off” the molecules without a change in energy (Bolognini & Hartog, 2013). However, a portion of the light undergoes inelastic scattering: the Raman effect. Photons absorb some vibrational energy from a molecule (’Stokes’ scattering), or lose energy to the molecule ('anti-Stokes' scattering) (Raman, 1928). As the vibrational energy of a molecule is temperature-dependent, so is the Raman scattering. A photon is more likely to gain energy from a warmer molecule, making the Stokes to anti-Stokes ratio strongly related to temperature.

The measurement provides temperature readings along the cable, with an average resolution of every 20–30 cm, depending on the specific machine and cable choices. Various cable setups allow for flexible applications, including long-distance measurements (Dai et al., 2023), array-based monitoring (Thomas et al., 2012a), and high-resolution vertical profiling (Sigmund et al., 2017; Zeller et al., 2021).

1.3. THIS THESIS

This thesis work is done in the context of spring frost damage in fruit orchards. To predict and prevent damage, we need to understand the conditions within an orchard canopy. This is a complex and fascinating interplay between the tree's physiological response, the synoptic weather situation, energy transport within the vegetation canopy, and the underlying cover crop.

SPRING FROST

Spring frost damage to young plants and buds is an important challenge for agriculture around the world, especially for fruit production (Snyder & De Melo-abreu, 2005). In 2021, a severe night frost period in April caused tree flowers and buds to freeze in France, leading to 27% less wine production than in 2020 (International Organisation of Vine and Wine, 2021).

Two phenomena can cause air temperatures to drop below zero: advective and/or radiative frost. The former is caused by the advection of cold air, generally originating in polar regions. It is often paired with cloudy conditions and moderate to strong winds (2.2 – 4.5 m/s) and therefore a well-mixed atmosphere. As it is more common for this type of frost to occur during winter, the trees do not suffer damage from the low temperatures. Radiative frost is a result of (intense) longwave radiative cooling under clear skies and is enhanced under calm or light wind conditions (less than 1.8 m/s). The result is a surface-based thermal inversion, i.e. a layer of air close to the surface in which the temperature increases with height above the ground (Dupont & Patton, 2012; Kalma et al., 2012). This type of frost can also occur during spring. When daytime temperatures are rising and the growing season has started, trees lose their ability to withstand low temperatures (so-called cold hardiness). In this stage, radiative frost can cause severe damage to sensitive tissues, such as buds and flower petals.

Yet, in the field, an air temperature above 0 °C does not necessarily mean that there will be no frost damage. Plant temperatures can fall below air temperatures, depending on the meteorological conditions and field characteristics (e.g. soil type and moisture, crop density and canopy height (Barlow et al., 2015)). Meteorological variables such as relative humidity, wind speed and cloud cover (Perry, 1998) influence the temperature of the flowers, by interacting with the plants' energy balance, as is shown in Figure 1.3.

So, to mitigate damage, the leaf energy balance has to be modified. Farmers take active measures to raise plant and air temperatures. Wind machines mix warm overlying

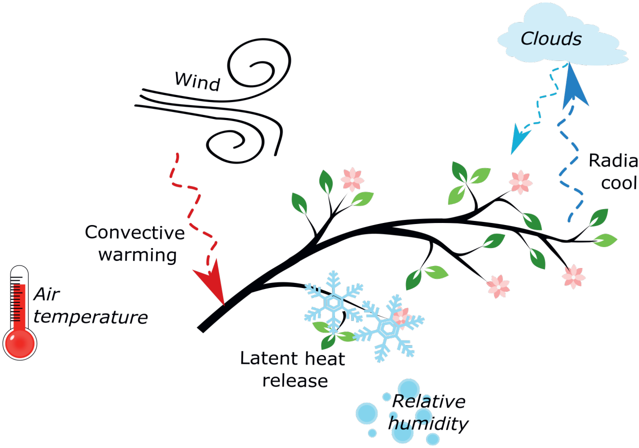

Figure 1.3: Meteorological conditions and their relationship with the plant energy balance, relevant during a spring frost night.

air down to the vegetation, hotpots warm the trees from below, sprinklers protect the buds with a coating of freezing water, and farmers mow the grass to optimise heat release from the soil (e.g. Atam et al., 2020; Heusinkveld et al., 2020; Ghaemi et al., 2009; Anconelli et al., 2002; O'connell & Snyder, 1999; Donaldson et al., 1993). Until now, research on the efficiency of these methods has focused on raising the air temperatures. To understand when and how these measures should be applied, we need to shift our focus to the plant's temperature to understand when frost damage to buds and flowers occurs. Each measure interacts with its environment and the plant in a unique way that will need to be understood to prevent a sub-optimal use of resources. In this thesis, I will focus on wind machines and surface manipulation.

WIND MACHINES

Wind machines blow air (more or less) horizontally to break the temperature inversion, bring warmer air close to the surface and raise the temperature close to the leaves (Ribeiro et al., 2002). The additional wind also breaks the microscale boundary layer over the plant surface, enhancing energy transport from the relatively warm air to the plant. The efficiency of a wind machine strongly depends on the inversion strength. The temperature increase at 2.0 m height typically achieved by a wind machine is about 30 % of the temperature difference between 1.5 m and 10 m height (Snyder & De Melo-abreu, 2005). Wind machines are typically operated automatically and start operating just before the air temperature reaches a manually set critical value. By improving our understanding of the interaction between the air flow generated by the wind machine, the orchard trees and the temperature of flowers and buds, we aim to contribute to optimising wind machine operation.

SURFACE MANIPULATION

Underneath the trees, the soil in an orchard is often covered with grass. Grass and other cover crops can reduce the temperature in an orchard because they act as an insulator, preventing energy exchange with the soil. The underlying physical processes are complex and depend on the energy exchange between air, vegetation and soil. The total energy released from the soil depends on the amount of energy stored in the soil during the day and the surface layer's ability to emit that energy during the night.

Grass has a higher albedo than bare soil, reflecting more solar radiation during the day. This results in less energy storage during the day, and thus less upwards energy transport during the night. The degree to which this heat can be released depends on the length of the grass. The airy vegetation layer itself works as an isolator, limiting energy exchange between air and soil. So, a thick grass layer will not only limit the amount of energy stored in the soil, but also limit the heat release from the soil to the atmosphere.

Donaldson et al. (1993) and Leyden and Rohrbaugh (1963) showed how various weed control strategies can be effective in raising the minimum temperature in orchards. Weed removal turned out to be effective provided that plant material is removed. When dead organic material remains on the surface, it has the same isolating effect as a thick grass layer.

Though simple, grass removal thus has a high potential of raising air temperatures during the night. However, the low soil-bearing capacity of a bare surface makes it very impractical for large agrimotors. As grass cover is thus a necessity in orchards, we want to understand to what extent keeping it short will affect the surface energy balance.

OVERVIEW

An overview of the processes we study in this thesis is given in Figure 1.4. Chapter 2 focuses on the interaction between the wind machine jet and orchard trees, specifically its influence on leaf temperatures. Using DTS we were able to measure high-resolution vertical and horizontal temperature profiles in the roughness sublayer of an orchard.

The scope of Chapter 2 does not go beyond the temperature of the plant organs. However, a temperature below zero does not result in damage per se, as I will explain in Chapter 3. There, we explore the freezing process at the cellular level and discuss how freezing can be detected. Existing detection methods are developed for controlled laboratory settings and are unsuitable for field conditions. We investigate the potential of thermal imaging to detect freezing events in the field, opening the door to studying, for example, the effects of different cover crop strategies.

In order to understand the influence of a cover crop within an orchard canopy, we must first understand the effect of crop (here: grass) height in an open field. This is the focus of Chapter 4, where we use a fine-scale DTS setup to analyse near-surface temperature profiles. We examine how these profiles deviate from the expected logarithmic behaviour and how they are influenced by variations in grass height.

In Chapter 5 we take a small detour into latent heat transport. We investigated the performance of the Penman-Monteith and its underlying assumptions. We show that here too, accurate microclimate representation is crucial for estimating transpiration, as model errors are the largest when large temperature differences occur between vegetation and air.

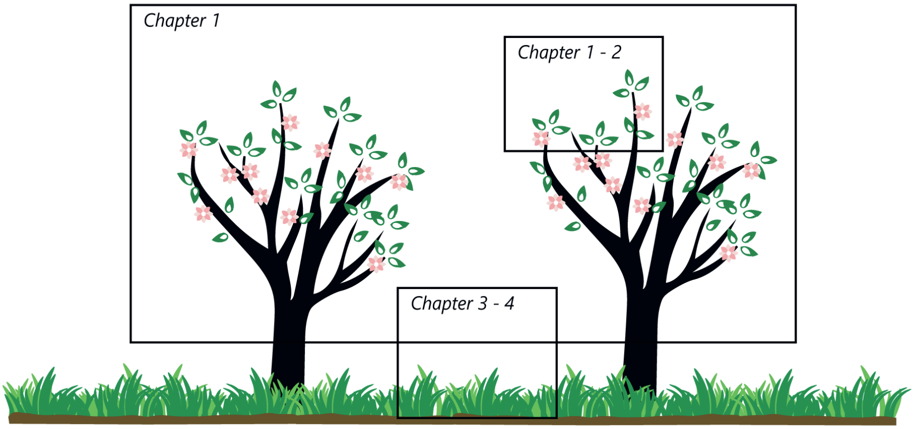

Figure 1.4: Schematic overview of the contents of this thesis.

2

PLANT–ATMOSPHERE HEAT EXCHANGE DURING WIND MACHINE OPERATION

> *We are apt to remember and cherish the flowers which appear earliest in the spring.*
> *I look with equal affection to those which are latest to bloom in the fall.*
>
> Henry David Thoreau

This chapter has been originally published as:
Boekee, J., Dai, Y., Schilperoort, B., Van de Wiel, B. J., & ten Veldhuis, M. C. (2023). Plant–atmosphere heat exchange during wind machine operation for frost protection. Agricultural and Forest Meteorology, 330, 109312.

Summary

To mitigate spring frost damage, fruit farmers use wind machines to mix warm overlying air down to the vegetation. Up to this point, studies on wind machine efficiency have focused on air temperatures. The temperature of different plant organs during operation remains unknown, while critical for the actual degree of frost damage. With Distributed Temperature Sensing we measured vertical in-canopy air temperature profiles in a pear orchard in the Netherlands and thermistors were installed to determine the plant tissue temperatures. We found that to optimise wind machine operation, it is important to consider two effects of a wind machine: 1) mixing of stratified air above and into the canopy layer and 2) erosion of the leaf boundary layer to facilitate plant-air heat exchange. We show how foliage reduces plume penetration to the ground with distance to the wind machine. Due to this blocking at least 15 rotations (~ 75 minutes) are needed for optimal mixing. Leaf temperatures lag behind air temperatures, due to strong radiative cooling. We found that over the rotation cycle of a wind machine the temperature difference between leaf and air is variable as convective warming repeatedly dominates over radiative cooling. This is different for flowers and shoots due to different heat capacities. Thin flower petals store little heat and are almost in direct equilibrium with air temperature changes. Shoots, with their higher heat capacity and lower surface/volume ratio, store more heat during the day that is slowly released at night. This discrepancy between plant and air temperature should be considered for frost damage prediction.

2.1. INTRODUCTION

In many climates, spring frost can cause extensive damage to crops resulting in substantial economic losses in the agricultural sector (Snyder & De Melo-abreu, 2005). To mitigate this damage, farmers take measures to raise plant and air temperatures in their fields. Wind machines are increasingly used to prevent or mitigate the adverse effects of night frost, particularly in the fruit sector. Up to this point, studies on wind machine efficiency have focused on how wind machines change air temperatures. Here, we show how warm air aloft is transported into the canopy and subsequently warms plant leaves and flowers.

Wind machines prevent frost damage via two processes. Firstly, they mix the higher, warmer air with near-surface, colder air thus breaking the temperature inversion (Ribeiro et al., 2006; Battany, 2012). Secondly, they erode the viscous microscale boundary layer around the leaf surface, thereby enhancing the local heat transfer between (warmer) air and leaf (Snyder & De Melo-abreu, 2005; Kimura et al., 2017).

To decide when to turn on the wind machine, farmers monitor air temperatures to stay above a critical temperature range. The critical range is defined as the range of temperatures at which 10% - 90% of the flower buds freeze and depends on the phenological development stage of the flower. As a flower develops from dormancy break to fruit set, the critical damage temperature increases (Quamme, 1978; Ashworth et al., 1989).

However, maintaining air temperature above the critical range does not ensure that damage is prevented. Critical temperature ranges are determined in a laboratory setting (in a so-called ’cold chamber’) where plant and air temperatures are in equilibrium as a result of active mixing. In reality in the field, plant and air temperatures change at different rates. Especially in still air, plant tissue can be 1-3 degrees cooler than the surrounding air (Monteith & Unsworth, 1990; Landsberg et al., 1974; Leuning & Cremer, 1988).

Plant-air energy exchange varies over a range of time scales (Monteith & Unsworth, 1990). Variations in micro-climate during frost events, such as wind speed and cloud cover, influence the temperature of plant tissue at short (minutes to hours) time scales (Perry, 1998). In-canopy air temperatures vary on longer timescales (hours to days) as a result of the bulk energy balance at the canopy-atmosphere interface (Dupont & Patton, 2012).

Previous work has explored the effect of wind machine operation modes on *air* temperatures in and above the canopy, with respect to tilt angle (Heusinkveld et al., 2020; Battany, 2012; Beyá-Marshall et al., 2019), rotation time (Heusinkveld et al., 2020) and timing of the start of machine operation Ribeiro et al. (2006). Kimura et al. (2017) show how during the rotation cycle of a wind machine the *plant-air temperature difference* varies in a tea plantation. Using temperature measurements in artificial leaves distributed over the field, they find a delayed thermal response of the leaf. In fruit orchards, with a higher, more developed canopy, we expect an additional delay in temperature response to wind machine operation, due to stronger dampening by the canopy. Hence, to optimise wind machine operation in higher canopies such as fruit orchards, it is important to understand 1) how warm air mixes into the bulk canopy layer and 2) how the plant tissue responds to the induced fast fluctuations in micro-climate.

To answer these questions we use data from a field campaign in a pear orchard in Zeeland, The Netherlands during clear-sky nights in spring (Sect. 2.2. Using distributed temperature observations of the canopy air at high spatial resolution combined with leaf and flower bud temperatures, we study how warm air penetrates into the canopy. We use a conceptual model to quantify the energy exchange between plant and air during operation of the wind machine (Sect. 2.3. Conclusions and recommendations are considered in Sect. 2.4.

2.2. MATERIALS AND METHODS

2.2.1. OBSERVATIONS

FIELD SITE

Data were collected during field studies on 13-14 April 2021 and 7-8 May 2021 from approximately 20h till 8h, in a pear orchard in Krabbendijke (Zeeland, The Netherlands, 51°25’44.7”N, 4°8’8.5”E). The pear trees (variety: Pyrus communis L. ‘Conference’) are pruned to have 2-3 scaffold limbs and an open centre. In April the trees are covered with buds and small leaves. In May the leaves are fully grown and only some late blossom is still present. The ground between the rows is covered with long grass and below the trees the bare soil is covered with mulch.

Since November 2018 this orchard is protected by a wind machine manufactured by Orchard-Rite®. The wind machine has a 10.7 m hub height and 6 m diameter double-bladed fan which blows air almost horizontally, with a modest downward angle of 8°. The blades rotate at 554 rpm, while the rotor makes a slow 360-degree rotation around its vertical axis, with a 5-minute (user-specified) period. At a fixed location in the field, the passing of the jet can thus be experienced as a strong gust of relatively warm air. To limit the effect of ’statistical noise’ data are phase-averaged over multiple rotations. This averaging is synchronised based on the moment where the peak in wind speed occurs, which receives timestamp zero.

The wind machine is activated automatically based on a critical temperature set by the farmer (1°C at 1 m height) measured with an unshielded sensor. Nights for field observations are selected based on the calm wind conditions and (mostly) clear skies. An overview of the weather conditions in the field is presented in Figure 2.1. On both nights the maximum wind speed observed at the nearby KNMI station in Woensdrecht (15 km to the West) is 1 m/s. In April, wind machine operation is intermittent for multiple short periods, due to fluctuating temperatures. In May, the wind machine makes two rotations after 23.30h as the temperatures briefly fall below the critical temperature. At midnight, the wind machine is manually set to continuous mode to ensure continuous operation for one hour for the purpose of the field study.

INSTRUMENTS

Figure 2.2 shows an overview of the measurement setup. High-resolution air temperature measurements are obtained through Distributed Temperature Sensing (DTS). This optical fibre technique uses the backscatter of a laser signal to infer local temperature at different cable sections with a sampling resolution of 25 cm and 10 s Thomas et al. (2012b). A thin 1.6 mm fibre optic cable and an Ultima-M system are used. A total cable length of 9 km is attached to the tree branches in a grid pattern to measure horizontal temperature variation at two heights. This is discussed in more detail in a separate paper by the same authors (Dai et al., 2023). In addition, 9 m high DTS towers are erected, at three locations

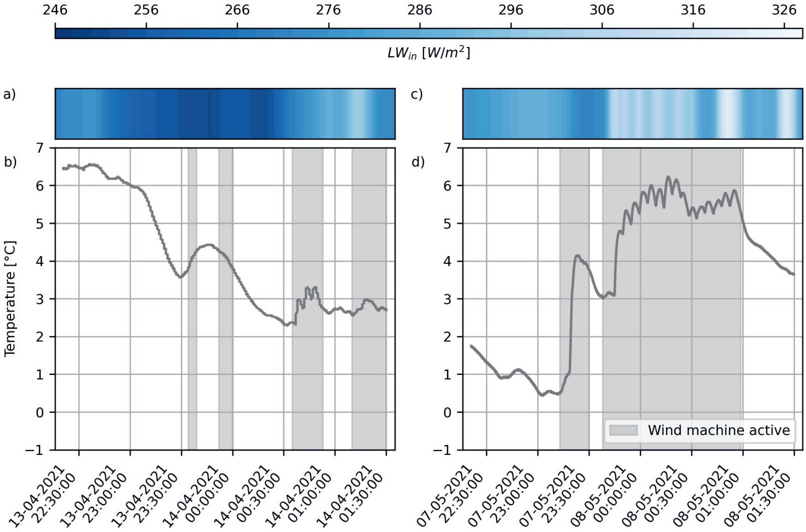

Figure 2.1: Air temperature at 2 m height and incoming longwave radiation during the measurement nights in April (panel a & b) and May (panel c & d) at location N00-N, as indicated in Figure 2.2.

relative to the machine: 12 rows West (~ 40 m distance, mast W12), 31 rows West (~ 110 m, mast W31), and 6 rows East (~ 20 m, mast E06). Two vertical cables are extended along each tower 1.5 m away from the trees.

In May the temperature of a tree close to mast W12 is monitored with small thermistors (Fig. 2.3). Each set of thermistors measured the temperature of the flower (T-Tissue, Ecomatik), shoot (T-Surface, Ecomatik), and leaf, as well as air temperature (LAT-B2, Ecomatik) at 2 cm from the leaf, at a temporal resolution of 0.1 Hz. The thermistors are pressed against the plant organs and thus measure the tissue surface temperature. Three sets of thermistors are installed at heights: 110 cm, 145 cm and 222 cm. Each set of thermistors is installed at the end of a new shoot, between 50 cm and 100 cm from the stem.

Radiation and soil temperatures are measured 100 m North of the wind machine (location N00-N). Soil temperature sensors (HOBO TMCx-HD) measure at 2, 5, 10 and 20 cm depth with a resolution of 5 minutes. A radiometer (Kipp & Zonen, CNR4) measures the incoming and outgoing short- and longwave radiation every minute. A HOBO weather station is installed at the same location, measuring wind speed and direction, air temperature, and humidity at 100 cm, 200 cm, and 300 cm height. Two sonic anemometers (YOUNG Model 81000) are installed at W12 and W31-N, at 300 cm height, just above the canopy. Their measurement resolution is 10 Hz.

All processed data is available in the 4TU data repository, DOI: 10.4121/20581542.

2.2.2. CONCEPTUAL MODEL

In this section, we present a conceptual model that enables us to investigate what processes drive plant-air heat exchange during wind machine operation. A similar modelling

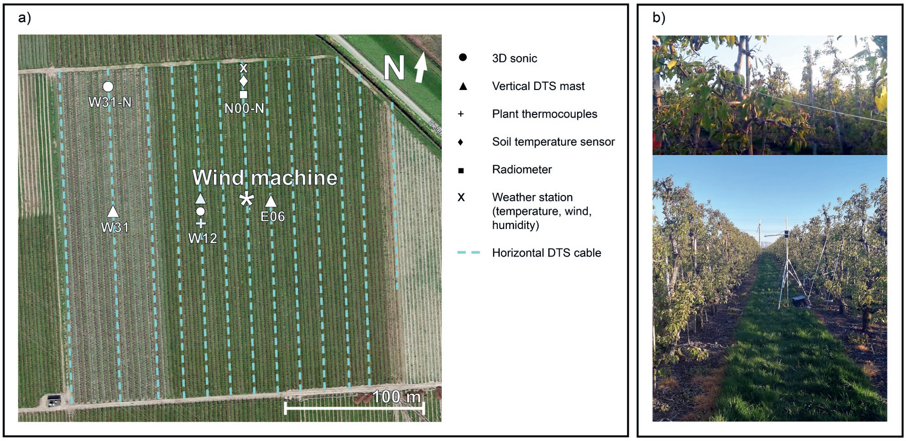

Figure 2.2: Field set-up in the Krabbendijke orchard. Panel a) shows the location of the different instruments. Symbols indicate the locations of the vertical DTS towers E06, W12 (only in May) and W31, 3D sonic-anemometers (only in May), soil temperature sensors, thermistors (only in May), HOBO weather station, and radiometer. The turquoise dotted lines are the horizontal DTS cables installed along the tree rows at 1 and 2 m height. Panel b) shows the DTS cable (top) and the radiometer (bottom) during the May experiment.

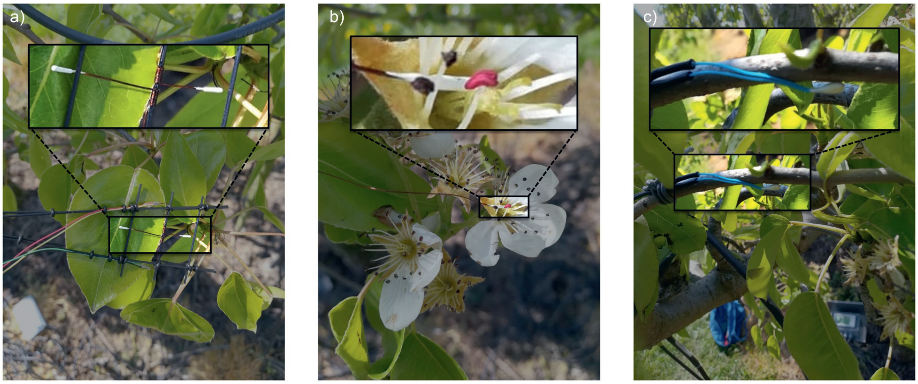

Figure 2.3: Thermistors (leaf-air (panel a), flower (panel b), shoots (panel c)) installed in the orchard in Krabbendijke.

approach has been proven accurate for apple buds (Landsberg et al., 1974; Hamer, 1985, 1986) and blossom (Landsberg et al., 1974), and eucalyptus leaves (Leuning & Cremer, 1988; Leuning, 1988). The instantaneous plant-air temperature differences can be predicted with an error of less than 1 K, thus supporting our approach. We focus our analyses of air-plant heat exchange on the most vulnerable plant organs: leaves, flowers, and shoots. The energy balance of plant organs during a spring frost night is the sum of radiative cooling, turbulent warming, and latent heat release due to dew and ice formation (Monteith & Unsworth, 1990). As we observed no dew and ice formation during our field study, the latent heat release is considered negligible in our analyses.

The budget equation of a plant organ (i.e leaf, flower, or shoot) is therefore conceptualised here as:

$$C_{plant} * \frac{dT_{plant}}{dt} = R_N - H \tag{2.1}$$

in which R_N is the net radiation and H is convection in W/m^2 (Monteith & Unsworth, 1990). T_{plant} is the temperature of the plant tissue (i.e. leaf, shoot or flower) [K]. C_{plant} is the heat capacity per area of plant tissue [J m^{-2} K^{-1}].

RADIATION

During the night net radiation is the sum of incoming and outgoing longwave radiation.

$$R_n = R_{lw,in} - R_{lw,out} \tag{2.2}$$

All surfaces surrounding plant tissue emit radiation: the sky, ground, and parts of the plant. A leaf hidden deep in the canopy receives a similar amount of longwave radiation from its neighbours as it is emitting itself. This results in radiative equilibrium. A leaf at the end of a shoot is exposed to the relatively cold sky and ground instead. It can thus cool down to below air temperature.

The longwave radiation emitted by a surface can be calculated through the Stefan-Boltzmann law:

$$R_{lw,out} = \sigma \varepsilon_{plant} T_{plant}^4 \tag{2.3}$$

in which ε is the emissivity and σ is Stefan-Boltzmann's constant [W m^{-2} K^{-4}].

The incoming longwave radiation $R_{lw,in}$ per square meter is a weighted average of incoming radiation from the canopy, sky, soil, and other plant tissue. The weighting factors are the fractions of the full hemisphere obscured by the different surfaces. This is the definition of the skyview factor SVF (Watson & Johnson, 1987). Here we also introduce the analogous ground view factor (GVF) and leaf view factor (LVF). Assuming a two-sided perfectly horizontal leaf (the lower half only faces the ground, and the upper half only faces clear or cloudy sky) gives:

$$R_{lw,in} = 0.5 SVF \sigma \varepsilon_{sky} T_{sky}^4 + 0.5 GVF \sigma \varepsilon_{soil} T_{soil}^4 + LVF \sigma \varepsilon_{plant} T_{plant}^4 \tag{2.4}$$

CONVECTION

Turbulent mixing (H) between air and plant causes temperature differences to be reduced. H can be parameterised using a resistance law Raschke (1960):

$$H = \frac{\rho c_p \cdot (T_{plant} - T_{air})}{r_H} \tag{2.5}$$

here, ρ is the density [kg m^{-3}] and c_p heat capacity of air [J kg^{-1} K^{-1}].

r_H [s m^{-1}] is the resistance for turbulent heat transfer due to the presence of a leaf boundary layer. There are no universal relations that describe r_H. However, H can be non-dimensionalized as the Nusselt number Schuepp (1993):

$$\mathrm{Nu} = \frac{H/(\rho c_p)}{\kappa (T_{plant} - T_{air})/L} = \frac{L}{r_H \cdot \kappa} \tag{2.6}$$

here, L is the representative length scale of the leaf [m] and κ the thermal diffusivity of air [m^2 s^{-1}].

The Nusselt number is the ratio of convective to conductive heat transfer over a surface (or the ratio of 'turbulent' to molecular diffusivity). Its value depends on the local Reynolds number ($\mathrm{Re} = \frac{u \cdot L}{\nu}$) and local Grashof number ($\mathrm{Gr} = \frac{|T_{air}^{-1} \cdot g \cdot L^3 \cdot (T_{plant} - T_{air})|}{\nu^2}$). Here ν is the kinematic viscosity of the air [m^2/s], g the gravitational constant [m/s^2] and u the wind velocity [m/s]. Hence, we will use (universal) relations of the form $\mathrm{Nu} = f(\mathrm{Re}, \mathrm{Gr})$ in order to parameterise the turbulent heat flux. These universal flat-plate relationships have been adapted to approximate leaves in a natural environment. The formulations are given in Appendix A.1.1, Table A.1.

There are two modes of turbulent transport: "forced" convection (active) and "free" convection (passive). Forced convection is the exchange through the boundary layer of a surface exposed to a moving air stream, and free convection is the ascent/descent of warm/cold air over a surface due to density differences. Under forced convection Nu is therefore a function of the Reynolds number Re (ratio of inertial to viscous force). Under free convection, Nu depends on the Grashof number (ratio of buoyancy to viscous force).

Roth-Nebelsick (2001) and Bailey and Meneses (1995) motivated that purely free convection is unlikely to occur in nature, as even a very slight air movement already results in a significantly changed temperature distribution over a leaf surface. However, as highlighted by Schuepp (1993), the transition regime (i.e. "mixed" convection) is not uncommon in dense canopies or during lulls between stronger wind speeds. Interestingly, this is exactly what happens during wind machine operation. A leaf is alternatingly exposed to high wind conditions in which forced convection is dominant, and low wind conditions in which free convection plays a more important role. When both forced and free convection are important (i.e mixed convection), Nu is a function of both Re and Gr.

Finding a satisfactory description of the Nusselt number for mixed conditions remains a challenge. Generally, Nu is calculated for both forced and free convection and the largest value is used. Alternatively, forced and free conductances are summed, equivalent to parallel resistances (Schuepp, 1993).

The regime transitions between free, mixed and forced convection are often described in terms of (rigid) thresholds based on a so-called leaf-Richardson number Ri, defined as:

$$\mathrm{Ri} = \mathrm{Gr}/\mathrm{Re}^2 \tag{2.7}$$

As such it compares non-dimensional buoyancy effects over inertial effects. However, the exact Richardson borders for regime occurrence are not sharply defined (Monteith & Unsworth, 1990; Parkhurst et al., 1968).

Here, we introduce and apply a new conceptual view, that eliminates the need for empirical sharp boundaries between regimes. The logic of Equation 2.7 can also be seen as the ratio of two competing Reynolds numbers, or likewise, as two competing velocity scales. This vision is explained in Appendix A.1.1. This reduces the need for the different formulations (Ap. A.1.1: Tab. A.1) to one equation, suitable for all quasi-laminar regimes ($\mathrm{Re}^* < 2 \cdot 10^4$):

$$\mathrm{Nu} = 0.6 \cdot (\mathrm{Re}^*)^{0.5} \tag{2.8}$$

and one for all turbulent regimes ($\mathrm{Re}^* > 2 \cdot 10^4$):

$$\mathrm{Nu} = 0.032 \cdot (\mathrm{Re}^*)^{0.8} \tag{2.9}$$

Here Re^* is the Reynolds number based on the refreshment velocity m^* that combines the wind velocity and a velocity scale for free convection:

$$m^* = \sqrt{(w^{free})^2 + u^2} \tag{2.10}$$

w^{free} is the typical velocity scale for free convection (Appendix A.1.1 for derivation):

$$w^{free} = \sqrt{2Lg\frac{T_{plant} - T_{air}}{T_{air}}} \tag{2.11}$$

MODEL SETUP AND CALIBRATION

Equation 2.1 is solved numerically using an Euler forward method. We have tested for numerical convergence (and stability) for time steps between 0.001 and 10 seconds.

When we know the *volumetric* heat capacity of a plant organ [MJ m^{-3} K^{-1}], we can determine the heat capacity *per area* (C_{plant} in J m^{-2} K^{-1}). Therefore, we need to know the organ's shape, or at least the ratio between volume and surface area. We approximated the leaf and flower as flat circle-shaped plates with a thickness t_{plant} and radius L. The shoot was approached as a cylinder. Using typical heat volumetric capacities of 0.5, 2, and 4.2 MJ m^{-3} K^{-1} for respectively the flower, leaf, and shoot, we calibrated the thickness and radius. A number of realistic evenly spaced samples is taken for each parameter, and the modelled leaf temperatures are compared to the observations. The parameters that give the lowest MSE are selected. The exact values and calibration ranges are given in Appendix A.1.2, Table A.1.

The different plant parts also experience different SVFs and wind speeds due to the geometric effects of the canopy itself. This is included as $U_{plant} = \gamma * U_{obs}$, in which U_{plant} is the wind experienced by the plant, U_{obs} the observed wind at the top of the canopy and γ a height dependent constant between 0-1. As we did not measure the wind and radiation in the canopy, γ and SVF are also determined through calibration, resulting in a total of 5 calibration parameters for each of the three (flower, leaf, and shoot) models.

Note that the calibration parameters are indicative of the order of magnitude, and should not be interpreted as actual and exact values. For example, due to its turbulent character, wind can be quite different next to a leaf compared to just 5 cm distance. The model code is available on Github (https://github.com/judithboekee/blossom). It is intended for use only in combination with observation data for model tuning and verification."

2.3. RESULTS AND DISCUSSION

In this section, we first discuss how vertical temperature profiles in the bulk canopy layer respond to wind machine operation, at different locations and times in the growing season. Next, the energy transport between the leaf and atmosphere during the fast micro-climate fluctuations is quantified using observations in combination with the conceptual model outlined above.

2.3.1. HEAT TRANSPORT INTO THE CANOPY

Vertical DTS cables measuring vertical temperature profiles are used to analyse heat transport into the canopy. Figure 2.4 shows the mean vertical profiles during ON (14-04-2021 00:38 till 14-04-2021 00:50 and 07-05-2021 23:40 till 08-05-2021 01:00) and OFF (14-04-2021 00:00 till 14-04-2021 00:30 and 07-05-2021 22:30 till 08-05-2021 23:00) mode. Figure 2.5 shows how these profiles vary over time during a phase-averaged rotation cycle.

In OFF mode, cooling of the overlying air by the cold surface results in a stable vertical temperature profile with the coldest temperatures and strongest vertical temperature gradient (i.e. a temperature inversion) close to the surface (Fig. 2.4a). In May the trees are leafed out and the inversion occurs at the top of the canopy at $z = 300$ cm instead of near the ground (Fig. 2.4b). Here the dense foliage cools radiatively. This limits the mixing of cold, dense air in the canopy with the warmer air above.

Interestingly, the rather uniform temperature within the canopy in the full leaf stage suggests that some kind of longwave radiative 'equilibrium' is reached, in absence of strong turbulent mixing. In accordance with equations 2.2 and 2.3 this suggests that at each height within the canopy, $LVF \approx 1$ (and SVF and GVF are approximately zero) and $R_{lw,in} \approx R_{lw,out}$.

In ON mode the vertical temperature gradient reduces. The operating wind machine accelerates air and generates a turbulent jet with an 8°downward angle. Flow instabilities at the edge of the jet (Kelvin-Helmholtz type) generate efficient mixing of in-canopy with the above-canopy air.

As a result, in the canopy, the air temperature rises. We observed an average temperature increase in the order of 1-3 °C near the ground. This is in line with earlier studies by Ribeiro et al. (2006) and Heusinkveld et al. (2020) who show an increase of ~ 2 °C. Above the canopy, the air temperature decreases. In May the temperature at 4 - 9 m height is lower during ON mode than during OFF mode (Fig. 2.4c). However, in April there is no cooling at this height. The above-canopy cooling was also not observed in January by Heusinkveld et al. (2020). We hypothesise that when there are no leaves on the trees, the mixing caused by the jet takes place over a rather deep layer exceeding hub height. However, there is no evidence from the current observations to confirm/falsify this.

Figure 2.5 shows how the warm air aloft is mixed down into the canopy, far from the wind machine (Fig. 2.5a) and close by (Fig. 2.5c). The warm air first arrives above the canopy and penetrates between the trees as the wind speed increases. Interestingly, the highest temperature increase happens just *before* the maximum in the wind speed at $t = 0$. At W31 this takes about 60 seconds and at W12 about 30 seconds. The time difference is largest at the furthest location, which presumably is caused by plume dispersion. This is explored more in-depth in a separate study on the same field experiment (Dai et al., 2023).

Next, we define a so-called plume penetration depth p_{plume}, to determine the influence of foliage density and radial distance from the wind machine on plume penetration. Penetration depth is defined as the normalised height below which the vertical temperature gradient remains larger than 0.5 K/m when the jet passes at $t = 0$. Below this height the effect of vertical mixing is limited. We define p_{plume} relative to the canopy height h, and is thus positive downwards into the canopy.

The mean temperature profiles during wind machine operation (Fig. 2.4) show that at the mast closest to the wind machine, the jet can penetrate completely to the ground (May, E06, ON mode). The penetration depth is $p_{plume} = 1$. The temperature gradient in the canopy is small: $dT/dz \sim 0.4$ K/m. At the location slightly further from the wind machine (May, W12, ON mode), only the upper half of the canopy air is well-mixed at $t = 0$. The penetration depth is $p_{plume} = 0.6$. For the location furthest from the fan (May, W31, ON mode), mixing of the in-canopy layer is suppressed. A significant temperature gradient of 0.8 K/m remains in the complete canopy layer, so the penetration depth $p_{plume} = 0$.

In April $p_{plume} = 0.5$ is at E06, at W31 $p_{plume} = 0$. In May the difference in penetration depth between the two masts is smaller. This is due to the increase in foliage density and difference in background conditions. In April a strong temperature inversion is present directly above the surface and minor turbulent mixing near the surface results in a strong temperature change. In May the vertical temperature gradient near the surface is smaller due to the presence of foliage and turbulent mixing will result in a comparatively smaller temperature change.

2.3.2. HEAT TRANSPORT FROM CANOPY AIR TO LEAF

To understand what is driving the energy exchange between leaf and air, we first diagnose the dominant mixing regimes. We use the classification given by Monteith and Unsworth (1990), which is based on the leaf-Richardson number in Equation 2.7 and shown in Figure 2.6a. The dominant regime is the 'Mixed convection' regime, followed by 'Forced convection' during passage of the wind machine jet. Occasionally, 'Free convection' occurs: in situations of very low wind speeds when the temperature difference between leaf and air is large. The wind speeds used for this classification are measured at the top of the canopy. The actual wind speeds next to the leaves will be lower and shifted towards free convection.

Figure 2.6c shows how the plant tissue (i.e leaves) temperature responds to fluctuations in wind and air temperature. Directly after the first passage of the jet (start of the grey band in the figure) the air temperature 2 cm from the leaf rises by 5 degrees and

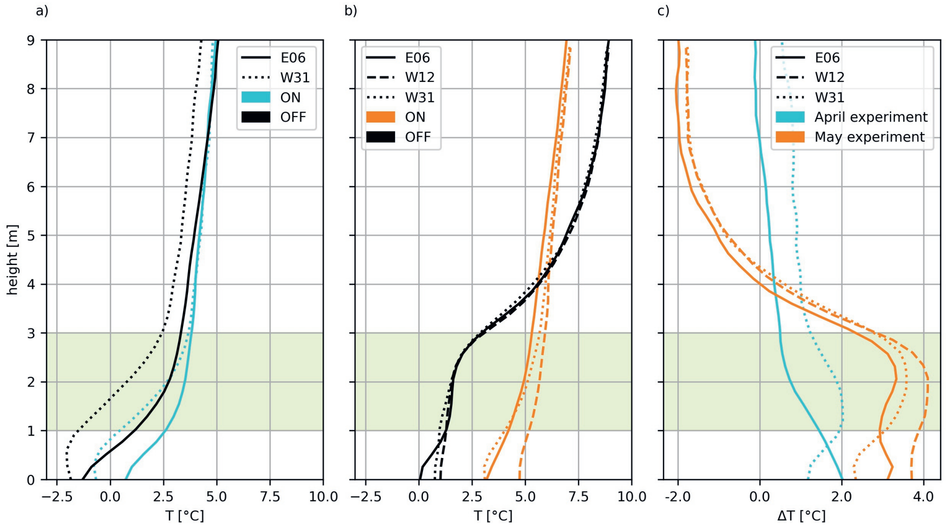

Figure 2.4: Average temperature during ON and OFF mode of the wind machine, measured with the vertical DTS masts during April and May. Panel a) shows April experiment, panel b) May experiment, and panel c) shows the *difference* between ON and OFF mode for both months. Green bars show the height of the horizontal shoots of the pear trees.

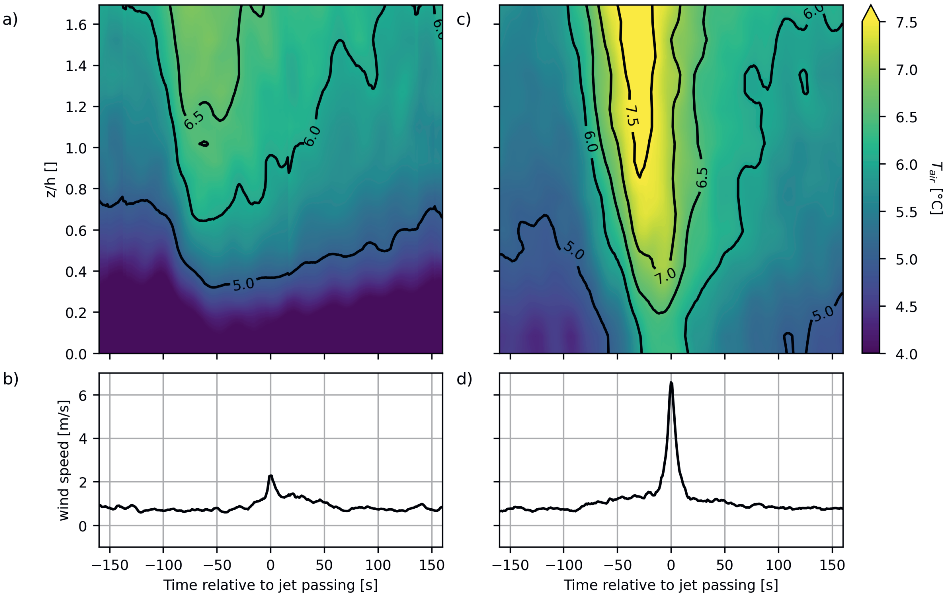

Figure 2.5: The top panels (a, c) show average air temperatures as measured by the DTS cables in May in color and contour lines against height z/h, with canopy height h ~ 300 cm. The lower panels (b, d) show the averaged wind speeds as measured by the sonic anemometer just above the canopy. Panel a) and b) represent location W31 (~ 110m) and panel c) and d) W12 (~ 40m).

this is followed almost instantly by the leaf temperature. Fig. 2.6d shows that leaves deeper in the canopy need more rotations to approach air temperature compared to those near the canopy top (222 cm). At the end of the active rotation period, air temperatures are the same at all heights in the canopy (not shown). All leaves have the same temperature as well, albeit 0.2 °C below the air temperature. From this, we conclude that the wind machine needs at least 15 rotations to reach maximum mixing in the canopy. This "warm-up" time is even more important for the vegetation, due to their delayed response compared to the air temperature. This is in line with the findings of Kimura et al. (2017), who show that boundary layer conductance is synchronised with wind machine oscillations, but leaf temperature reacts with a delay of several seconds.

2.3.3. LEAF ENERGY BALANCE

The conceptual model presented in Section 2.2.2 enables us to investigate what processes drive leaf-air heat exchange during wind machine operation. We introduced a refreshment velocity m^*, which combines the typical velocity scales for forced and free convection. By doing so we avoid the pre-imposed boundaries between turbulence regimes as used in Monteith and Unsworth (1990). In Figure 2.7 we show how the aerodynamic resistances calculated using the original model (Monteith & Unsworth, 1990) result in a sharp change at $Ri = 10$, which is unlikely to exist in nature. We compare this to the m^*-based model which presents a more realistic gradual shift. Discrepancies between the two approaches occur mainly around the $Ri = 10$ boundary and over the range of very low velocities where Monteith and Unsworth (1990) assume the energy exchange through wind (i.e. forced convection) to be negligible. This causes discrepancies between the two approaches of up to 20%. Henceforth we use m^* in our model calculations.

The heat-exchange model is calibrated based on phase-averaged observations of air, soil, and sky temperature as input. Results of the predicted leaf temperature are given in Figure 2.8a, together with the observations. The model reproduces the leaf temperature variation within an absolute error range of 0 to 0.2 °C, about 10% of the mean leaf-air temperature difference. Next, we use the model to compute the plant energy budget terms R_N and H, as shown in Figure 2.8c.

We divide the phase-averaged rotation cycle in three phases: the rising limb with a convex-concave shape, the temperature maximum, and the convex-shaped falling limb. As follows from Figure 2.8c, the convective energy transport dominates during the first two phases, before and during the passage of the jet from $t = -150$ until $t = 10$. This corresponds to a strong increase in air temperatures (due to mixing of the in-canopy air) and thus a larger temperature difference between the air and the plant tissue. The convective heat flux increases linearly with the plant-air temperature difference and depends on the wind speed via the boundary layer resistance (Eq. 2.5). Consequently, when the jet speed peaks at $t = 0$, the increase in wind speed enhances the convective energy exchange resulting in an additional leaf temperature increase of 0.2 K. After the passage of the peak (phase 3), radiative cooling again becomes dominant. At the start of phase 3, leaf temperature is nearly equal to the air temperature, the small temperature difference combined with low wind speeds limits further convective heat exchange. The leaf cools and radiative cooling gradually decreases. Finally, the influence of the next jet passage is felt (as the jet plume has a finite horizontal extent and is also advected), and

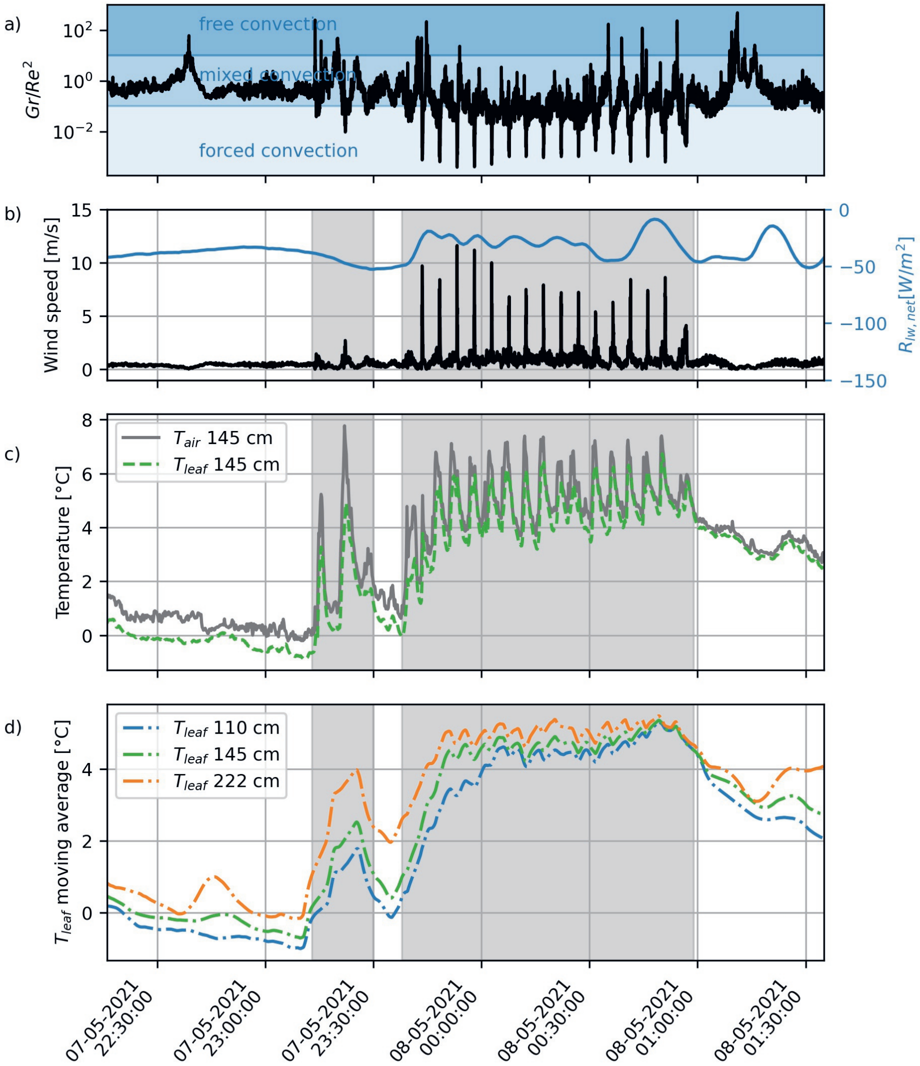

Figure 2.6: Main mode of convective energy transport (i.e. according to criteria of Monteith and Unsworth (1990) in Table A.1) at 300 cm height (panel a). Wind speed and net longwave radiation (panel b), leaf and air temperature (panel c), and 500 s moving average of leaf temperature at three heights in the same tree to show the trend (panel d) before, during (highlighted in grey) and after operation of the wind machine in the night of 7-8 May at W12.

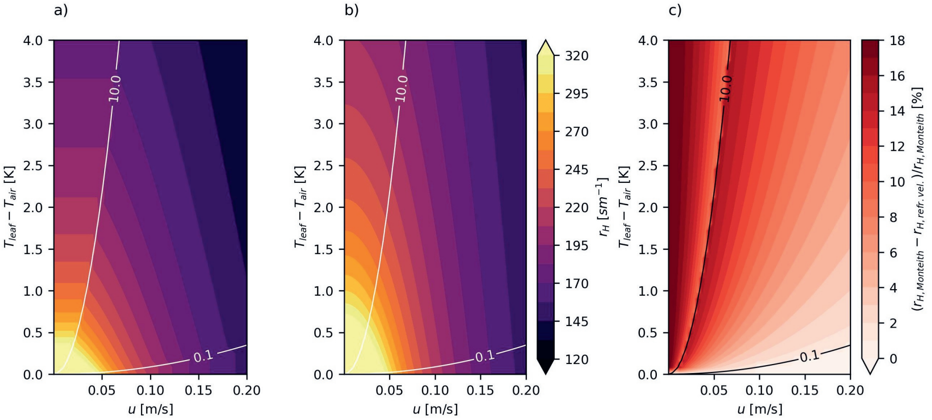

Figure 2.7: Aerodynamic resistance r_H for a range of leaf temperatures and wind speeds, calculated using the approach presented by Monteith and Unsworth (1990) (panel a), and with our refreshment timescale (panel b), and the difference (panel c). Here we took $T_{air} = 273K$ and $L = 0.08m$ as typical values for the calculations.

convection rises again. Over the full rotation cycle, the heat introduced by convection was 1449 J/m^2 (area under H in Fig. 2.8c), 1416 J/m^2 (area under R_N in Fig. 2.8c) is lost due to radiative cooling. As long as the integrated convective warming is larger than the integrated radiative cooling the leaf will warm over time.

2.3.4. DIFFERENT PLANT ORGANS

Figure 2.9 shows the averaged dynamic temperature response of leaves, flowers, and shoots to the passage of a wind machine jet. The flower tissue responds faster than the leaf due to its lower heat capacity and the difference between air and flower temperature remains close to zero (Fig. 2.9a). The flower temperature is measured at ~15 cm distance from the air temperature. This coherence in signal suggests that specific curve characteristics measured, such as the plateau at -150 to -100 s, have some general validity and are not a coincidence. The temperature response of a shoot differs from that of a leaf or flower: it warms and cools more slowly as a result of its smaller surface/volume ratio (Fig. 2.9a). We account for this by applying a higher heat capacity in the model, however, this results only in a delayed response as compared to the observational data (Fig. 2.9b, blue versus dashed curve). Moreover, the model predicts an initial cooling (first 50 seconds) that is absent in the observations (Fig. 2.9b). This cooling computed by the model is a result of the air temperatures being below shoot temperature in combination with radiative cooling. On the contrary, in the observations, shoot temperature in the first 50 seconds remains almost constant. We hypothesise that cooling in the initial phase is counteracted by an (unknown) source of heat (or a delay process). We now empirically model this extra source of heat as a relaxation term in the budget equation:

$$S = \alpha \cdot (T_{core} - T_{shoot}) \tag{2.12}$$

in which, α is a constant, T_{core} is the temperature of the core of the shoot. As we did

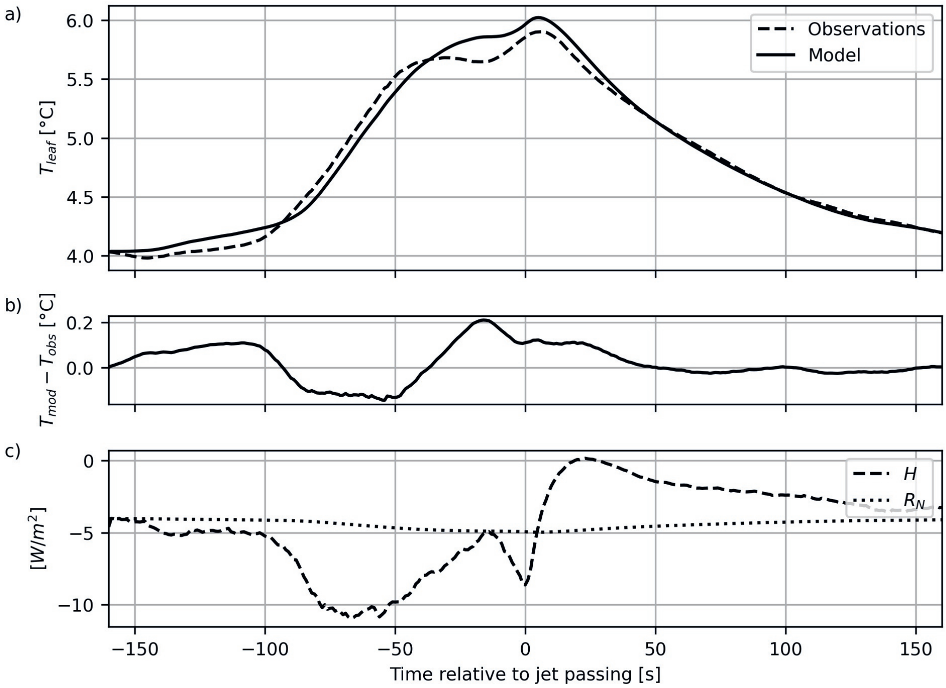

Figure 2.8: Leaf temperature observed with the thermistors and model results (panel a) and the difference (panel b) over an averaged wind machine rotation at 145 cm height. Plant energy budget terms based on the observations according to Equation 2.1: radiation (R_N), and forced and free convection H (panel c).

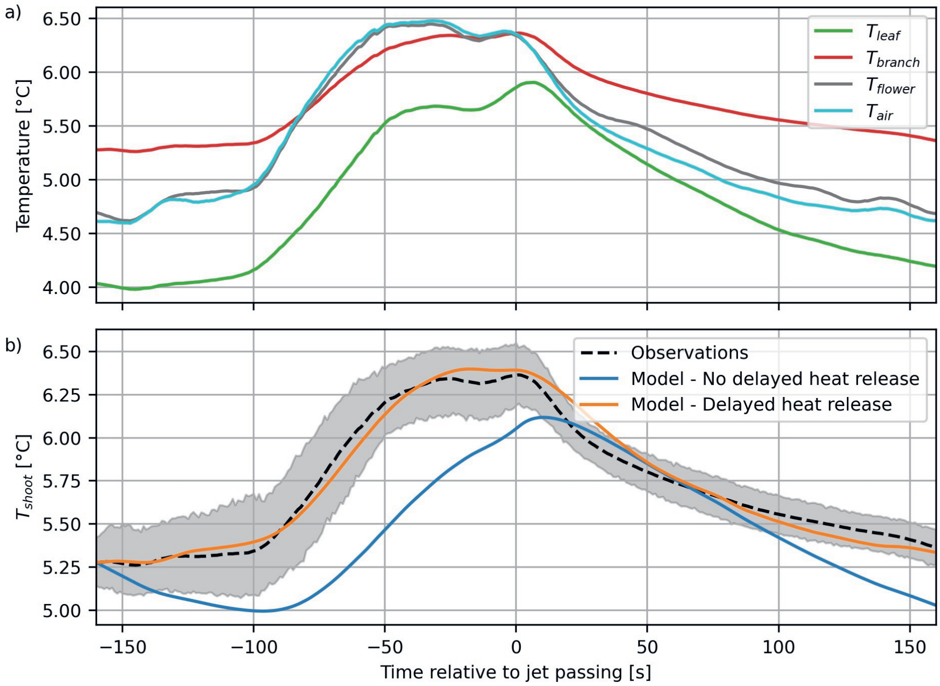

Figure 2.9: Panel a) shows all thermistor measurements at 145 cm: leaf, shoot, flower, and air temperatures. Thermistor sets at other heights show similar behaviour. Panel b) shows observed (the variation between the rotations shown by the grey band) and modelled temperature of the shoot, including (orange) and excluding (blue) a delayed heat release.

not measure this, we used the temperature of the soil at 20 cm depth, which was 8.8 °C. The physical meaning of the extra heat source is beyond the scope of this manuscript. Equation 2.12 is fully empirical and could be interpreted as the heat release from the centre of the shoot to its surface. This process works on a larger timescale and can be seen as delayed heat release from the day. In a separate analysis (not shown here) it was found that the shoot–air temperature difference decreased during wind machine operation. This indeed may suggest that heat storage effects on larger time scales may play a role here. The heat capacity C_{plant} in Equation 2.1 does not cover this delayed heat release. It assumes instantaneous redistribution of heat through the plant tissue. For thin leaves and flowers, this is indeed the case. A thicker shoot or flower bud, however, has a frequency-dependent damping effect, similar to grass and soil (Jacobs et al., 2008; Van Der Linden et al., 2022). Short term-variations in temperature, such as those caused by clouds or the passing of a wind machine jet, penetrate into the outer layer of the tissue only, but cannot reach the central part. Long-term temperature variations such as the diurnal cycle will penetrate to the core. These long-term variations will therefore have a significant effect on the temperature measured at the surface. With the inclusion of the extra heat source, which is promising in its simplicity, the model can accurately predict the dynamics of the shoot temperature.

2.4. CONCLUSION

In this study we investigate heat exchange processes in fruit tree canopies during wind machine operation. We deployed high-resolution Distributed Temperature Sensing (DTS) and leaf thermistors to measure temperature response of leaves, within-canopy and above-canopy air to the fast fluctuations in temperature and wind induced by the machine. We found that to optimise wind machine operation in fruit orchards, it is important to consider two effects of a wind machine: 1) mixing of stratified air above and into the canopy layer and 2) erosion of the leaf boundary layer to facilitate leaf-air energy exchange.

In addition to the average temperature increase, we looked at temperature variation over a five-minute rotation cycle. Thanks to the availability of high-resolution DTS data we are able to characterise the delayed response of in-canopy air temperature compared to the air above. Warm air arrives above the canopy just before the jet passes, due to plume dispersion. Due to plume dispersion, the above-canopy temperatures start rising before the jet core passes. Then, the stably stratified in-canopy air is mixed from the top down to a given penetration depth. This depth depends on the jet strength, distance to the wind machine and canopy density. We found penetration depths varying from 60% penetration close to the wind machine to 30% of the canopy at 110 m in early spring. Penetration was reduced with distance from full-canopy penetration to no penetration in late spring as a result of the denser foliage.

A second effect of the wind machine is erosion of the viscous boundary layer surrounding the leaves, flowers, and shoots by increased wind speeds. The same processes play a role here on the micro scale as on the canopy scale: convective warming and radiative cooling. Radiative cooling depends only on the temperature of the leaf and varies between -4 to -5 W/m^2. Preceding and during the passing of the jet convective energy exchange rises to 10 W/m^2 and dominates due to the high wind speed and large temperature difference. After the peak in wind speed, convective warming approaches zero and radiative cooling restores the temperature difference between air and plant. Before a new equilibrium temperature is reached, the next jet arrives and convective warming erodes the temperature difference again. As long as convective heat repeatedly introduced by the wind machine exceeds radiative cooling, the temperature of the plant tissue shows a positive trend over time, until equilibrium with the well-mixed canopy air is reached.

The conceptual energy balance model we use to quantify heat exchange between plant and air generally shows good agreement with the observations. Main deviations (up to 0.2 °C) occur just before jet passage, minor deviations are found during the rising limb of the temperature curve, as the jet approaches. The most likely explanation for these deviations is the position of wind observations used as input for the model. Sonic anemometers are installed above the canopy, because measuring representative 3D wind fields within a canopy is extremely challenging (Patton et al., 2011). We approximated wind speed in the canopy as a fraction of the wind on top of the canopy. In reality, the damping effect of the canopy is phase-dependent and changes the character of the flow by enhancing turbulence. To improve understanding of in-canopy energy exchange, measuring in-canopy wind velocities will be an important requirement. New developments in wind sensors like Freundorfer et al. (2021) and Alveringh et al. (2022) open a promising avenue for further research.

Our results show that temperature response of different plant organs depends on their heat capacity, strongly related to organ volume, and their surface/volume ratio. Thin flower petals store little heat and are almost in direct equilibrium (and synchronised) with air temperature changes. Leaves store small amounts of heat, but remain cooler than the air as convective warming is counterbalanced by strong radiative cooling. Shoots, with their higher heat capacity and lower surface/volume ratio, store more heat during the day which is slowly released at night. As a result, their temperature remains above air temperature, except at passage of the wind machine, when air temperature briefly exceeds shoot temperature.

The focus of this study has been on temperature response of leaves and flower petals in fruit tree canopies. Our initial analyses of shoot temperature show that their response is significantly different from the thinner tissue of leaves and petals. We attribute this to the higher heat capacity resulting in larger heat storage during the day. This results in a higher average temperature and a dampened temperature response to wind jets in comparison to the leaves and flowers. By implementing a delayed heat release from the shoot core, we are able to replicate this effect with the model. However, to fully understand the origin of this delayed heat release, more observations and physics-based model efforts during wind machine operation are needed. Additional measurements of the internal temperature of the shoot, the stem and sap flow can support estimation of the heat transport from the core to the surface. Since flower buds are likely to show a similar dampened response and are the plant's most vulnerable organs in early spring, better understanding their temperature response is important for fruit frost protection

3

PLANT PHYSIOLOGICAL VARIABLES AT PLAY IN FROST DAMAGE

And the day came when the risk to remain tight in the bud was more painful than the risk it took to blossom.

Anaïs Nin

Summary

When plant water freezes, it releases a detectable thermal signal known as a freezing exotherm. These exotherms are used to determine the lethal temperatures for different fruit cultivars. However, the conventional detection method (differential thermal analysis) is destructive and relies on controlled cold chamber environments, which may not accurately reflect field conditions. To address this limitation, we explored the potential of using thermal imaging in the field to detect freezing exotherms in different development stages.

This chapter is the result of a three-month stay at Cornell University at the lab of dr. Jason Londo (Associate Professor at the School of Integrative Plant Science, Horticulture Section, Cornell AgriTech). During this research visit, I studied the physiological effects of climate stress (particularly frost) on various apple cultivars. In this chapter, I give a little taste of what happens at cellular level during freezing, highlighting that frost damage is, in essence, a form of dehydration.

3.1. WINTER CHILLING

Temperature, along with light, nutrients and water, is fundamental for plants to survive and thrive. All biochemical processes in plants operate within specific temperature limits -both upper (Box 1) and lower- and have an optimum range known as the cardinal temperature range (Hopkins, Hüner, et al., 1995).

In temperate climates, many plant species adapt to low winter temperatures as they survive the winter in a dormant state. Dormancy refers to the inability of plant tissue (such as buds and seeds) to grow, despite the presence of appropriate temperatures and adequate moisture and oxygen. Only a severe frost during dormancy will result in lethal damage. This transition towards dormancy begins at the end of summer, triggered by the decreasing day length (Hopkins, Hüner, et al., 1995).

Higher daytime temperatures in spring will break dormancy, but only if the plants' chilling requirements are met. For instance, species such as apples or pears, require 7 – 9 weeks of accumulated temperatures between 0 – 7 °C. The temperature variations during winters in temperate climates do not pose a problem, as dormant tissue sums the days until the appropriate amount of cold has been reached. This explains the early bloom after relatively warm winters as plants meet their chilling requirement relatively fast (Hopkins, Hüner, et al., 1995).

3.2. SPRING FROST DAMAGE

When daytime temperatures rise and the growing season begins, fruit trees lose their resistance to low temperatures. This is why in springtime, frost can cause severe damage to sensitive tissues, such as buds and flower petals.

Frost damage is not directly caused by below-zero air temperatures but by dehydration of the flower's essential cells (Charrier et al., 2015). As the temperature of the plant drops below zero, the tissue can cool further (6 – 8 °C) before ice forms. This phenomenon, called super-cooling, occurs due to the small volumes of water and the absence of nucleating substances needed for ice crystal formation.

Initially, water will freeze *between* the cells and in the water-transporting vessels. The formation of extracellular ice crystals (i.e. apoplastic freezing) causes a rise in extracellular solute concentrations (Fig. 3.1 and 3.2). Consequently, water is drawn from the cells into the intercellular space. This dehydration will protect the cells up to a certain limit, due to the increase in intracellular solute concentrations, which lowers the freezing point by an additional 1 – 2 °C. However, as freezing continues, severe dehydration of the cell results in coagulation. The normal bilayer structure of the cell membrane will be disrupted forming water-filled channels that make the membrane porous.

When the ice melts, large amounts of solute will leak between the cell compartments and from the cells. Membrane proteins may be displaced and the membrane loses its selective characteristics, resulting in a loss of enzyme activity. This can be lethal to the cell and manifests itself as flaccidity and/or discolouration of the tissue.

If the cell death is limited and happens during blooming (i.e. anthesis, a period of rapid cell division) the plant will be able to recover rapidly. However, damage inflicted before anthesis will persist throughout fruit maturation. Although the buds may appear undamaged on the outside, internal damage can manifest as browning at a later stage.

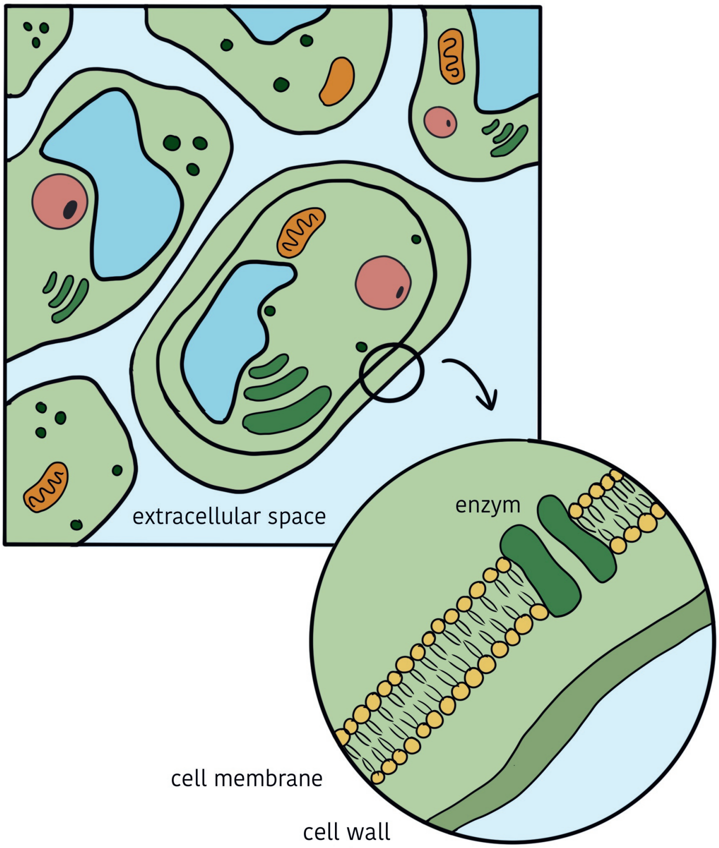

Figure 3.1: Sketch of a plant cell.

Flowers at full bloom show the damage as browning at the base of the style and, depending on the species, in other organs as well. The damage will become visible in the fruit as they ripen, often evidenced by the breaking of the weakened skin and the formation of healing cork tissue. Such damage reduces the quality, appearance and value of the fruit.

The temperature conditions during a frost night (e.g. intensity and duration of low temperatures, rates of temperature decrease, and thawing) determine the severity of the frost experienced by the plant. These conditions, as well as other environmental conditions such a wind and clouds, regulate the size and formation speed of ice crystals and affect the cells' ability to reabsorb water.

Box 1: High temperature stress

Under conditions of high solar radiation or elevated temperatures, plant temperatures can rise to 5 K or more above the ambient temperature. Many plants attempt to prevent overheating by adopting strategies such as vertical leaves, reflective hairs or waxy coatings that reflect light, or small dissected leaves that minimise the leaf boundary layer thickness. However, many of these techniques also reduce transpiration, a natural cooling mechanism to cope with high temperature stress (Hopkins, Hüner, et al., 1995).

Traditionally, it was believed that overheating was problematic as it resulted in irreversible protein denaturation. This is however only part of the problem, as high temperature stress also affects for example membrane fluidity (Wahid et al., 2007).

As the temperature becomes too low, the membrane crystallises. As the temperature becomes too high, the kinetic energy of the membrane molecules increases and the membrane loses its integrity and selective character. The cellular membrane consists of lipids with hydrophobic heads and two hydrophilic tails. These tails are fatty acids, some saturated and others unsaturated. Saturated fatty acids solidify at higher temperatures than unsaturated fatty acids. The ratio between saturated and unsaturated fatty acids therefore determines the transition temperature at which the membrane transitions from a crystalline to a fluid state. This is especially important in a cold environment where plants with more unsaturated fatty acids solidify at a lower temperature, and are thus more cold resistant (Raison et al., 1980). Under conditions of heat stress the number of unsaturated fatty acids increases, making the membrane more fluid. More heat-tolerant species therefore have a higher ratio of saturated fatty acids (Wahid et al., 2007).

3.3. COLD HARDINESS

Plants have developed mechanisms to cope with freezing stress to limit the degree of frost damage. They can resist stress through two main strategies: avoidance and tolerance (Snyder & De Melo-abreu, 2005).

Frost-avoidant species prevent their exposure to cold temperatures, for instance, by growing deep within the canopy where they are shielded from radiative cooling. On the other hand, frost-tolerant species avoid ice crystal formation when exposed to freezing temperatures. An interesting example of frost tolerance is the reduced leaf wettability observed in plants at high altitudes and in open areas where low nighttime temperatures and dew fall are common (Aryal & Neuner, 2010). Leaves with a lower wettability have a reduced contact area between water/ice and the epidermis, decreasing the likelihood of extrinsic ice formation that could lead to intrinsic ice formation. This reduction in leaf wettability thus promotes supercooling (Wisniewski et al., 2002; Fuller et al., 2003).

This tolerance mechanism is heritable, and represents a form of species adaptation. This is opposed to acclimation; a non-heritable physiological modification that results from gradual exposure to the stress. The biochemical processes that allow the plant to withstand crystal formation and dehydration, are known as hardening (Wisniewski et al.,

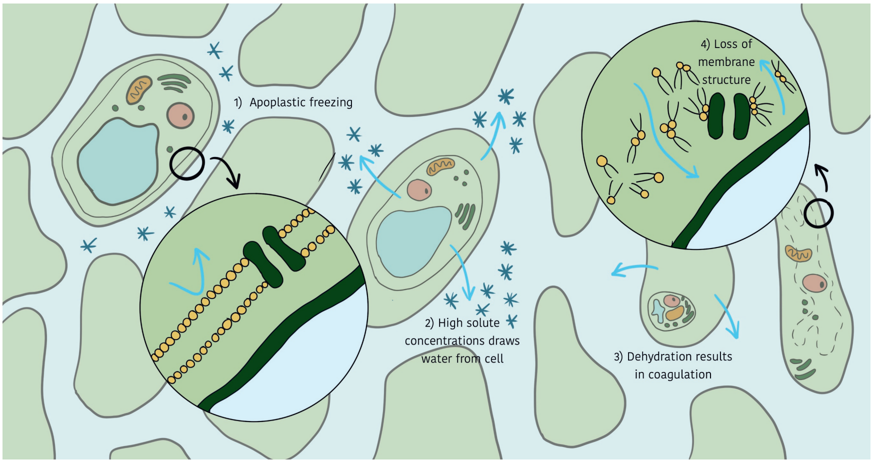

Figure 3.2: Illustration of freezing within a plant cell, from left to right the temperature decreases.

2014). After a winter or early spring with significant exposure to chilling temperatures, the degree of hardiness is higher. As a flower develops from dormancy to fruit set, the vulnerability of the vital organs increases, and cold hardiness thus decreases. Unfortunately, the mechanisms behind cold hardiness remain complex and not fully understood. Several factors have been reported to play a role, including changes in ice nucleation agents (Ashworth & Kieft, 1992), moisture content (Hewett et al., 1978) and nutrition status (Alden & Hermann, 1971; Khanizadeh et al., 1992; Flinn & Ashworth, 1995).

3.4. CRITICAL TEMPERATURE RANGES FOR FROST PREVENTION

The dependency on (prior) weather conditions makes predicting frost damage challenging. To determine whether protective measures are necessary, farmers often monitor whether the air temperature falls within a specific temperature range. This range is known as the critical temperature range: the temperatures at which 10% - 90% of the flower buds freeze at various stages of development. Due to the many factors that influence cold hardiness, the magnitudes of these ranges are broad typically between 3 – 10 °C (Wisniewski et al., 2014; Rodrigo, 2000; Lu & Rieger, 1993). The temperature ranges are published widely, but their origins and determination methods are not well-documented. Modern fruit farmers often still rely on old fruit bud charts, such as those based on Proebsting and Mills (1978), even for new cultivars.

Recently, Miranda et al. (2005), Salazar-Gutiérrez et al. (2016) and Matzneller et al. (2016) have sought to re-determine critical temperatures for new cultivars using modern techniques, such as cold chambers and differential thermal analysis (DTA). In DTA, thermoelectric modules are used to detect the freezing exotherm corresponding to the release of heat due to ice formation. An example of such a freezing exotherm is shown in Figure 3.3. The samples are cooled to below the freezing point of water in a cold chamber. Initially, no ice forms until the first apoplastic water freezes at -6 °C to -8 °C, causing the first exotherm. As the water consequently moves from the cell to the apoplast, a

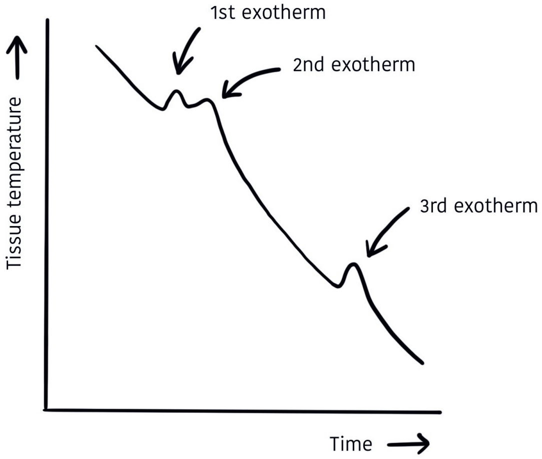

Figure 3.3: Freezing exotherms (figure adapted from Yu and Lee (2020)).

second exotherm occurs. Eventually, the third exotherm results from the freezing of the intracellular water.

However, these tests cannot be used to study how freezing occurs in the field for two reasons. First, modern freezing tests typically use convective freezing chambers. This freezing process does not accurately mimic radiative frost conditions, due to the absence of a temperature gradient and dew formation. This has significant effects on how the plants freeze and whether they survive. Additionally, the tests often require the detachment of a plant part from the whole plant. Field experiments using intact plants (Ashworth et al., 1985) and attached evergreen leaves, have shown that ice nucleation temperatures can be up to 3 °C higher in the field compared to freezing chambers (Taschler & Neuner, 2004). Second, limitations of the DTA method are that it can not be used to determine where freezing initiates, the rate of ice propagation or how many ice nucleation events are needed to freeze a whole plant.

The development of higher-resolution thermal cameras could help to address these gaps. Very few attempts have been made to study freezing under natural night frost situations by infrared technology (e.g. Pearce & Fuller, 2001; Hacker & Neuner, 2008; Frederiks et al., 2012). Charrier et al. (2017) distinguished three distinct freezing patterns in European spruces: 1) tree top to base, 2) from base to top, and 3) from thin branch to thick stem. These variations likely result not only from differences within the tree, but also from the interactions with microclimate.

3.5. THERMAL CAMERA: PROOF OF CONCEPT

Thermal cameras seem to be a promising solution to study spring frost in orchards in a field setting. The potential of an off-the-shelf infrared camera (Optris PI 450i) for this purpose was tested during a research visit at Cornell University. First we needed to test whether the camera was able to capture the nucleation events. This was done in a

Table 3.1: Critical temperatures for apple based on Proebsting and Mills (1978).

Bud development stage	Bud	Leaves	Flower
Avg. temp for 10% kill (°C)	-9.4 – -7.8	-5.0 – -2.8	-2.2
Avg. temp for 90% kill (°C)	-17 – -12	-9.4 – -6.1	-4.4 – -3.9

controlled freezer setting. Since the research visit lasted only three months, we did not have the time do test the camera in the field. Here, we thus applied the camera to answer the following question:

Can the camera be used to capture the ice nucleation from dormancy to fruit set?

To test frost hardiness throughout different development stages in a single run, we needed to have samples at various development stages available at the same time. To this end, we manipulated the development of the apple cuttings.

At the start of spring, 60 cuttings with dormant flower buds were cut in the field and stored in a dark cool room at 5 °C. This paused their development keeping them in their dormant stage. Over the next two weeks, every three days, ten cuttings were taken out and placed in a room at room temperature. This method provided us with a selection of samples ranging from dormant to pink stage (Chapman & Catlin, 1976). The trial was done three times with different cultivars: Jonagold, a popular cultivar in the Netherlands; Honeycrisp, a popular cultivar in the United States; and SweeTango, a young cultivar developed at the University of Minnesota.

The samples were frozen in a convective freezer. The internal and external temperatures of the buds were tracked using two different measurement techniques. Internal bud temperatures were measured using small thermocouples inserted into the buds or between the flower petals. Skin temperatures were recorded using a thermal camera. Both techniques showed similar trends, with the internal temperature being 1 – 1.5 °C above the skin temperature. This experimental setup and an example of a thermal image is demonstrated in Figure 3.4.

To determine the freezing point, the freezer was programmed to cool to -10 °C over the course of two hours. The internal temperatures observed for all three cultivars are presented in Figure 3.5. We grouped them into three broad development stage ranges: 1) buds: dormant, silver tip and green tip; 2) leaves: half-inch green and tight cluster; 3) flowers: pink. As this experiment was designed to be a proof of concept, we kept the number of samples low and limited the number of freezer runs. Although the sample size is too low to draw significant conclusions, the thermocouple observations suggest the following freezing order: buds and leaves freeze first, followed by flowers. Based on the critical temperatures (Table 3.1), one might expect flowers to freeze before leaves and buds. However, our observations indicate the opposite, which suggests that cold hardiness may not be solely due to the absence of ice formation but rather a tolerance to ice formation. In other words, freezing may occur without causing lethal damage. To confirm this theory, further testing for browning in buds and flowers after freezing would be necessary, as this would indicate whether damage occurred.

The question remained whether freezing occurred due to the duration of exposure or

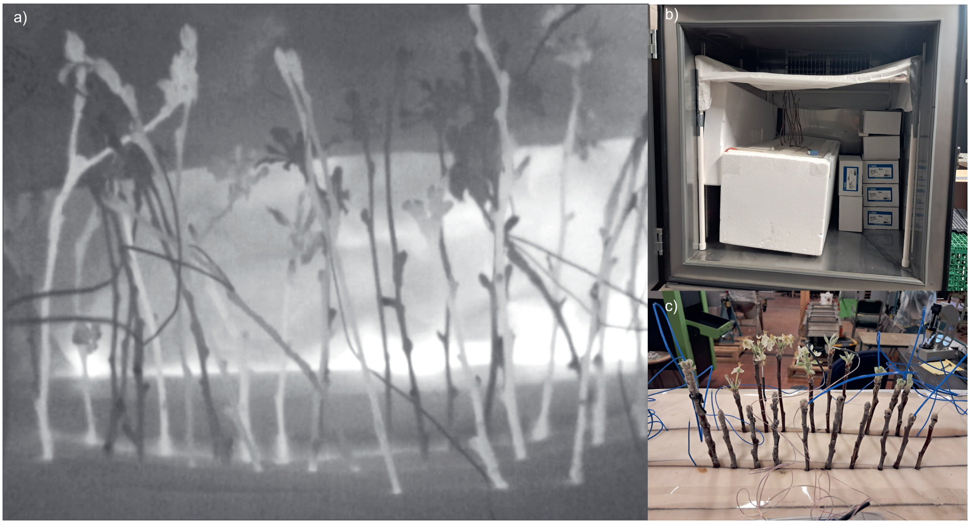

Figure 3.4: Thermal imaging setup and snapshot. Panel a) shows a snapshot from the freezing video. The light colours show relatively warm regions. Some of the cuttings are already frozen and show up as white in the thermal image. The freezing exotherm caused the temperature of the cuttings to rise, which caused them to be relatively warm compared to the supercooled unfrozen cuttings. The white square in the back is caused by the relatively warm insulating material. Panel b) shows the freezer with a foam box that holds the cuttings in place, protecting the cut ends from freezing. The thermal camera is kept from freezing in an insulated cardboard box. Panel c) shows the cuttings at different development stages. At the end of the blue cables is a thermocouple, inserted in the buds and flowers.

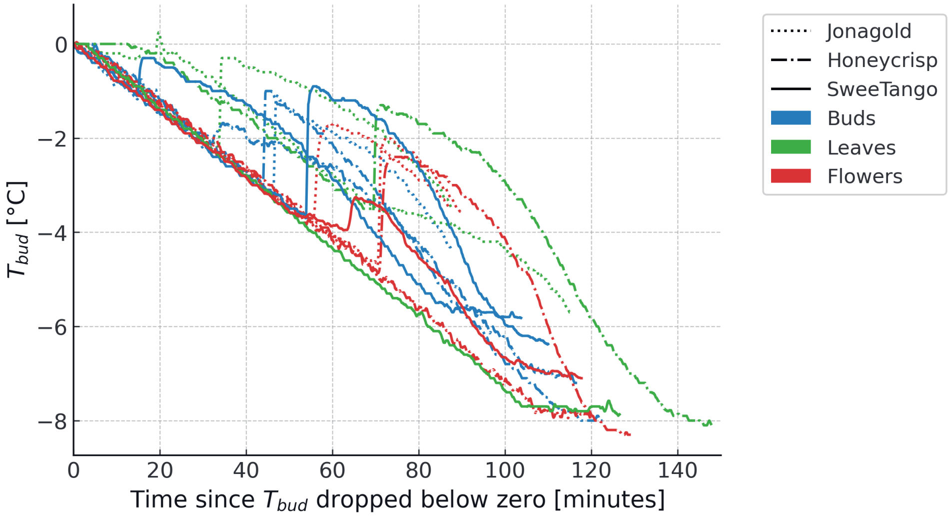

Figure 3.5: Internal bud temperatures measured with the thermocouples. The sudden increase in temperature is the first freezing exotherm (Figure 3.3).

Table 3.2: Results from thermal camera. The temperature column includes the skin temperatures of the buds and flowers just before the freezing exotherm. The time is the time since the air temperature dropped below 0 °C. The ranges indicate the differences between the cuttings.

Cultivar	**Freezer setting**	**Temperature (°C)**	**Time (min)**
Jonagold	Cooling from 0 to -8 °C in 2.5 hours	-3.5 – -6.5	65 - 110
SweeTango	Cooling from 0 to -8 °C in 2.5 hours	-3.5 – -6	65 - 95
Honey Crisp	Cooling from 0 to -8 °C in 2.5 hours	-4 – -6.5	75 - 105
Jonagold	-3 °C	-3.5	0 - 90
SweeTango	-2 °C	-3 – -3.5	15 - 75
Honey Crisp	Stepwise cooling from 0 to -4 °C with 0.5 °C hourly intervals	-3.5 – 4	0 - 90

because the temperature dropped below a specific threshold—or perhaps a combination of both. To distinguish between these causes, we exposed the samples to a constant temperature just above the observed freezing threshold for each cultivar. If freezing still occurred, it would likely be attributed to the length of exposure rather than the temperature alone. However, it proved quite a practical challenge to set the freezer at the correct threshold temperature.

During the first ramp run (Jonagold), the first flower froze at a skin temperature of -3.5 °C, after ~ 65 minutes of exposure to sub-zero temperatures. Within an hour, all samples had frozen. Therefore, in the constant temperature run, we set the temperature to drop from 0 to -3 °C over 10 minutes, then maintained it at -3 °C for two hours to see if freezing would still occur or not.

Despite the air temperature in the front section of the freezer not dropping below -1 °C, the dormant buds in the back cooled to -3.5 °C. Immediate freezing was observed as the temperature dropped below -3.5 °C. In the next run we therefore placed more thermocouples to measure spatial variation in the air temperature, and observed about a degree difference.

Therefore, for SweeTango, we kept the programmed temperature at -2 °C instead. We saw only one flower freeze after 15 minutes and one bud after 75 minutes at this temperature. This suggests that the freezing results from time of exposure. However, the final run with Honeycrisp suggests that freezing is triggered by temperature dropping below a threshold value. Here, we used a stepwise cooling approach, decreasing the temperature by 0.5°C at hourly intervals and freezing occurred within the first 5 minutes of every step.

To draw significant conclusions from this experiment, it needs to be scaled up to a large number of samples. We showed that this can be done with a thermal camera, as the camera was able to capture the freezing exotherms of the individual cuttings. Not shown in this thesis are the thermal camera videos. They allow us to detect the starting point of nucleation and the propagation rate.

4

RETHINKING THE ROUGHNESS HEIGHT

Make everything as simple as possible, but not simpler.

Albert Einstein

This chapter has been originally published as:
Boekee, J., van der Linden, S. J., ten Veldhuis, M. C., Verouden, I. E., Nollen, P. J., Dai, Y., Jongen, H. J. & van de Wiel, B. J. (2024). Rethinking the Roughness Height: An Improved Description of Temperature Profiles over Short Vegetation. Boundary-Layer Meteorology, 190(7), 31.

Summary

In this study, we present an extension to the Monin–Obukov similarity theory (MOST) for the roughness sublayer (RSL) over short vegetation. We test our theory using temperature measurements from fibre optic cables in an array-shaped setup. This provides a high vertical measurement resolution that enables us to measure the sharp temperature gradients near the surface.

It is well-known that MOST is invalid in the RSL as the flow is distorted by roughness elements. However, to derive the surface temperature, it is common practice to extrapolate the logarithmic profiles down to the surface through the RSL. Instead of logarithmic behaviour defined by MOST near the surface, our observations show near-linear temperature profiles. This log-to-linear transition is described over an aerodynamically smooth surface by the Van Driest equation in classical turbulence literature. Here we propose that the Van Driest equation can also be used to describe this transition over a rough surface, by replacing the viscous length scale with a surface length scale L_s that represents the size of the smallest eddies near the grass structures. We show that L_s scales with the geometry of the vegetation and that the model shows the potential to be scaled up to tall canopies. The adapted Van Driest model outperforms the roughness length concept in describing the temperature profiles near the surface and predicting the surface temperature.

4.1. INTRODUCTION

4.1.1. DIAGNOSIS OF THE PROBLEM

Accurate estimations of the surface temperature and momentum profiles are crucial to determine the exchange of energy and moisture between the surface and the atmosphere (Physick & Garratt, 1995; Holtslag et al., 2013). Yet, getting a good estimate of the temperature profile over the widespread and frequently studied grass surface remains challenging (e.g. Beljaars & Holtslag, 1991; Duynkerke, 1992; Sun, 1999; Best & Hopwood, 2001). Here, we present a (semi-) analytical model to describe vertical temperature profiles just centimetres above the grass. The framework is inspired by the well-known Van Driest equations (Van Driest, 1956) for flow in smooth channels and is now applied to a rough grass surface. We test our model using high-resolution temperature observations from fibre optic cables.

Traditionally, the temperature profiles in the atmospheric surface layer (ASL), the lowest 10% of the atmospheric boundary layer (Fig. 4.1a), are represented by the Monin–Obukov Similarity Theory (MOST) (Monin & Obukov, 1954; Foken, 2006). This theory relates the vertical gradients of transported quantities to stability and surface fluxes via the law of the wall: large turbulent eddies are broken down into smaller eddies closer to the surface (von Kármán, 1930). This results in the characteristic logarithmic behaviour of the wind and temperature profiles.

From turbulent channel flow, we know that over a flat surface, the logarithmic profiles naturally transition to linear profiles in the viscous sublayer. As turbulent mixing lengths decrease (i.e. the turbulent eddies become smaller), viscous transport takes over (Prandtl, 1905). From the surface upwards, we can therefore recognise a viscous sublayer, a buffer layer and a log layer (Fig. 4.1b). Their heights are well-defined in terms of dimensionless distance to the wall (Kundu et al., 2016).

For a natural, vegetated surface, such a normalisation becomes complex. Since grass is three-dimensional, consisting of individual vertical blades, the viscous sublayer follows the shape of the leaves and is orders of magnitude smaller than the grass height (Fig. 4.1a). Such a surface is considered aerodynamically rough. Here, the air has to flow around individual roughness obstacles and this disturbs the profiles from their logarithmic shape. This part of the atmospheric sublayer is called the roughness sublayer (RSL): the layer in which the flow is influenced by the spatial variation of the rough surface (Raupach et al., 1980). The RSL stretches from the surface up to 2–5 times the height of the roughness elements. As the flow is influenced by the individual roughness elements, the MOST equations are only valid above the RSL.

Special RSL modifications to the MOST theory have been introduced e.g. Harman and Finnigan, 2007, 2008; De Ridder, 2010 and tested for tall canopies (Ryder et al., 2016; Chen et al., 2016; Bonan et al., 2018). However, for *short* vegetation such as grass, it is still common practice to extrapolate the logarithmic profiles to the surface (or the displacement height d (Thom, 1971) through the RSL (Viterbo & Beljaars, 1995; Mitchell, 2005; Clark et al., 2010; Meier et al., 2022; Zhang et al., 2022).

If the surface height were defined at $z = 0$, mathematically speaking the surface temperature and wind speed are undefined, as the logarithm goes to minus infinity. To overcome this, the roughness heights for heat and momentum have been introduced. In the case of momentum, the roughness height z_{0m} is defined as the height where wind

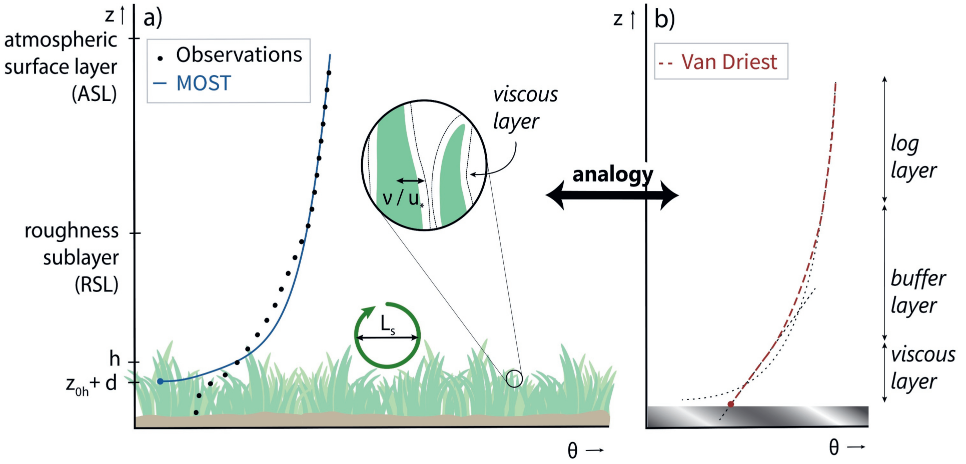

Figure 4.1: Visualisation of the analogy between the Monin–Obukov model and the Van Driest model. Panel a) shows the Monin–Obukov model for near-surface temperatures highlighting the difference in RSL temperature (θ) between the model (blue line) and observations (black dots). Panel b) shows the different layers used in the Van Driest model for flow over a smooth surface. The green eddy and round inset show the scale difference between the viscous length scale (ν/u_*) and a surface length scale, L_s. Here h represents the grass height, z_{0h} the roughness height for heat, and d the displacement height.

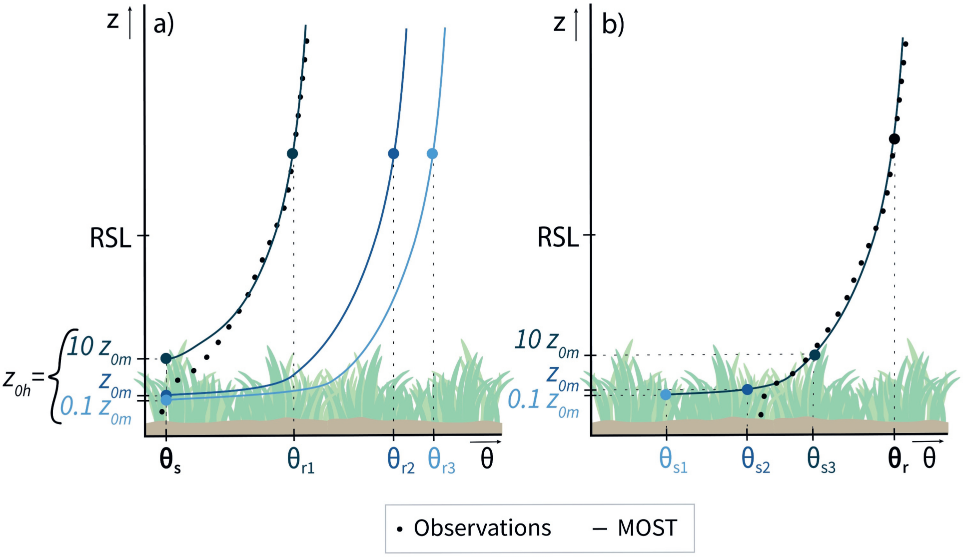

Figure 4.2: Sketch highlighting the consequences of the extrapolation of the logarithmic profile down to the surface and the uncertainty in z_{0h}. The black dots show observed temperatures, and the blue lines possible MOST profiles for a range of z_{0h} values. To match observations above the RSL and the surface temperature non-physical z_{0h} values may be needed. Panel a) shows how a relatively small difference in z_{0h}/z_{0m} can propagate as a large difference in temperature above the RSL ($[\theta_{r1}, \theta_{r2}, \theta_{r3}]$). Panel b) shows the reverse problem, how for a known reference temperature, a small difference in z_{0h} results in a large difference in surface temperatures ($[\theta_{s1}, \theta_{s2}, \theta_{s3}]$).

speed decreases to its surface value (i.e., zero). It is *assumed* that a similar concept can be applied to heat. So, the roughness height for heat z_{0h} is the height where the temperature equals the surface temperature.

To estimate z_{0h}, often a fixed ratio of 0.1 relative to z_{0m} is assumed (Beljaars & Holtslag, 1991; Garratt & Hicks, 1973; Garratt & Francey, 1978; Brutsaert, 1982), since the underlying physical mechanisms responsible for these transports differ. Heat exchange at the surface occurs by less effective molecular diffusion, while momentum is exchanged through (form) drag caused by pressure effects.

However, even for the same site, it was shown that the ratio z_{0h}/z_{0m} can vary up to 6 orders of magnitude (Duynkerke, 1992). The consequences of this uncertainty are significant due to the logarithmic shape of the profiles. This is illustrated in Fig. 4.2. For a given surface temperature (derived from radiation measurements), an uncertain z_{0h}/z_{0m} ratio results in a wide spread of predicted temperatures higher up in the temperature profile (Fig. 4.2a). Conversely, when for example the 1.5 m temperature is measured in situ, the predicted surface temperature for a slightly different z_{0h} can show a large divergence due to the large gradients near the surface (Fig. 4.2b).

The robustness of the ratio between z_{0h}/z_{0m} has been the subject of many earlier studies (e.g. Beljaars & Holtslag, 1991; Sun, 1999; Brutsaert, 1982; Andreas, 1987; Blyth & Dolman, 1995; Zilitinkevich, 1995; Verhoef, De Bruin, & Van Den Hurk, 1997; Massman, 1999; Blümel, 1999; Chaney et al., 2016; Rigden et al., 2018). Partly, its uncertainty lies in the fact that it cannot be measured directly, but must be derived from the measurements of other quantities. In particular, the surface temperature (Garratt et al., 1993; Su et al., 2001) proves challenging.

It is common practice to use the radiative temperature as the surface temperature in MOST. That signal is a composite of the *skin* temperature of different surface types within the view of the pyrgeometer (e.g. bare soil, dry grass, living grass). To derive z_{0h} and apply MOST correctly, we need to know the *effective* surface temperature, i.e. the temperature of the *air* that is in contact with the roughness elements (vegetation, soil, etc.) (Garratt et al., 1993). A recent study by Hicks and Eash (2021) highlights how these temperatures derived from infrared radiation can differ from the effective surface temperature by up to 2K during the day.

However, we argue that another important source of uncertainty stems from the incorrectness of the underlying physical model. Extrapolating the logarithmic profile down to the surface implies a decrease in the eddy size to zero towards the surface. A vanishing length scale leads to an infinite gradient, which is a non-physical asymptotic limit.

In this paper, we therefore propose a more physics-based approach to describe near-surface temperatures, thereby enhancing the robustness of heat transfer parameters near the surface.

4.1.2. ALTERNATIVE APPROACH: SURFACE LENGTH SCALE FOR SHORT CANOPIES

As explained, extrapolation of the logarithmic profile is still common practice for short canopies. This leads to nonphysical profiles in the RSL, which limits the generality of the z_{0h} concept. Eventually, this affects the modelling of the full ASL temperature profile. We therefore aim to provide a more physical description of the temperature profile over short vegetation. Such a description should have a gradient of finite magnitude near the surface and asymptotically merge into the traditional log layer higher up in the atmosphere. With finite gradient, we imply e.g. a linear, quadratic or exponential temperature profile, rather than logarithmic.

Van Driest (1956) describes such an asymptotic transition from the log layer into the viscous layer for smooth channel flow. The Van Driest equation is based on first principles, closely follows laboratory measurements (Monin & Yaglom, 1973) and was later also confirmed by direct numerical simulations (e.g. Donda et al., 2014). For our new formulation, we adapt the existing Van Driest equation by replacing the viscous length scale with a characteristic surface length scale. However, we would like to emphasise here, that although we choose a Van Driest-inspired model description, alternative formulations are also possible.

The empirical RSL models available for tall canopies include a similar surface length scale. This length scale represents the size of the dominant turbulent eddies that scale with the canopy height (Raupach et al., 1996). Also for short canopies, we expect that the surface length scale scales with the canopy geometry. Just like tall canopies, the grass surface is rough and partly permeable, which results in shear instabilities and vortex shedding at the top. We hypothesise that the minimal eddy size at the surface is *finite* and determined by the distance between the clustered groups of grass leaves (Fig. 4.1a). The actual eddy size near the top of the grass is therefore larger than anticipated through a proportional relationship with z as assumed when extrapolating the log-law. Moreover, it is orders of magnitude larger than the viscous length scale.

Due to the lack of a method for high-resolution temperature measurements, it has not been possible to observe the actual shape of the temperature profiles near the surface over short vegetation until recently. We apply Distributed Temperature Sensing (DTS) for temperature sampling at a high spatial and temporal resolution. DTS is a technique that uses fibre-optic cables as temperature sensing elements (Selker et al., 2006; Tyler et al., 2009). This enables measurements of the small-scale and rapidly changing gradients and individual turbulent eddies. By installing the cable in different configurations such as coils (Sigmund et al., 2017; Zeller et al., 2021), or arrays (Thomas et al., 2012a), sharp temperature gradients near the surface can be measured. Here, we apply a harp-shaped DTS set-up to measure the temperature profile over and within the grass with 2 cm resolution.

In Sect. 4.2, we describe the field measurements and introduce the adapted Van Driest model. In Sect. 4.3, the adapted Van Driest model will be compared to the observations and the roughness length concept. Additionally, we will illustrate the model's equivalence to established tall-canopy models. Finally, Sect. 4.4 summarises conclusions and provides an outlook on further applications of the new model concept.

4.2. METHOD

4.2.1. HIGH RESOLUTION TEMPERATURE PROFILES, EXPERIMENTAL SET-UP

The supporting measurement campaign took place at the Veenkampen meteorological site in the Netherlands (51.98° N, 5.62° E), between 1 to 24 May 2022. This site has been operated and maintained by Wageningen University & Research since 2011. Here we installed DTS cables to measure temperature profiles at two vertical resolutions: a 9-m mast with 25-cm resolution, and a 64 cm high harp-shaped configuration with 2-cm resolution (Fig. 4.3).

DTS uses the backscatter of a laser signal to infer local temperature at different cable sections with a sampling resolution of 25 cm and 10 s (Thomas et al., 2012a). A thin, white, 1.6 mm fibre optic cable and an Ultima-M system were used. The data calibration was done using the DTS Calibration Python package (des Tombe et al., 2020). Two well-mixed calibration baths were kept in the maintenance hut: one at ambient temperature (~ 19 °C) and one heated (~ 35 °C). The baths were placed at the start and end of the cable to allow for a double-ended configuration.

For the mast, two vertical DTS cables were extended along a support structure. The temperatures recorded by the two cables deviate by 1 – 2 K from each other near the surface and the top of the mast. This is most likely due to the influence of the support structure on the airflow. We therefore only considered the cable closest to the harp in our analyses and excluded the upper and lower 30 cm.

The harp consisted of horizontal layers of cable that were 2 cm apart. This resulted in a vertical measurement resolution of 2 cm, with 30 temperature observations per measurement height, from 2 cm above the surface up to 64 cm. The cables were glued to a fibreglass mesh every meter, to maintain alignment and keep sagging to within 1 cm. The harp was split into 4 measurement sections, each ~ 2 m long (Fig. 4.3). Along these sections, different mowing regimes were applied. Measurements were averaged horizontally along sections to reduce sensitivity to spatial variation.

The grass height along the DTS harp was recorded (and maintained) every 3 days. Four mowing regimes were applied: at fixed heights of 3 cm, 10 cm, and 20 cm, and a variable section where grass grew naturally from 3 cm to over 20 cm. Grass heights including variation within a plot, are provided in Appendix A.2, Fig. A.2. In our analyses, we focused on the 10 cm grass plot, unless stated otherwise, in agreement with the dominant grass height in the surrounding fields.

The Veenkampen automated weather station provides 10-minute averages of several meteorological variables, of which we used the radiation, eddy covariance and sonic-anemometer measurements (wind direction and wind speed at 2 m). We verified the DTS measurement using the shielded and ventilated 1.5 m and shielded 0.1 m temperature measurements (Sect. 4.3.1). Additionally, we used the longwave radiative measurements of the pyrgeometer to derive the surface skin temperature.

The soil at the Veenkampen site consists of a clay layer down to 1 m depth, on top of peat. The groundwater level during the experiment varied between -0.8 m and -0.6 m. The site was sown with ryegrass in 2011, and the grass height is kept at approximately 10 cm. Neighbouring fields are not maintained and here grass and reeds up to 1.5 m can be found (Schulte et al., 2021). The 17-ha field is surrounded by ditches, where the water level was close to the surface during the experiment. The field is located in a flat area, with a 50 m moraine at a 4 km distance.

During the measurement period, the weather conditions were relatively constant with mostly warm and sunny days without precipitation. The only precipitation occurred during a heavy thunderstorm with measured wind gusts of up to 30 m s^{-1} at 10 m. The storm ripped the harp on 19 May 2022 at 12.30 UTC. We repaired the harp on 21 May 2022. Observations from 19 May 2022 till 21 May 2022 were therefore not included in the analyses.

When the wind direction was perpendicular to the harp, the airflow was deflected due to the fibreglass mesh. This resulted in temperature profiles that were not representative of the undisturbed surroundings. We therefore excluded observations from wind directions 45° - 135° relative to the harp. This was the case 43% of the time. After 10-minute averaging and filtering, 1350 timestamps were retained for analysis.

4.2.2. ADAPTED VAN DRIEST MODEL

Our new formulation is an adapted version of the Van Driest model for momentum transport in smooth channel flow (Van Driest, 1956). Van Driest (1956) introduced a model for the buffer layer where the eddy diffusivity (or rather turbulent velocity fluctuations) gradually decreases to zero in the viscous layer, instead of a hard boundary between the viscous and logarithmic layer. Therefore the eddy diffusivity model can be used in the entire surface layer through the introduction of a damping function A. A expresses the damping effect of the wall on the eddy diffusivity with $A = 1 - \exp(-\beta z)$, where $\beta \approx 1/26$ is an empirical constant for smooth walls. Donda et al. (2014) adapted the Van Driest formulation to correct for stability effects that dominate with increasing distance to the wall. They describe the turbulence near a smooth wall using the following equation:

$$u_* = \left[\frac{(A\kappa z)^2 \frac{\partial u}{\partial z}}{u_* \left(\Phi_m\left(\frac{z}{L_{ob}}\right)\right)^2} + (\nu/u_*) \right] \frac{\partial u}{\partial z}. \tag{4.1}$$

Here, u is the wind speed, u_* the friction velocity, κ the Von Kármán constant of 0.4. Function Φ_m is the similarity function for momentum and depends on the stability of the atmosphere via the Obukov length L_{Ob}. We used the formulations by Dyer (1974).

We hypothesised that for a rough grass surface, the logarithmic layer does not continue into a viscous layer, but instead continues into a layer where the eddy size is determined by the geometry of the vegetation. The individual roughness elements, i.e. individual grass leaves and clustered groups (i.e. tussocks), prescribe the minimum eddy size close to the surface. Note that, also with a well-maintained grass height, significant structural variation exists, which will promote mixing at the top of the grass (Fig. A.2).

We hence replaced the original viscous length scale ν/u_* in the Van Driest equation with a surface length scale L_s. L_s represents the smallest eddies just over and within the grass (Fig. 4.1a). Additionally, we applied the similarity assumptions and replaced momentum with heat. This gives an adapted Van Driest formulation:

$$\theta_* = \left[\frac{(A\kappa z)^2 \frac{\partial \theta}{\partial z}}{\theta_* \left(\Phi_h\left(\frac{z}{L_{ob}}\right)\right)^2} + L_s \right] \frac{\partial \theta}{\partial z} \tag{4.2}$$

where θ is the potential temperature and θ_* is the turbulent temperature scale. The function Φ_h is the similarity function for heat:

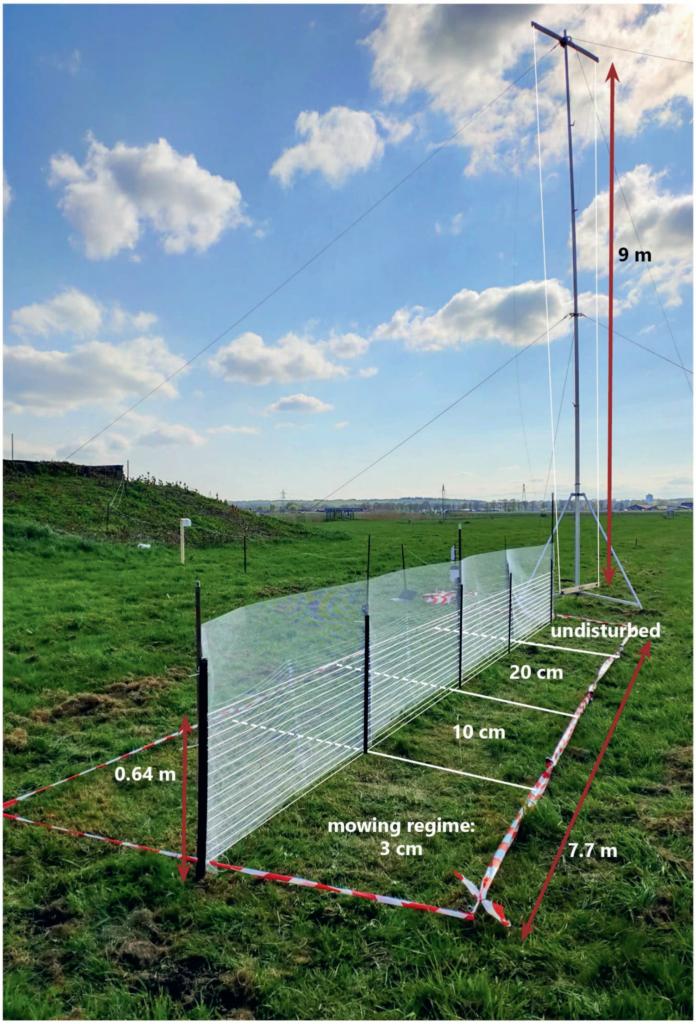

Figure 4.3: DTS field set-up at the Veenkampen measurement site showing the harp and mast. The DTS cables are sketched in white for visualisation purposes. The grass heights are written in their respective plots. The relative widths of the plots are (from front to back): 2.09 m, 2.06 m, 1.85 m, 1.70 m. The maintenance hut is visible in the back.

$$\begin{array}{c}\Phi_h = \left(1-16\tfrac{z}{L}\right)^{-1/2} \text{ for } \tfrac{z}{L} \leq 0 \\ \Phi_h = \left(1+5\tfrac{z}{L}\right) \text{ for } \tfrac{z}{L} \geq 0\end{array} \tag{4.3}$$

The distinctive feature of the adapted Van Driest equation compared to MOST is the introduction of a finite gradient, i.e. linear temperature profile, within the roughness sublayer. Note the limits of this formulation: close to the surface (small z) the linear velocity profile in the roughness sublayer is obtained, whereas for larger z MOST is recovered. Above the RSL, the formulation asymptotically approaches MOST and the *gradients* are identical to the traditional MOST framework. The temperature itself is not per se the same, as different boundary conditions may result in a different offset.

Our new RSL description was compared to the MOST formulation. The MOST equation for the temperature gradient with height is:

$$\frac{\partial\theta}{\partial z}\frac{\kappa z}{\theta_*} = \Phi_h\left(\frac{z}{L_{Ob}}\right). \tag{4.4}$$

In its integrated form from the surface to height z, Eq. 4.4 becomes:

$$\theta(z) - \theta_s = \frac{\theta_*}{\kappa}\left[\ln\left(\frac{z}{z_{0h}}\right) - \Psi_h\left(\frac{z}{L_{Ob}}\right) + \Psi_h\left(\frac{z_{0h}}{L_{Ob}}\right)\right], \tag{4.5}$$

with θ_s as the surface temperature, and Ψ_H the integrated form of the similarity functions.

To compare the MOST and adapted Van Driest model to each other and the observations, we needed a non-dimensional form of the equations. In the classical MOST framework, potential temperature is normalised using the turbulent heat flux scale θ_* and height using the Obukov length L_{Ob} in the form of z/L_{Ob}. In the Van Driest model a different length scale is introduced, the viscous length scale ν/u_* (c.q. L_s in our adaptation).

To apply the normalisation, we needed a first guess of L_s. By applying Eq. 4.2 in the limit for $z \rightarrow 0$ we derived:

$$\lim_{z\rightarrow 0}\theta_* = [0 + L_s]\lim_{z\rightarrow 0}\frac{\partial\theta}{\partial z} \tag{4.6}$$

$$L_s = \frac{\theta_*}{\frac{\partial\theta}{\partial z}_{z\rightarrow 0}} \tag{4.7}$$

Note here the analogy with the vorticity thickness used for tall canopies, which will be elaborated in Sect. 4.3.5.

Normalising MOST by θ_* and L_s gives:

$$\frac{\partial\hat{\theta}}{\partial\hat{z}}\frac{\kappa\hat{z}}{1} = \Phi_h\left(\frac{\hat{z}}{\hat{L}}\right), \tag{4.8}$$

in which $\hat{\theta} = (\theta - \theta_s)/\theta_*$, $\hat{z} = z/L_s$ where $z = Z - d$, and $\hat{L} = L_{ob}/L_s$. Z is the height above the substrate (i.e. soil). d is the displacement height, assumed to be $\frac{2}{3}h$ (Shaw & Pereira, 1982), with h the grass height. θ_s was here taken as the temperature at the top of the grass.

The adapted Van Driest model after normalization, becomes:

$$1 = \left[\frac{(A\kappa \hat{z})^2 \frac{\partial \hat{\theta}}{\partial \hat{z}}}{\Phi_h(\frac{\hat{z}}{\hat{L}})^2} + 1 \right] \frac{\partial \hat{\theta}}{\partial \hat{z}} \tag{4.9}$$

Note that in the limit for $z \to 0$, $\frac{\partial \hat{\theta}}{\partial \hat{z}}$ in the adapted Van Driest model goes to 1, whereas in MOST it goes to infinity. Derivations of the normalised equations can be found in Appendix A.2.1.

4.3. RESULTS AND DISCUSSION

In this section, we first analyse the near-surface temperature profiles provided by the DTS measurements. Then, the adapted Van Driest model and roughness length model are compared to the DTS observations. Finally, we show how our model relates to the existing literature, as our adapted Van Driest approach closely resembles existing RSL models for tall canopies.

4.3.1. NEAR-SURFACE TEMPERATURE OBSERVATIONS

To assess the accuracy of the DTS measurements, the DTS temperatures were compared to the reference measurements at the Veenkampen site. Results are shown in Fig. 4.4 for a selection of days. A nearly constant bias of approximately +1 K was observed for the temperature at the DTS mast at 1.5 m, relative to the shielded and ventilated sensor, persisting during both day and night. The consistent sign of the bias suggests that the calibration, rather than radiation, was likely responsible for this effect. A similar bias of 1 K was observed for DTS observations at 10 cm height during the night, while the bias is near zero during the day.

We suspected that the daytime DTS temperature at 10 cm is also biased, yet remained undetected because tall grass obstructed the sensor. Had the sensor not been overgrown by the grass, it would probably have recorded a lower temperature during the day, subsequently revealing the +1 K bias of the DTS measurements. Given the uncertainty in the reference temperature, we did not apply a correction but assumed a 1 K measurement uncertainty.

It is common practice to use the radiative temperature as the surface temperature in MOST. The green dotted line in Fig. 4.4 shows the surface temperature derived from radiative measurements. This represents the skin temperature and not the air temperature. This difference can be 1 – 2 K at night, but up to 10 K during the day (compare the pyrgeometer to the 10 cm observations). Note that, MOST assumes knowledge of the near-surface air temperature and not *skin* temperature (Hicks & Eash, 2021). If one wants to use these radiative measurements in combination with MOST or the adapted Van Driest model, the skin temperature first needs to be translated to air temperature.

4.3.2. FINITE GRADIENT NEAR THE SURFACE?

For decreasing z the MOST model prescribes a temperature gradient approaching infinity at the surface (Eq. 4.4). In Sect. 4.1, we argued our belief that this is a non-physical boundary condition. Additionally, we hypothesised that instead, the surface gradient is

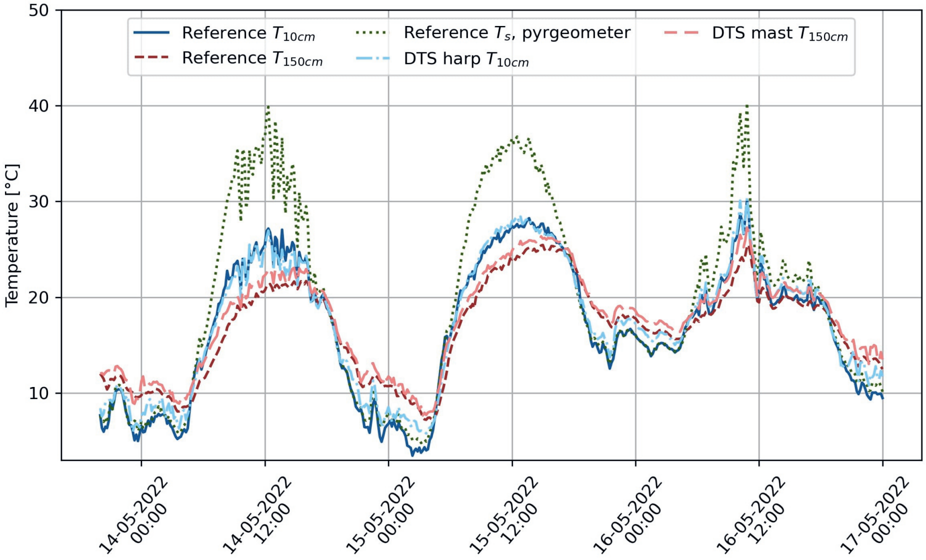

Figure 4.4: Temperature measurements with the DTS compared to the reference measurements at the Veenkampen measurement site during three radiatively different days and nights.

finite. Using the high-resolution temperature profiles measured with DTS we can evaluate this hypothesis. Figure 4.5 shows two examples of observed temperature profiles for stable (panel a) and unstable (panel b) conditions. Below 0.4 m (panel a) and 0.2 m (panel b), the observations no longer follow a logarithmic profile (shown as the blue line).

Next, we hypothesised that this profile in the RSL can be more accurately described with a linear approximation, inspired by the Van Driest equation. Figure 4.6 zooms in on the lower part of the temperature profiles and here the profile predicted by the adapted Van Driest model is added (at 1.4 m and 0.2 m for respectively Fig. 4.6 a and b). Above the RSL both models converge to the same gradient. In the RSL, the logarithmic profile transitions into a linear profile at the top of the grass. The absolute height at which the profile becomes linear depends on the stability (Eq. 4.2).

Figure 4.6 also highlights the difference in predicted surface temperatures using MOST and the adapted Van Driest model (i.e. -1.5 K for the stable, and 3.4 K for the unstable case). We derived the surface temperature from the locally observed 1.5 m temperature (DTS mast measurement) using Eq. 4.8 and Eq. 4.9. Values for θ_* and L_{Ob} were calculated from the sonic-anemometer observations. According to MOST (Eq. 4.5), the surface temperature was defined at $d + z_{0h} = 0.067$ m (blue star in Fig. 4.6). We used a displacement height of 2/3th of the grass height and took $z_{0h} = 0.1 \times z_{0m} = 0.001$ m. In the adapted Van Driest equation we took the surface temperature at the top of the grass (at 0.1 m) since we assumed that the linear profile approximation only applies above the vegetation layer. We point out that the lower boundary condition of the adapted Van Driest equation is still an open question. We suspect it is linked to the density at the top

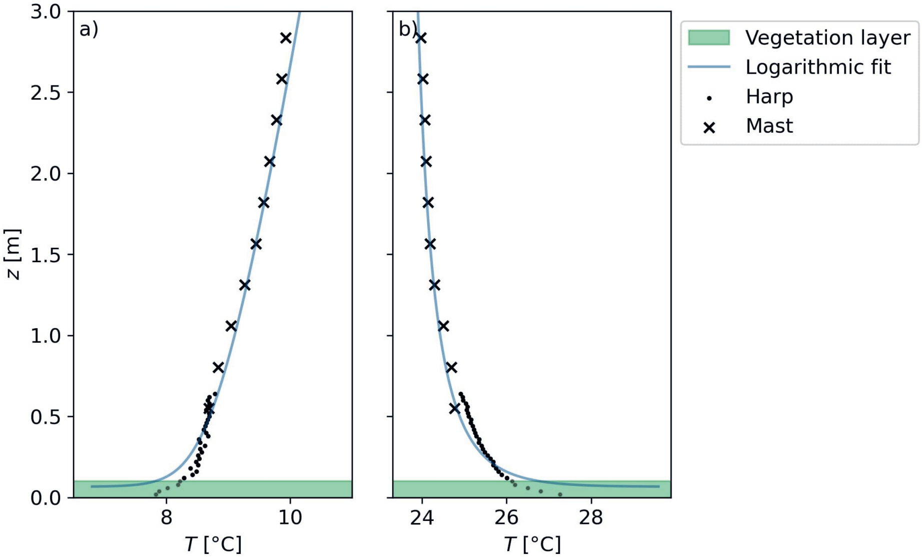

Figure 4.5: Examples of observed temperature profiles for panel a) a stable case (12 May 2022 0330 UTC L_{Ob} = 3) and panel b) an unstable case (18 May 2022 0900 UTC L_{Ob} = -12).

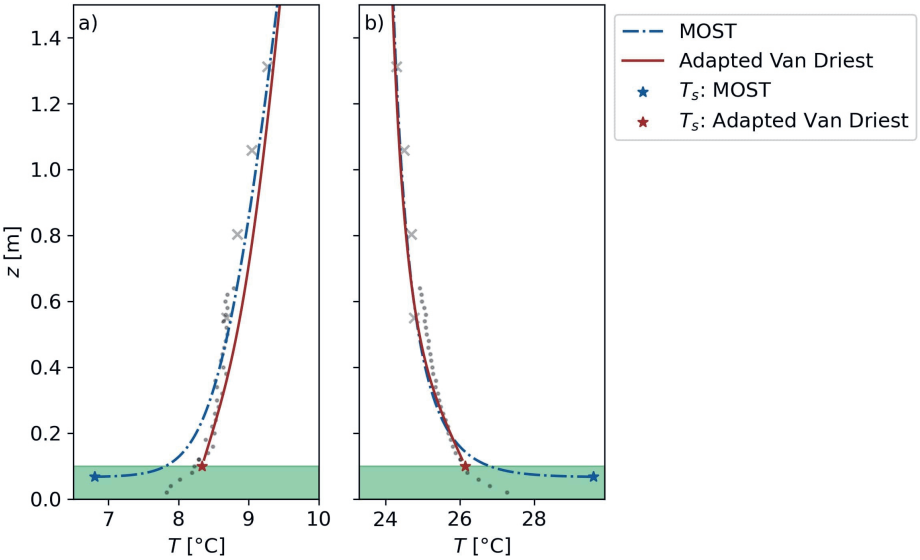

Figure 4.6: Examples of predicted temperature profiles using MOST (blue) and adapted Van Driest (red) with optimal L_s = 0.08 m (Fig. 4.9a), for stable (panel a) and unstable (panel b) cases. The explanation of the observation symbols is given in Fig. 4.5. Above the roughness sublayer, both models converge to the same gradient. The exact height for which this happens depends on L_{Ob}.

of the vegetation, as e.g. eddies may penetrate deeper into a very open canopy than a closed one. Note that this uncertainty is orders of magnitude smaller compared to the uncertainty in choosing a value for z_{0h}.

In Fig. 4.7 we compared the predicted surface temperatures by MOST and the adapted Van Driest model to the observed temperature (DTS harp) at the top of the vegetation, at 0.10 m for the full measurement period. The adapted Van Driest equation outperformed the traditional MOST approach with a mean absolute error (MAE) of 0.6 K compared to 2.1 K, respectively. The strongest improvement was seen around noon, when the air is well-mixed, and MOST overestimates the gradient at the surface.

The performance of the adapted Van Driest model compared to MOST depended on the height (i.e. 0.1 m) that is used to determine the "true" surface temperature. Choosing a reference height within the vegetation (e.g. at $d + z_{0h} = 0.067$ m), resulted in a higher MAE (0.82 K) for the adapted Van Driest model. Yet it still outperformed MOST (MAE = 2.0 K) since the behaviour above (and within!) the vegetation is better captured by a linear than a logarithmic profile description (see e.g. Fig. 4.6).

4.3.3. PREDICTING TEMPERATURE PROFILES

To assess the model's performance in predicting temperature profiles in the RSL, we compared it against 1350 observed temperature profiles under various atmospheric stabilities. Six composites were created by averaging multiple cases to reduce the effect of outliers. Classes of composites were defined based on the Obukov length. Each class contained the same number of profiles (225) (Fig. 4.8).

Here we used a "bottom-up" approach to predict the normalised temperature profiles. From a *known* surface temperature and corresponding height, we predicted the temperature profiles up to 8.5 m. This means that we prescribed the surface temperature at $d + z_{0h}$ for MOST and at the top of the grass (i.e. 10 cm) for the adapted Van Driest model.

To obtain temperature profiles using the MOST approach, an estimation of z_{0h} was required. Generally, realistic values of z_{0h} are in the order of $0.1 z_{0m}$ (Beljaars & Holtslag, 1991; Garratt & Hicks, 1973; Garratt & Francey, 1978; Brutsaert, 1982). We found an average z_{0m} of 0.01 m for the Veenkampen site, by applying the MOST equations for momentum to a year of wind measurements at 2 m and 10 m. Values show a seasonal dependence varying between 0.006 m (November) and 0.04 m (July). This is in correspondence with typical values for short grass reported in the literature (Wieringa, 1993).

Figure 4.8b gives the profile description using the literature value of $0.1 \times z_{0m}$. The MOST model clearly failed to describe the temperature profiles using this value of z_{0h}. The incorrect estimate of the surface temperature height offsets the temperature profiles by $\hat{\theta} \sim 5 - 15$, which for e.g. $\theta_* = 0.1$ K translates into $\sim 0.5 - 1.5$ K. Taking a larger z_{0h} of 0.01 m (i.e. $z_{0h} = z_{0m}$), improved the fit but still resulted in an offset of 0.5 - 1 K (Fig. 4.8c).

The optimal z_{0h} value that minimised MAE for the surface temperature prediction based on the locally observed 1.5 m temperature was approximately 0.1 m (Fig. 4.9d). However, this implies that z_{0h} equals $10 \times z_{0m}$ implying heat transport to be more efficient than momentum transport, which is physically unrealistic. Using $z_{0h} = 0.1$ m in the model gave a good match for values of $\hat{z}$ above ~ 2, i.e 0.2 m, roughly the RSL height (Fig. 4.8c). For lower values of $\hat{z}$, in the RSL, the observed temperature profiles deviated from

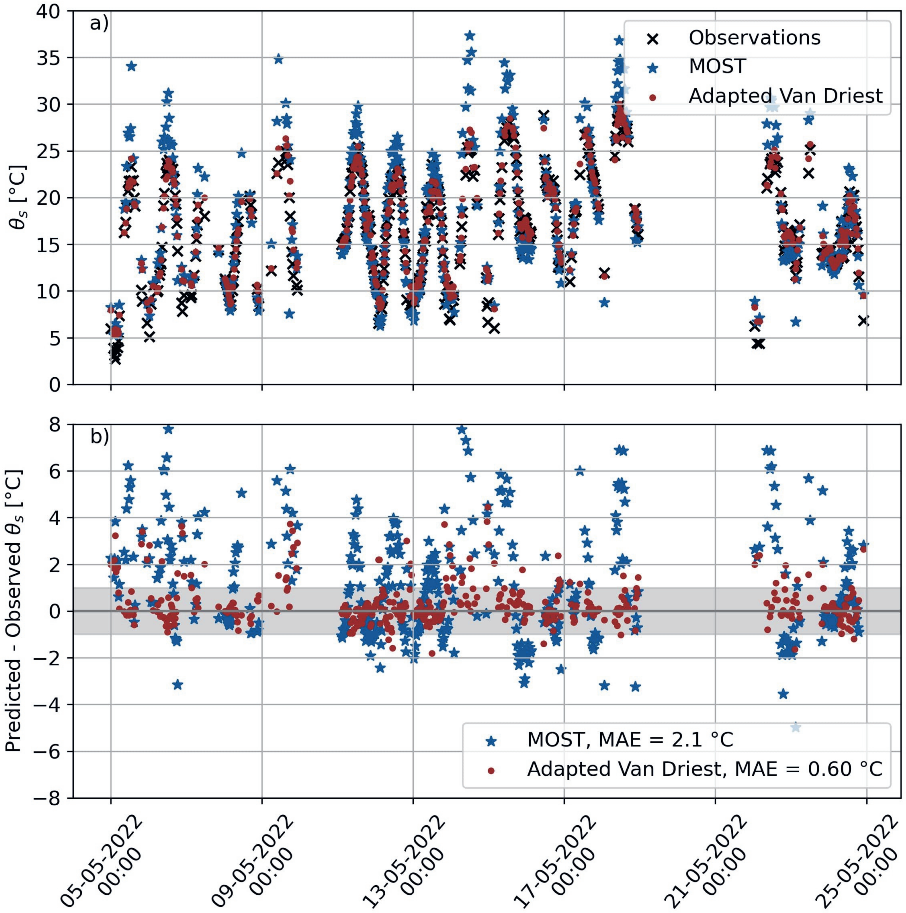

Figure 4.7: Plot of predicted surface temperature over the 10 cm plot, panel a) shows the potential temperature at 10 cm, panel b) shows the mean absolute error between predicted and observed (DTS harp) temperature. The grey shaded bar shows the measurement uncertainty of the DTS harp (+/- 1 K).

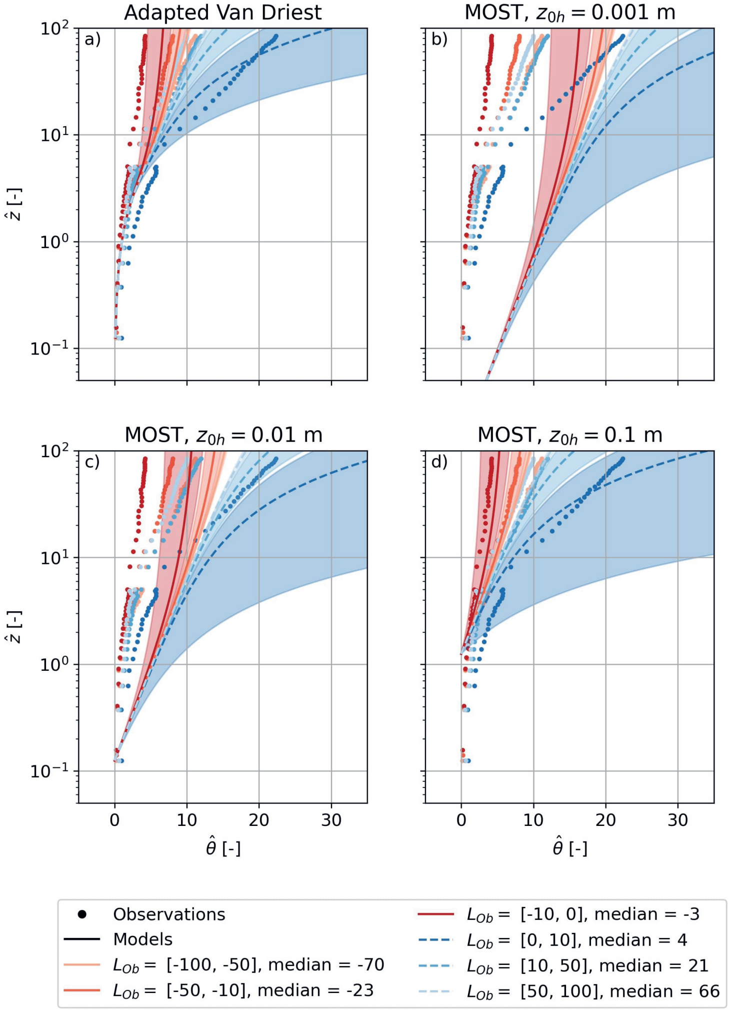

Figure 4.8: Profiles of normalised temperature versus height for stability classes (defined as L_{Ob} ranges), for the adapted Van Driest (panel a) and MOST based on different z_{0h} (panel b, c and d) predictions. Dots represent DTS observations at 2 and 30 cm resolution for the lower 0.64 m and between 0.41 - 8.7 m respectively (as described in Sect. 4.2.1). Length scale L_s was set to its optimal value of 0.08 m (Fig. 4.9a). The full (unstable atmospheric conditions) and dashed (stable atmospheric conditions) lines show the median modelled values per class, and shaded areas show the predicted spread between the maximum and minimum L_{Ob} per class.

the profile predicted by MOST and were linear instead of logarithmic. Since the lower boundary of MOST is $d + z_{0h}$ (17 cm in this case, $\hat{z} = 1.7$), there is no description for the temperature profiles below this height.

For the adapted Van Driest model, we similarly derived the optimal value for L_s by optimizing MAE. This gave $L_s = 0.08$ m for the 10 cm grass and $L_s = 0.16$ m for the 20 cm grass (Fig. 4.9a). L_s thus seems to scale with the canopy height as $\sim 0.8h$. The sensitivity of the MAE to the exact value of L_s was much lower than the sensitivity to z_{0h} (Fig. 4.9b), showing that the adapted Van Driest approach is a more robust alternative to z_{0h}.

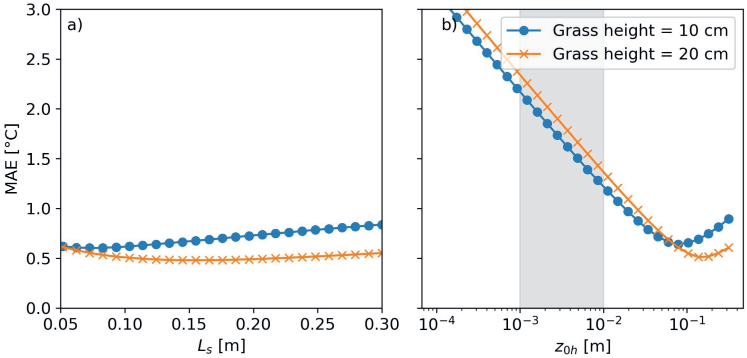

Figure 4.9: Mean absolute error of the surface temperature (at 10 and 20 cm respectively) prediction against possible length scales L_s (panel a) and a range of z_{0h} values (panel b) over the 10 cm and 20 cm grass. The grey band in panel b) indicates the physically realistic range of z_{0h} values. The optimal values that minimise MAE for the surface temperature fall outside of this range.

The adapted Van Driest model correctly captured the transition to a near-linear temperature profile in the RSL ($\hat{z}$ <3), closely following the observations (Fig. 4.8a). For large $\hat{z}$ ($\hat{z} > 5$) it predicted similar temperature profiles as compared to the optimised MOST model. Parameter β (Eq. 4.2, $A = 1 - \exp(-\beta z)$) was empirically determined by minimising the MAE. For smooth flow, an empirical value of 1/26 is found in the literature (Van Driest, 1956). Here, the flow is aerodynamically rough and we found an optimised value of about 1/5.

The values predicted by the adapted Van Driest model deviated by up to 1.5 (~ 0.15 K for $\theta_* = 0.1$ K) from the observations, which can partly be attributed to the measurement uncertainty of the DTS set-up (+/- 1 K). In cases of extreme stability (L_{Ob} = [0, 10]), the largest deviations occurred. These can be explained by the difficulty of obtaining representative temperature measurements under very low wind conditions. Due to the lack of wind, conduction and radiation dominated over convection in the energy exchange between the cable and the air (Sigmund et al., 2017). The temperature of the cable was therefore not representative of the temperature of the air. Additionally, another explanation may lie in the stability correction itself, which is insufficient to correctly capture the typical challenges that come with extremely stable conditions (e.g. intermittent turbulence (Holtslag et al., 2013), submesoscale circulations (Mahrt, 2009) and radiative divergence (Edwards, 2009). Deviations of the models from the observations during unstable conditions, can partly be attributed to the warming of the cable due to solar radiation (Fig. 4.4), but may also lie in the empirical nature of the Dyer stability corrections (Högström, 1996). Moreover, during very unstable (free convection) conditions, θ_* is not a proper scaling parameter. Using θ_* for scaling is based on the assumption that $\overline{w'\theta'}$ and u_* are linked, which is only the case for shear-driven turbulence.

4.3.4. DETERMINING SURFACE LENGTH SCALE L_s

The surface length scale L_s can be approximated through optimisation against observations, as described in Sect. 4.3.3. We hypothesised that L_s is associated with the smallest eddies just in and above the vegetation. This implies that it is independent of the flow characteristics, but mostly depends on the dimensions of the vegetation. So, ideally, L_s should be a measurable quantity related to the vegetation height.

By studying the limit behaviour of the adapted Van Driest model (Eq. 4.6), we found that L_s equals the ratio of θ_* over $(\partial\theta/\partial z)_{z=h}$. Using the high-resolution DTS observations, this ratio could be measured. Therefore we explored whether $\theta_*/(\partial\theta/\partial z)_{z=h}$ increased with vegetation height. The distribution of $\theta_*/(\partial\theta/\partial z)_{z=h}$ for two grass heights is shown in Fig. 4.10. Panels a and c depict the 20 cm grass section of the harp, and panels b and d show the 10 cm section, for dominant wind directions west and east respectively. For wind from the east, air flows over the 3 cm grass, and for the west over the undisturbed plot.

The variation between the two plots was larger than the variation associated with the wind direction. From this, we inferred that $\theta_*/(\partial\theta/\partial z)_{z=h}$ can be reasonably approximated as a fixed length scale equal to $\sim 0.2-0.4h$. Accounting for the standard deviation, the typical range is similar to L_s/h derived for momentum fluxes in tall canopies, i.e. $\sim 0.3-0.6h$ (De Ridder, 2010).

Despite being 2 – 4 times smaller than the optimal values for L_s of $0.8h$ we found before (Fig. 4.9a), a length scale 2 – 4 times smaller only slightly increases the MAE by 0.05 – 0.12 K. Hence, $\theta_*/(\partial\theta/\partial z)_{z=h}$ is a reasonable estimate of L_s. The difference between the expected and optimal L_s might be, because L_s depends on the density of the grass (i.e. the distance between the tussocks) rather than its height (Fig. 4.1a). Note that, similar canopy concepts have been introduced for sparse canopies such as bushes (Raupach, 1992; Jacobs & Verhoef, 1997; Verhoef, McNaughton, & Jacobs, 1997). Further research into the grass structure is needed to support this claim. For now, we introduce as a rule of thumb that $L_s \sim 0.5h$.

4.3.5. RELATION TO TALL CANOPIES

The failure of similarity laws above tall canopies has long been recognised (e.g. Högström et al., 1989; LeMone et al., 2019). Often the standard boundary-layer flux-gradient relationships are adjusted for the RSL over tall canopies via the introduction of a correction term $\phi(z/\delta)$, e.g. Harman and Finnigan (2007, 2008), De Ridder (2010), Verhoef, McNaughton, and Jacobs (1997), Cellier and Brunet (1992), and Graefe (2004). The correction terms introduce a length scale δ that relates to the canopy height, similar to our adapted Van Driest approach. However, the smallest canopies that were studied, were at least an order of magnitude taller than grass (Brunet, 2020).

Raupach et al. (1996) hypothesised that tall canopy flows are more similar to a plane

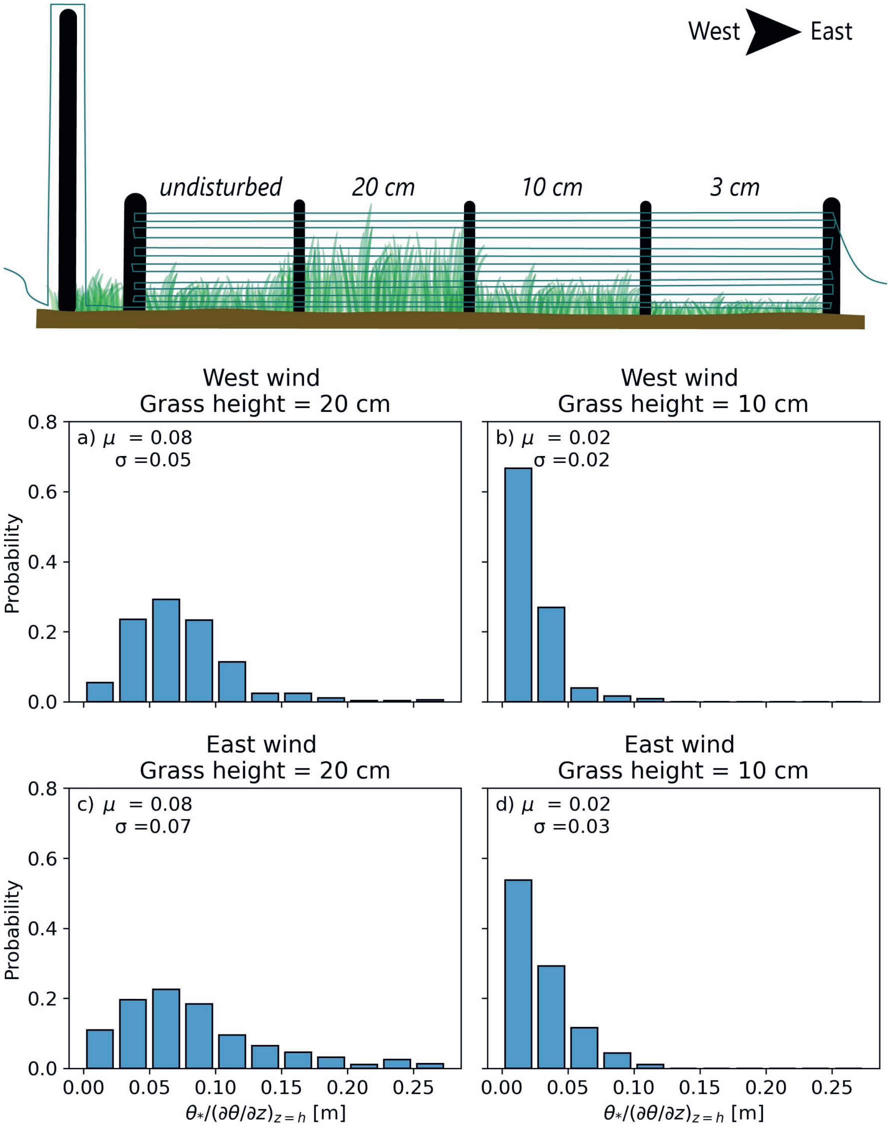

Figure 4.10: Histogram of $\theta_* / (\partial\theta/\partial z)_{z=h}$ (an estimate of L_s) over the 20 cm and 10 cm plot for different wind directions for length scales in the 5th to 95th percentile range.

mixing layer than a boundary layer. A plane mixing layer is formed at the boundary of two atmospheric layers with different wind speeds, in contrast to a boundary layer at a fixed surface. Such a plane mixing layer occurs at the top of a canopy, where the logarithmic profile above the canopy continues into a more or less exponential profile in the canopy. The mixing layer depth is quantified by the vorticity thickness:

$$\delta = U(h) / \left(\frac{\partial U}{\partial z} \right)_{max} \tag{4.10}$$

where h is canopy height, U is mean velocity and $(\partial U/\partial z)_{max}$ is the maximum of the vertical wind velocity gradient and often (but not always) found at the top of the canopy. The dominant turbulent eddies are about the size of the mixing layer depth. This is because in large canopies, the eddies scale with the canopy height, instead of the individual plant elements (i.e., leaves, twigs, branches, etc.). It is reasonable to assume that the flow over short vegetation also behaves as a plane mixing layer. Preliminary DNS studies by our group indeed pointed towards the occurrence of vortex shedding and shear instabilities over (flexible) grass (Sauerbier, 2024). By studying the behaviour of the adapted Van Driest equation near the surface (Eq. 4.7), we found that the formulation of the new length scale L_s closely resembles that of the vorticity thickness used for tall canopies.

Here we compared a relatively simple RSL correction (De Ridder, 2010) and a complex (Harman & Finnigan, 2008) correction to our adapted van Driest model. By scaling the tall canopy models with their respective length scales, we could compare them to the adapted Van Driest model, and we show how they describe similar behaviour near the surface. De Ridder (2010) uses the RSL height as a scaling length scale, while Harman and Finnigan (2008) uses δ. The normalisation procedure is detailed in Appendix A.2.1. Figure 4.11 shows that overall behaviour is very similar (though the second derivatives differ near the surface). This implies that –in a scaled sense– the boundary layer flow does not behave very differently when the height of the roughness elements changes between grass and e.g. forests. Just like the inertial sublayer scaling (log-law) is rather universal, the buffer layer (RSL) could be as well. Why should grass essentially behave differently from e.g. mais etc.?

For completeness, we note that explicit (physical) matching of the log-layer to the RSL has also been proposed over snow by Brutsaert (1975) and Andreas (1987). Snow is often rough, but typically smoother than grass. They hypothesised that heat exchange near the surface happens through diffusion while the eddies are temporarily trapped by the roughness elements (Grass, 1971). The diffusion by one eddy has to be integrated over time to find the average RSL temperature profile. This integration introduced a new length scale that is the ratio of $T_b - T_s$ over the surface gradient (where T_b is the bulk temperature, above the RSL). Their models described separate formulations for the RSL and log layer (that cross at a z_{0h}-dependent height), instead of describing a smooth transition like we do here.

4.4. CONCLUSION AND OUTLOOK

In this study, we introduced a new approach to predict temperature profiles for the roughness surface layer over short vegetation (grassland). It is well-known that MOST

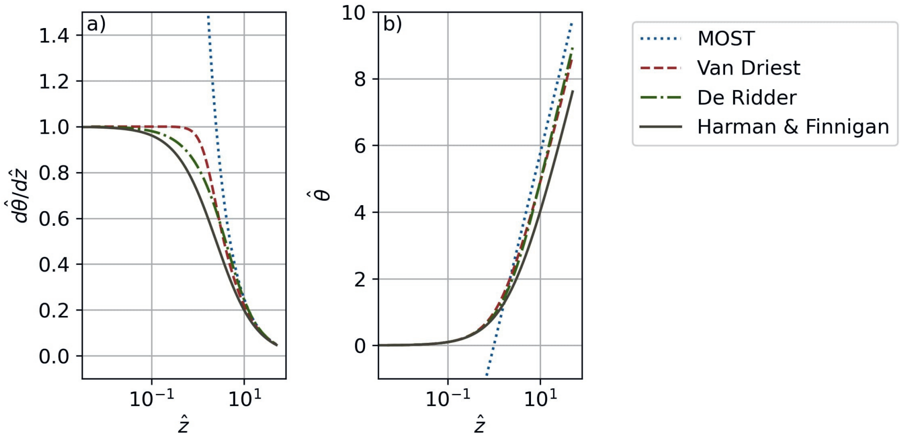

Figure 4.11: Normalised Monin–Obukov (blue), Van Driest (red), De Ridder (2010) (green) and Harman and Finnigan (2007, 2008) (grey) model for the temperature gradient with height (panel a) and numerically integrated temperature profile (panel b). Note the difference between MOST and the other models for small values of $\hat{z}$.

does not hold in the RSL, yet the logarithmic behaviour is conventionally extrapolated down to the surface.

Based on high-resolution temperature observations, we showed that MOST failed to accurately describe the temperature profiles in the lowest 1 – 2 m. Instead of logarithmic behaviour near the surface, we observed near-linear temperature profiles. Inspired by the Van Driest equation that describes the log–linear transition from turbulent to viscous flow over a smooth surface, we developed a similar model for flow over a rough vegetation surface. We therefore adapted the Van Driest model, by replacing the viscous length scale with a surface length scale L_S. We showed that over a rough surface, the geometry of the vegetation determines the size of the smallest eddies near the surface. The adapted Van Driest model outperformed the roughness length concept in describing the temperature profiles near the surface and predicting the surface temperature.

The adapted Van Driest equation described a similar shape as the De Ridder (2010) and Harman and Finnigan (2007, 2008) model for tall canopies. This showed the potential for upscaling. Moreover, we found that the surface length scale can be linked to the height of the vegetation. Future research is needed to prove the general applicability of the adapted Van Driest equation over different types of surface cover.

5

DIAGNOSING LE

What is a scientist after all? It is a curious man looking through a keyhole, the keyhole of nature, trying to know what's going on.

Jacques Yves Cousteau

This chapter is based on:
Boekee, J., Van de Wiel, B. J., & ten Veldhuis, M. C.. Diagnosing LE: when Penman-Monteith and eddy-covariance disagree. Quarterly Journal of the Royal Meteorological Society, ***In preparation***.

Summary

Despite its omnipresence in atmospheric models, the Penman-Monteith (PM) equation often fails to accurately represent the latent heat flux (evapotranspiration).

In this study, we critically compared the latent heat flux calculated following the PM model to eddy-covariance (EC) measurements over a grass and forest site in the Netherlands. By analysing deviations between the model and observations, we identified when and under which conditions the largest discrepancies occur.

We demonstrate how these discrepancies are particularly pronounced when the vegetation is decoupled from the air above. Low wind speeds and high incoming radiation warm the vegetation, but limit water transport from the stomata to the air above the canopy. Under these conditions, thick leaf boundary layers may form. Moreover, the closed canopy structure may block flow and decouple it from the air above the vegetation layer. Such decouplings are not included in aerodynamic and stomatal resistance formulations, and PM therefore tends to predict higher latent heat fluxes than sampled by EC instruments.

The discrepancies are more pronounced over short vegetation such as grass, than over taller canopies, as higher surface roughness will enhance mixing, limiting the decoupling. Over tall canopies, discrepancies are mainly caused by an underestimation of the flux resistance, likely because only the top layers of the canopy receive enough radiation to actively contribute to transpiration. We recommend steering observation efforts towards in-canopy sampling of radiation, temperature and humidity, to improve resistance parameterisations for evapotranspiration models.

5.1. INTRODUCTION

Land surface models (LSMs) play a critical role in numerical weather prediction, climate simulations, and high-resolution atmospheric modelling, such as large eddy simulations. They provide the interface between the surface and the lowest atmospheric model layer. However, systematic biases in their representation of latent heat fluxes have been consistently reported, both in early studies (Henderson-Sellers et al., 1996; Chen et al., 1997) and in more recent model intercomparison efforts (Holtslag et al., 2013; Best et al., 2015).

Simple linear regression models can still outperform complex evapotranspiration models that include multiple soil layers and different vegetation types (Best et al., 2015; Abramowitz et al., 2008). Dirmeyer et al. (2006) points towards a systematic bias in the near-surface temperature and humidity, which may explain the failure of models to reproduce the energy fluxes. Renner et al. (2021) highlighted that LSMs especially struggle to capture the diurnal cycle of latent heat flux accurately, while Wang et al. (2011) argue that errors result from a misrepresentation of seasonal biological processes. These contrasting findings suggest that key processes and governing variables that influence latent heat fluxes are not adequately represented in current LSMs.

The Penman-Monteith (1965) model (PM) is one of the most widely used models to estimate latent heat fluxes and underlies many LSMs (e.g. Mitchell, 2005; Clark et al., 2010; Zhang et al., 2022; ECMWF, 2024). It distinguishes itself by its physics-based approach and use of a limited number of commonly available meteorological variables.

In this study, we diagnose the sources of deviation between latent heat flux calculated by the Penman-Monteith equations, compared to evapotranspiration observed using eddy-covariance techniques. We identify meteorological conditions underlying the largest deviations and to what extent they coincide with violations of the assumptions inherent in Penman-Monteith. Instead of comparing many models, sites and climates, we take a deep dive into two locations to look beyond the general performance. This investigation allows us to pinpoint the critical limitations of the PM method and determine the aspects that require refinement or revision in future research.

PM departs from the assumption that vertical moisture transport is directly related to the vertical gradient of atmospheric moisture. This is modelled according to a resistance analogy:

$$LE = -\frac{\rho c_p}{\gamma}\frac{\Delta e}{r_a}. \tag{5.1}$$

Here, ρ is the dry air density (kg/m^3), c_p the specific heat capacity ($Jkg^{-1}K^{-1}$), γ is the psychrometric constant ($\gamma \approx 66$ Pa K^{-1}), Δe the vapour pressure difference between the atmosphere and the surface, and r_a (s/m) the aerodynamic resistance derived from Monin-Obukov Similarity Theory (MOST):

$$r_a = \frac{1}{\kappa u_*}\left(\ln(z/z_0) - \Psi(z/L) + \Psi(z_0/L)\right) \tag{5.2}$$

in which u_* is the friction velocity, κ the von Kàrman constant (≈ 0.4) and z the height above the surface minus the displacement height d. z_0 is the roughness height for momentum and L is the Obukov length. The Ψ functions are the integrated form of the similarity functions (Dyer, 1974).

The integrated form of Equation 5.1 describes a logarithmic moisture profile. However, over a natural, vegetated surface, the flow near the surface (in the atmospheric roughness layer) deviates from the logarithmic description. Here, the airflow is disturbed by individual roughness obstacles, which disrupts the profiles from their logarithmic shape. Special roughness sublayer formulations have been introduced for short (Boekee et al., 2024) and tall vegetation (Harman & Finnigan, 2008; De Ridder, 2010), that correct the profiles to a more linear shape. Not taking these corrections into account may result in biases in the predicted latent heat flux.

To eliminate the need for measurements at two heights, Penman (1948) assumed that the air at the surface is saturated. This way, the surface vapour pressure can be expressed as a function of the surface temperature T_s. This would still require a temperature measurement at the surface. This is circumvented through energy balance closure (i.e. $R_n - G = H + LE$). Additionally, to arrive at an explicit formulation for the latent heat flux, a linearization of the vapour pressure curve is applied. The linearization is given by: $e_{sat}(T_s) = e_{sat}(T_a) + s(T_a)(T_s - T_a)$. This gives a new version of Equation 5.1:

$$LE = -\frac{\rho c_p}{\gamma}\frac{e_a - e_{sat}(T_s)}{r_a} = -\frac{\rho c_p}{\gamma}\left[\frac{e_a - e_{sat}(T_a)}{r_a} + s(T_a)\frac{(T_s - T_a)}{r_a}\right] \tag{5.3}$$

With $\frac{(T_s - T_a)}{r_a} = \frac{H}{\rho c_p} = \frac{R_n - G - LE}{\rho c_p}$ we come to the final version of Penman's equation:

$$LE = \frac{s(R_n - G)}{s + \gamma} + \frac{\rho c_p (e_{sat}(T_a) - e_a)}{r_a(s + \gamma)} \tag{5.4}$$

in which s is the rate of change of saturation vapour pressure with air temperature, R_n net incoming radiation and G the ground heat flux.

Penman's equation was developed for evaporation over open water, which justifies the assumption of 100% saturated air at the surface. When water is readily available at the surface (e.g. over open or intercepted water), the evaporative flux is indeed limited by the atmospheric moisture demand (Brutsaert, 1982). In contrast, water transpiring from stomata is subject to a stomatal resistance and leaf boundary layer resistance. The stomatal control was introduced in the Penman equation by Monteith (1965) through a serial surface resistance factor for non-stressed vegetation: stomatal resistance r_c. This resulted in the famous Penman-Monteith equation:

$$LE = \frac{s(R_n - G) + (\rho c_p)/r_a(e_{sat}(T_a) - e_a)}{s + \gamma(1 + r_c/r_a)} \tag{5.5}$$

This implicitly assumes that air inside the stomata is 100% saturated and that the temperature inside the stomata is equal to the air temperature near the leaves. However, in laboratory experiments, relative humidity as low as 70% has been observed inside stomata (Wong et al., 2022). Moreover, plants are heated by solar radiation, which enhances the temperature inside the stomatal cavities. The difference between the leaf temperature and air temperature near the leaves depends on the structure of the leaf boundary layer, which in turn depends on the wind speed (Raschke, 1960; Schuepp, 1993).

The original PM equation assumed the stomatal resistance is constant in time. In reality, however, the transport resistance from the stomatal cavity to the leaf boundary layer depends on the opening and closing of the stomata. Stomatal opening is influenced by multiple environmental factors including light, CO_2 concentration, plant temperature, soil moisture and air humidity. To date, most LSMs have implemented empirical, climate-driven r_c models (e.g. Jarvis, 1976; Monteith, 1965). However, these approaches do not capture *interactions* between environmental drivers, and are due to their empirical nature unsuitable for extrapolation under changing climate conditions. As a result, there is a shift towards photosynthesis-based models, which incorporate plant optimisation strategies for balancing CO_2 uptake and water loss (e.g. Goudriaan, 1977; Farquhar & Wong, 1984; Ball et al., 1987).

By studying about a decade of data from a grassland and forest site in the Netherlands, we will evaluate the performance of the Penman-Monteith equation with three different ways of representing stomatal control. First, we will discuss model average, and diurnal and seasonal model performance to identify conditions of large model biases. Then, we will discuss how these biases result from the assumptions underlying Penman's equation, to identify areas of improvement.

In Sect. 5.2, we describe the field observations and stomatal control models. In Sect. 5.3, the model performance will be discussed in depth, while Sect. 5.4 discusses the influence of possible measurement errors and validity of the assumptions underlying PM. Finally, Sect. 5.5 summarises the conclusions and provides recommendations on how to improve model performance.

5.2. METHODS

5.2.1. OBSERVATIONS

The observations used in this study are part of the Ruisdael Observatory network for monitoring greenhouse gases across the Netherlands. We use observations above a pine forest from the Loobos Flux tower (van der Molen et al., 2024), and above a grassland site at the Veenkampen automated weather station (Heusinkveld et al., 2024). All data is openly available via: https://maq-observations.nl/data-downloads/.

LOOBOS

The Loobos flux tower is located at the Veluwe region (52.09 °N and 5.44 °E), at a patch of Scottish Pine trees (*Pinus Sylvestris*) planted in the 1910s, with a mean height of about 22 m. The tower itself is 38.1 m high, and several instruments are placed on, along and around the tower. We use observations from 2022-2024.

The latent heat flux is measured by an eddy-covariance system (EC) placed on top of the tower (Gill HS-50 sonic anemometer / LI-7500 gas analyser, LI-COR Biosciences, USA), logging at 20 Hz, and aggregating in 30-minute intervals. Additionally, we use radiation (Kipp & Zonen CNR4), air temperature and relative humidity (Vaisala HMP155A) and wind speed (Gill Windsonic) measurements from the top of the tower (i.e. ~ 16 m above the canopy top). The ground heat flux is measured at 5 cm depth (Hukseflux HFP01SC) at 2 locations and we use the average.

VEENKAMPEN

The Veenkampen automated weather station is located in the Binnenveld nature area (51.98 °N, 5.62 °E), between unmaintained fields with grass and reeds. The patch itself was sown with ryegrass in 2011 and kept at approximately 10 cm. The weather station provides

10-minute averages of several meteorological variables. We use observations from 2015-2024. We use 30-minute aggregated eddy-covariance measurements (Campbell CSAT3 sonic anemometer / LI-COR Li-7500 gas analyser) and radiation (Kipp & Zonen SGR3 and CR11) measured at 1.5 m height. The ground heat flux is measured at 6 cm depth (Hukseflux HFP01SC) at 3 locations and we use the average. For T_a in Equation 5.5 we use the shielded, ventilated air temperature observations and for e_a the relative humidity both measured at 2 m (HMT337). The wind speed is measured with a Windsonic 75 at 2 m.

DATA FILTERING

Data for the Loobos and Veenkampen have gone through rigorous data quality control. Additionally, we applied a data filter for conditions when the leaves are wet. When the leaves are wet, r_c reduces to zero. Water does not have to be transported through the stomata. Penman-Monteith with a constant r_c therefore underestimates the flux size compared to the EC in these cases. However, when the leaves are wet, it is likely that the EC is too, and the flux observations become unreliable. At Loobos leaf wetness sensors are installed at different heights, we remove the datestamps when the sensors at 2.4 m and 22.1 m indicate that the leaves are wet (i.e. 20% of the data). At Veenkampen no leaf wetness sensors are available, therefore we filter for rainfall. Since these are only the moments it is actually raining, this removes less than 1% of the data. The leaves (and EC) may remain wet afterwards.

5.2.2. STOMATAL RESISTANCE MODELS

The Penman-Monteith model was originally developed to calculate *daily* averages. An r_c was chosen that is representative of the average daily stomatal resistance. In our analyses, we will use the empirical r_c values for short grass and needle leaf forest of respectively 50 and 100 s/m, given by Moene and van Dam (2014).

However, when the Penman-Monteith model is used in models with a higher temporal resolution, the constant r_c can result in an over- or underestimation of the transpiration flux. The stomata directly respond to sub-daily variations in light, temperature, humidity and atmospheric CO_2.

Various modelling approaches exist to represent this (Damour et al., 2010): (1) empirical models driven by solely climatic conditions (e.g. Jarvis, 1976; Stewart, 1988; Monteith, 1965), 2) models based on the relationship between photosynthesis and stomatal control (e.g. Goudriaan, 1977; Farquhar & Wong, 1984; Ball et al., 1987), 3) hydraulic models that account for water transport through the xylem (e.g. Jones & Sutherland, 1991) and 4) models that explicitly simulate the water balance of stomatal guard cells (e.g. Gutschick & Simonneau, 2002; Buckley et al., 2003).

Following the implementation of stomatal models in LSMs, we will discuss the empirical Jarvis-Stewart model and the photosynthesis-based A-gs model. Both model responses are illustrated in Figure 5.1 and will be discussed next.

JARVIS-STEWART

The Jarvis-Stewart approach (JS) multiplies a minimal stomatal resistance of a leaf (i.e. $r_{s,min}$, the stomatal resistance under optimal conditions) with empirical response functions with values equal or larger than 1. By dividing the stomatal resistance by the LAI,

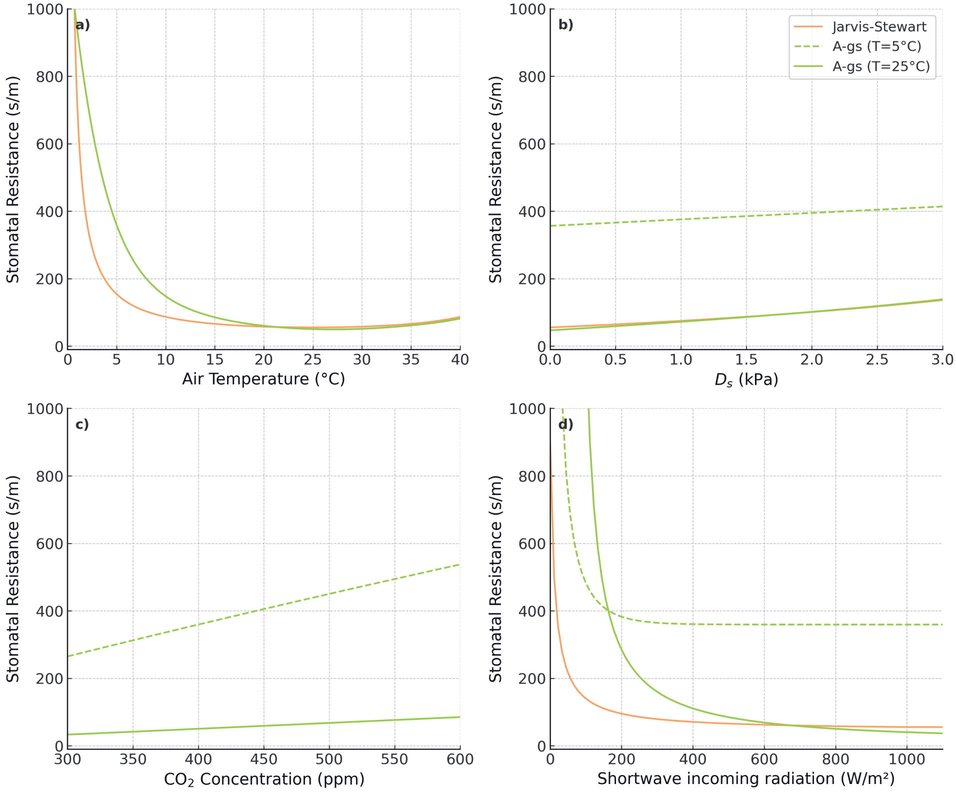

Figure 5.1: Stomatal resistance as a function of environmental variables. Jarvis-Stewart does not include a correction for CO_2, and is therefore not plotted in panel c. The shape of the A-gs functions depends on the other environmental variables. When not varied these reference conditions are therefore: T_{air} = 5 (dotted line) or 25 (full line) °C, CO_2 = 400 ppm , D_s = 1.5 kPa, $r_a = 50\ s/m$, and global radiation = 400 W/m^2. For low radiation conditions, the A-gs model may return (non-physical) 'negative' resistances.

the resistance scales from a square meter of leaf to a square meter of canopy. For grass we use a LAI of 1 (Byrne et al., 2005), and for needleleaf forest 4.5 (Cisneros Vaca et al., 2018).

$$r_c = \frac{r_{s,min}}{\text{LAI}} f_1(\text{SW}_{in}) f_2(D_s) f_3(T_a) \tag{5.6}$$

Here, we use the response functions as given by Jarvis (1976) and Noilhan and Planton (1989):

$$f_1^{-1} = \min\left[1, \frac{0.004\ \text{SW}_{in} + 0.05}{0.81(0.004\ \text{SW}_{in} + 1)}\right] \tag{5.7}$$

$$f_2^{-1} = \exp(-g_D \cdot D_s) \tag{5.8}$$

$$f_3^{-1} = \begin{cases} 1 - 0.0016(T_{\text{ref}} - T_a)^2 & \text{for } T_a - 25\,\text{K} < T_{\text{ref}} < T_a + 25\,\text{K} \\ \to 0 & \text{otherwise} \end{cases} \tag{5.9}$$

in which SW_{in} is the incoming shortwave radiation above the canopy and D_s the vapour pressure deficit in hPa (i.e. the difference between the saturated vapour pressure at temperature T_a ($e_{sat}(T_a)$) and the actual vapour pressure e_a. g_D is a plant species dependent constant with value 0 or 0.03 hPa^{-1} for grass or forest, respectively. T_{ref} is a reference temperature of 25 °C. The complete Jarvis-Stewart formulation also includes a correction for soil moisture. We do not include the correction in our analyses, as for our locations in the Netherlands, the soil moisture is rarely below the wilting point: in < 1% of the cases.

Note here that the form of Equation 5.6 highlights one of its main deficiencies: it does not account for interactions between environmental variables, e.g. low incoming radiation often correlates with low air temperatures. This may result in double corrections and overestimations of the canopy resistance.

A-GS

The A-gs model is based on the stomatal behaviour of striking a balance between optimal CO_2 uptake and minimal water loss. Many models exist for this link between stomatal resistance and photosynthesis and some have been introduced in meteorological models to study the interactions between the stomata and the direct surroundings of the leaf. For example, Collatz et al. (1991) introduced the photosynthesis model by Ball et al. (1987). Ronda et al. (2001) (based on (Jacobs, 1994; Jacobs et al., 1996)) calculates net assimilation (i.e. CO_2 flux into the cell) according to Goudriaan (1977). Here we follow the Goudriaan (1977) approach as described by ECMWF (2024).

The stomatal resistance is calculated in three steps, for which the details are given in Appendix A.3.2. First, the net assimilation flux (A_n) is calculated as a fraction of the gross assimilation. The gross assimilation depends on the photosynthetically active radiation (PAR), and the environmental CO_2 concentration (C_e). These exact relationships are plant-specific and temperature-dependent. Second, the internal CO_2 concentration (C_i) is defined as a fraction of C_e. This ratio depends on D_s. Last, once the A_n and C_i are known, the stomatal resistance for CO_2 ($r_{s,c}$) can be derived via a resistance law:

$$r_{s,c} + r_a = (C_e - C_i)/A_n \tag{5.10}$$

Table 5.1: Performance of the Penman-Monteith model compared to EC observations, for a constant stomatal resistance value and two dynamic stomatal resistance models. For r_c we give the median, and the 25^{th} and 75^{th} percentile.

Location	**Model**	**r_c (s/m)**	**MBE (W/m^2)**	**MAE (W/m^2)**	**MAE$_b$ (W/m²)**	**MAE$_p$ (W/m^2)**	**MAE$_u$ (W/m^2)**
Veenkampen	constant r_c	50	20	34	9.0 (26.3%)	5.0 (14.5%)	20.0 (59.2%)
	Jarvis-Stewart	352.0 (114 - 1709)	-14	30	7.0 (24.6%)	5.0 (15.0%)	18.0 (60.4%)
	A-gs	157.8 (-9824 - 11456)	-12	38	9.0 (22.9%)	0.0 (0.4%)	29.0 (76.7%)
Loobos	constant r_c	100	37	44	20.0 (45.0%)	2.0 (4.6%)	22.0 (50.3%)
	Jarvis-Stewart	223.8 (78 - 1447)	26	34	10.0 (30.2%)	4.0 (10.6%)	20.0 (59.1%)
	A-gs	40.9 (-2202 - 1777)	90	103	30.0 (29.5%)	29.0 (28.3%)	43.0 (42.2%)

The stomatal resistance to water vapour is then defined as $r_s = r_{s,c}/1.6$. To upscale to the canopy level, we divide by the LAI, as with Jarvis-Stewart.

In low radiation conditions, the A-gs model may calculate negative stomatal resistances that are non-physical. Since the stomatal resistance is inversely related to the net assimilation (Equation 5.10), negative r_s values occur when A_n is negative, i.e. a net CO_2 flux out of the leaf. A_n is described as an exponential response to radiation, of the form $A_n = 1 - e^{-(PAR - PAR_{crit})}$ (Appendix A.3.2). Here, PAR_{crit} is a critical radiation level. For $PAR < PAR_{crit}$ the net assimilation becomes negative, in combination with a positive CO_2 gradient this can only be achieved with negative resistance values, which is physically impossible.

5.3. RESULTS

To evaluate the performance of the Penman-Monteith model, we compared modelled latent heat fluxes against eddy-covariance observations above the canopy at 30-minute time resolution. We first assessed the model's average performance using different stomatal conductance formulations and examined the mean diurnal and seasonal cycles. Then, we identified periods of over- and underestimation to better understand which assumptions of the Penman-Monteith model may have been violated under these conditions.

5.3.1. AVERAGE PERFORMANCE

The comparison between observed and modelled latent heat (LE) fluxes, as presented in Figure 5.2, reveals poor agreement between the model and observations. Remarkably, the magnitude of the model errors is comparable for both vegetation types, despite grass being considered relatively simple and well understood compared to forest. The maximum LE predicted by the models is limited by the maximum available energy, which results in asymptotic (capping) behaviour at 500 and 400 W/m^2 for grass and forest respectively. This is a result of the use of the radiation measurements, and will be discussed in depth in Section 5.4. Discerningly, although stomatal resistance models account for dynamic physiological responses, such as stomatal closure under low radiation, high vapour pressure deficit (D_s), or elevated CO_2, these adjustments do not significantly improve model accuracy compared to using a simple constant stomatal resistance (r_c). In fact, all models yield similar r^2 values.

To assess the nature of the model deviations, we analyse the Mean Bias Error (MBE) and a decomposition of the Mean Absolute Error (MAE) (Table 5.1), following Robeson and Willmott (2023). This decomposition separates the MAE into average systematic,

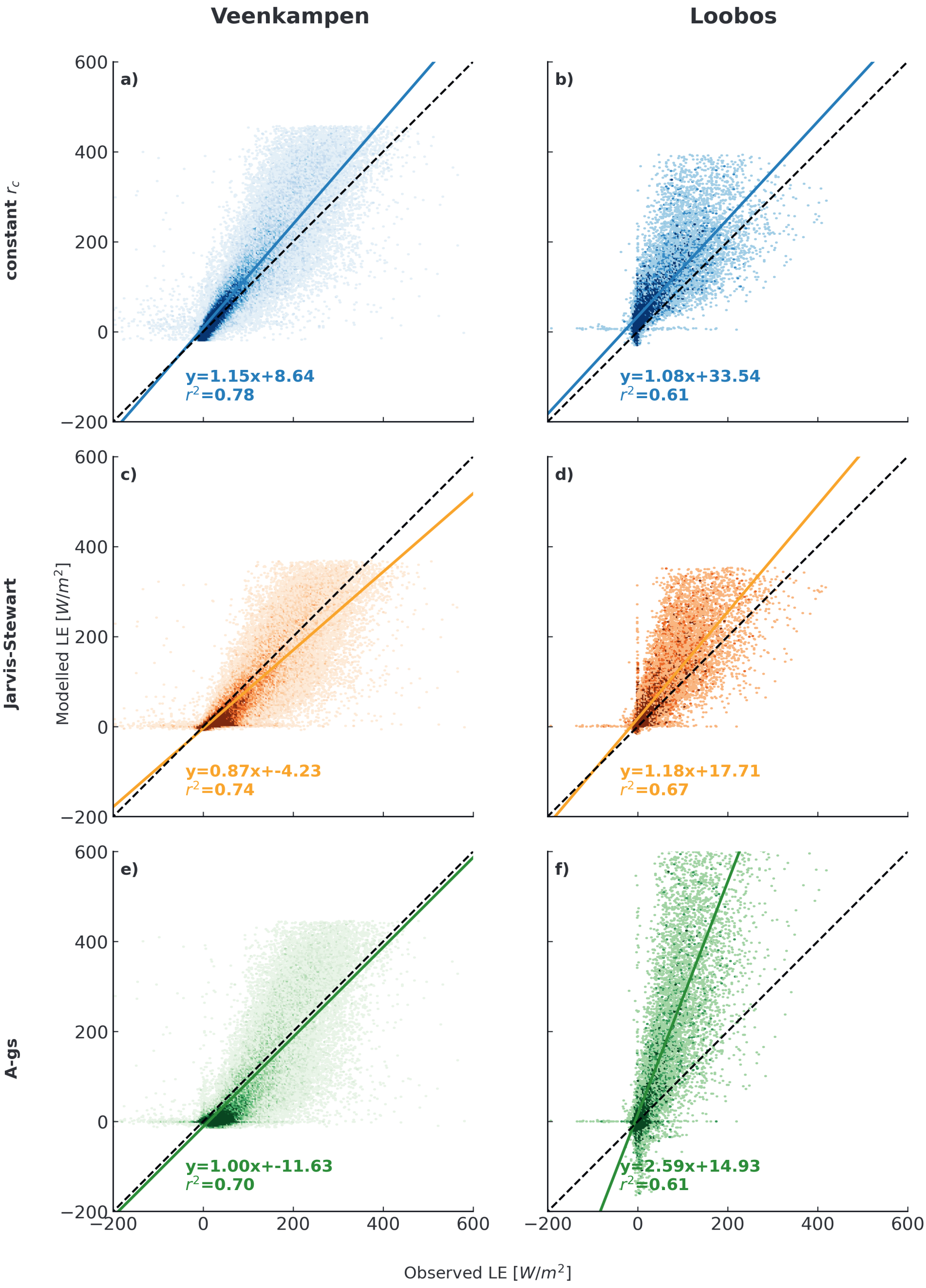

Figure 5.2: Scatter plots of observed versus modelled latent heat fluxes using three stomatal conductance models: panel a-b for constant r_c, panel c-d using Jarvis-Stewart, and panel e-f using A-gs. The coloured dots indicated the *LE* estimates, the coloured full line is a linear fit, and the dotted black line the 1:1 line.

regression systematic, and unsystematic components. Biases in the average reflect a consistent over-/underestimation of the flux, while positive biases in the regression slope are a result of an overestimations of high fluxes, and underestimations of low fluxes.

The Penman-Monteith model with a constant stomatal resistance tends to overestimate the *LE* flux, as shown by a positive MBE of 20 and 37 W/m^2, over grass and forest respectively. For grass, 26% of the MAE in PM is the result of a bias in the average, while 14% of the error results from an error in the regression slope. The remaining 59% is unsystematic (MAE_u). We observe a positive MBE (20 W/m^2) turn into a (smaller) negative MBE when a stomatal conductance model is applied (-14 W/m^2 for JS and -12 W/m^2 for A-gs). This results from the higher median stomatal conductance: 352 and 158 s/m for JS and A-gs, compared to a constant value of 50 s/m. For JS we now tend to slightly overestimate the r_c. However, for A-gs stomatal resistance is more accurately estimated, reducing the regression error to 0.4% and with the remaining 76% of the error being unsystematic.

Over forest, these ratios are different as the regression error for the constant r_c model is very small, only 5%. Here, 45% of the error results from a bias, while the remaining 50% is unsystematic. The positive bias (37 W/m^2) in the modelled *LE* fluxes improves slightly with JS (24 W/m^2), but becomes much higher with A-gs (90 W/m^2). This is mainly caused by scaling of r_c to a canopy resistance using LAI. The large LAI ($\sim$ 4.5, based on the nearby Speulderbos (Cisneros Vaca et al., 2018)) results in small r_c values and large latent heat fluxes for the A-gs-based model. The stomatal resistance is taken as the sum of the parallel resistances of the different leaf layers, which means that more layers result in a lower resistance. However, for dense forest canopies, the shading of the lower leaves limits their contribution (Kelliher et al., 1995) and using LAI may thus give an underestimation of r_c.

The main difference in error between the two vegetation types thus lies in the relatively greater contribution of regression error over grassland compared to forest. These biases in the regression slope suggest that $|e_a - e_s|$ is overestimated or r_c remains underestimated under for high flux conditions, and vice versa for small flux conditions. This could be caused by the model predicting maximum *LE* values, whereas in reality, stomatal closure by plants limits transpiration and water availability. The model performance over grass does indeed improve when taking stomatal closure into account using the A-gs model, but not when using the Jarvis-Stewart model.

In contrast, over forested areas, incorporating a canopy resistance model does not lead to improved model performance, since the error is mainly due to a bias. This indicates a structural modelling error over forest, potentially an overestimation of the available energy. Possible explanations for this could be an underestimating the ground heat flux, or a missing energy sink such as biomass energy storage. This will be discussed in Section 5.4.

5.3.2. SEASONAL AND DAILY CYCLES

As a next step we evaluate the average diurnal and seasonal performance of the Penman-Monteith model including the three different stomatal conductance representations. Through inverse modelling, we derive the r_c that is required in the PM model so as to match the observed *LE* flux, and compare these to the model estimates.

Figure 5.3a and c illustrate the seasonal and diurnal patterns of canopy resistance

(r_c) over grassland, as derived from eddy covariance (EC) observations (black lines). r_c is relatively small and constant (50 – 200 s/m) throughout the day and year, with a subtle increase in summer reflecting stomatal closure. Fitted r_c values are close to the literature-based constant r_c estimate (50 s/m). It turns out to provide a good first-order approximation, though it may not fully capture dynamic stomatal responses under varying environmental conditions. Over forest, however, fitted r_c values are larger and highly dynamic throughout the year (-10 – 600 s/m) and increase with sunrise and sunset more strongly, in response to lower radiation (Fig. 5.3b and d).

The seasonal behaviour of the stomatal conductance models is similar for both sites showing an increase in r_c in winter. Over grass, this means that both models more or less correctly estimate the summer resistance, but do not capture the decrease in winter. Over forest, A-gs captures the variation over the year correctly, but underestimates the values overall throughout the year. JS overestimates the seasonal variation, resulting in an underestimation of r_c in summer and an overestimation in winter.

Both stomatal conductance models produce a pronounced increase in canopy resistance (r_c) during nighttime, driven by the absence of radiation and the resulting stomatal closure. Specifically, JS predicts r_c values that are orders of magnitude higher than those derived from observations, while the A-gs model yields unphysical negative resistances (see Sect. 5.2.2). Despite these discrepancies, their practical impact on modelled fluxes remains limited, as nighttime latent heat fluxes are typically small.

The contrasting behaviour of r_c between grass and forest (i.e. respectively constant r_c versus diurnal and seasonally variable r_c) raises the following question. Is this due to 1) differences in environmental conditions over grass and forest, such that only forest vegetation needs to close its stomata, or 2) inherent differences in plant behaviour? In other words, are trees more "strategic" in their stomatal regulation? Both the JS and A-gs models also show a variable r_c over grass, suggesting similar stomatal closure strategies. The absence of similar variations in the fitted r_c suggests that in reality grass behaves differently than suggested by the models. However, other errors in the Penman model can also propagate into the inverse modelled r_c values. For instance, the lack of increase in r_c in winter could also be the result of an underestimation of the moisture gradient $|e_a - e_{sat}|$ from weather station observations or due to the PM model assumptions, since a lower r_c is then needed to achieve the same flux. We will revisit this question in Section 5.4.

5.3.3. CONDITIONS UNDERLYING LARGE ERRORS

Next, we focus on better understanding the conditions underlying the instances of poor performance of the Penman-Monteith model, including the stomatal parameterisations. In order to analyse the over- and underestimations, we divide the errors into three categories. The error is defined here as the difference between model and observed LE. First, we split the errors into under- and overestimates. Then we define a category of large underestimates as the errors below the 25th percentile of the underestimates. For overestimates we did the same, i.e. errors above the 75th percentile are defined as large. The set of all errors between the 75th percentile of the overestimates and 25th percentile of the underestimates are defined as small deviations. For each of the three categories, we plotted their distribution against several meteorological conditions. The results for

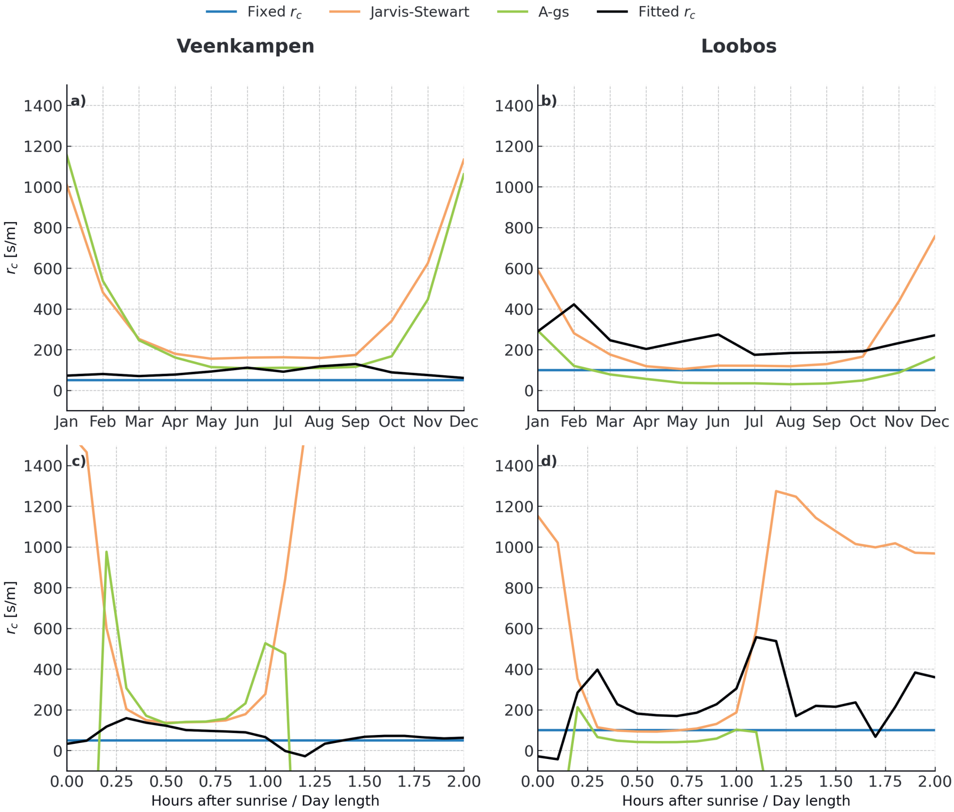

Figure 5.3: Median seasonal (panel a and b) and diurnal (panel c and d) patterns of r_c. No r_c values are given for A-gs during the night, as these approach (negative) infinity. The x-axis of panel c) and d) shows the time after sunrise normalised by hours of sunlight during that day. This way we account for variations in day length over the year.

grass are given in Figure 5.4, the results over forest are in Figure 5.5. We only show the result for constant r_c, the distributions for the stomatal resistance models are qualitatively comparable and given in Appendix A.3.1.

Figure 5.4 and 5.5 a and b show that small deviations of modelled LE flux versus observations are spread relatively consistently throughout the day and year (green lines). However, mainly with low D_s (panel c), low temperature (panel e), low radiation (panel g) and a relatively small difference between plant and air temperature (panel f), as well as relatively low wind speeds (panel d). This corresponds to small LE fluxes. Large underestimations occur throughout the year, when the available energy is around zero.

For grass, larger overestimations coincide with higher D_s, T_{air} and $R_n - G$. Both grass and forest return the largest overestimations for high available energy, high temperatures and dry air. Applying a stomatal conductance model does not substantially correct for this (Appendix A.3.1), suggesting that the underlying cause is not a result or the stomatal behaviour or stomatal behaviour is not correctly captured by the models .

A difference between grass and forest is the temperature difference between vegetation and air. Large overestimations over grass occur in conditions where the vegetation is much warmer than the air near the surface. This also corresponds to a dry top soil. This is not the case for forests, where soil moisture remains low throughout the dataset, but the LE flux is maintained by tree roots accessing deeper soil layers. Additionally, temperature differences between vegetation and air are smaller due to the shading provided by the canopy. These vegetation-air differences will be discussed in Section 5.4.

5.4. DISCUSSION

For the Veenkampen and Loobos site, we have additional measurements available to investigate several of the assumptions in the PM model. This allows us to evaluate to which extent model deviations follow from model assumptions not being met under certain conditions.

ENERGY BALANCE CLOSURE

In Penman's equation, the saturated vapour pressure at the surface depends on the surface temperature (T_s) via the law of Clausius-Clapeyron. The surface temperature is 'replaced' by assuming energy balance closure (see Sect. 5.1). If the observed energy balance does not close, i.e. when $R_n - G > H + LE$ the model will return a higher LE flux than the eddy-covariance. In this section, we will first evaluate the energy balance closure for both sites. Next, we will directly use the surface temperature to predict LE, instead of calculating it from enforced surface energy balance closure. These results are given in Figure 5.6.

Figure 5.6a-b and c-d shows that indeed the eddy-covariance flux observations ($H + LE$) do not add up to the available energy ($R_n - G$) for Veenkampen and Loobos. Especially during midday, the mean $H + LE$ is lower than $R_n - G$. This could explain the afternoon mean positive bias of Penman-Monteith compared to the EC measurement that we observed in Figure 5.4 and Figure 5.5.

An energy imbalance is commonly observed in surface energy balance studies that integrate eddy-covariance measurements alongside radiative and ground heat flux measurements. Such discrepancies often stem from underestimation of turbulent fluxes,

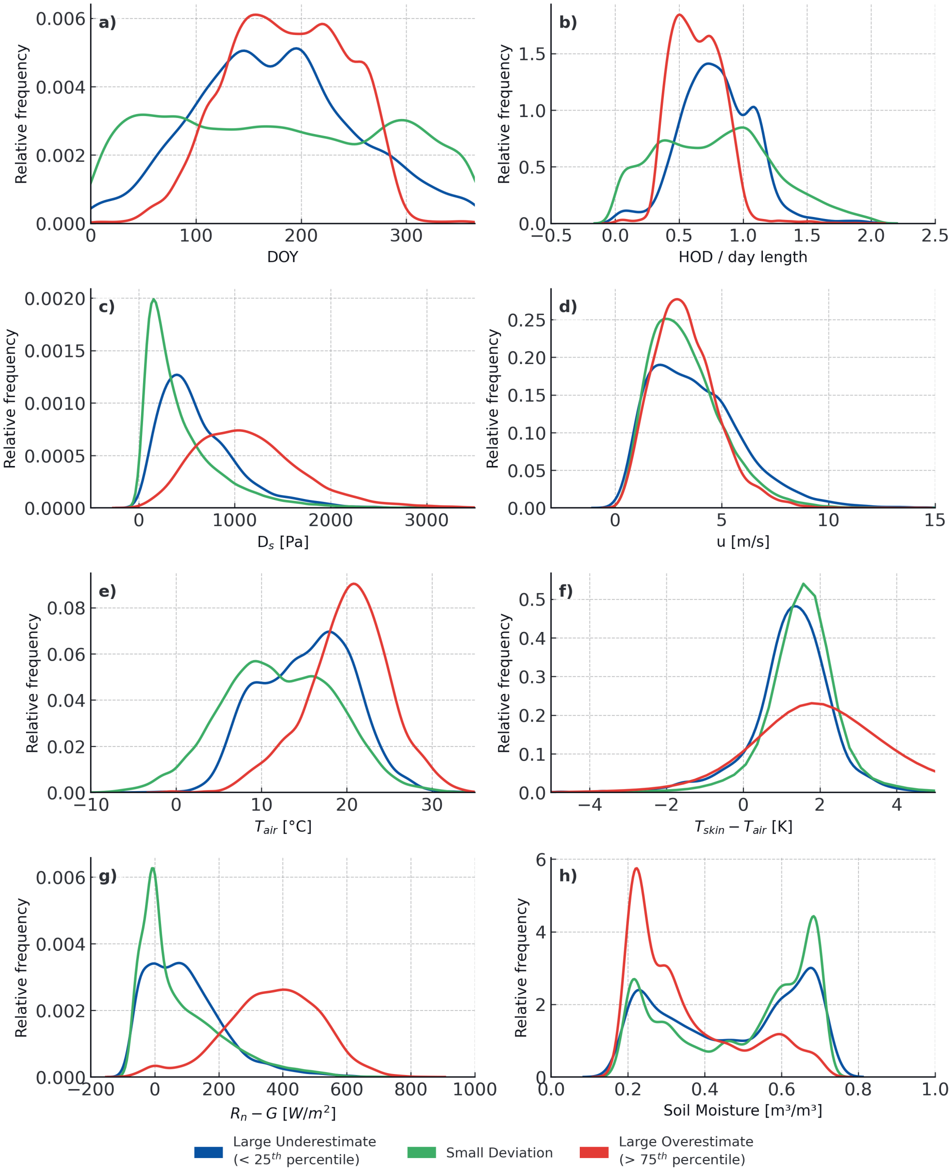

Figure 5.4: Relative frequency distributions in relation to timing (DOY, HOD) and six different environmental variables, for 3 categories of error (model - observations) size over grass. Large underestimates are those below the 25th percentile of all underestimates, while large overestimates exceed the 75th percentile of all overestimates. Small deviations fall between the 75th percentile of underestimates and the 25th percentile of overestimates.

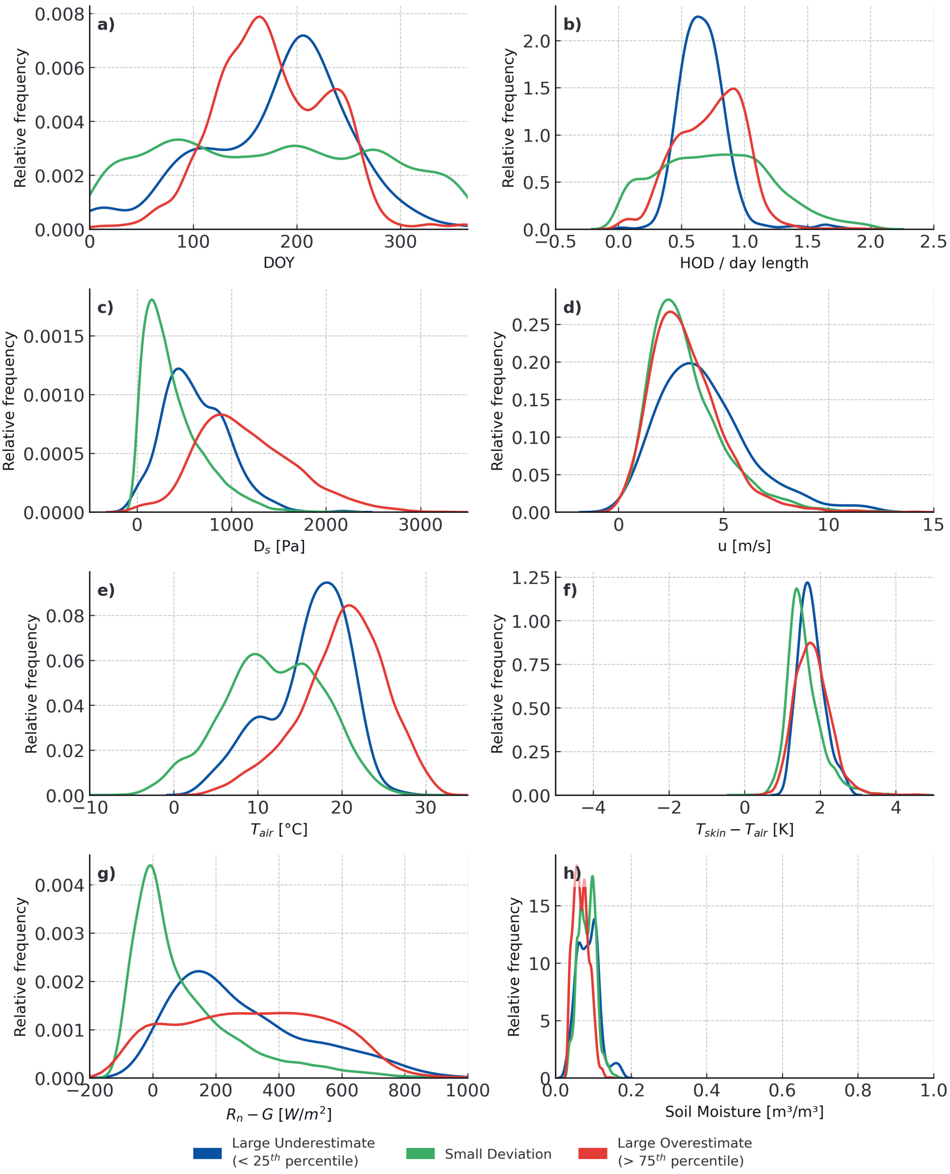

Figure 5.5: Relative frequency distributions in relation to timing (DOY, HOD) and six different environmental variables, for 3 categories of error (model - observations) size over forest. Large underestimates are those below the 25th percentile of all underestimates, while large overestimates exceed the 75th percentile of all overestimates. Small deviations fall between the 75th percentile of underestimates and the 25th percentile of overestimates.

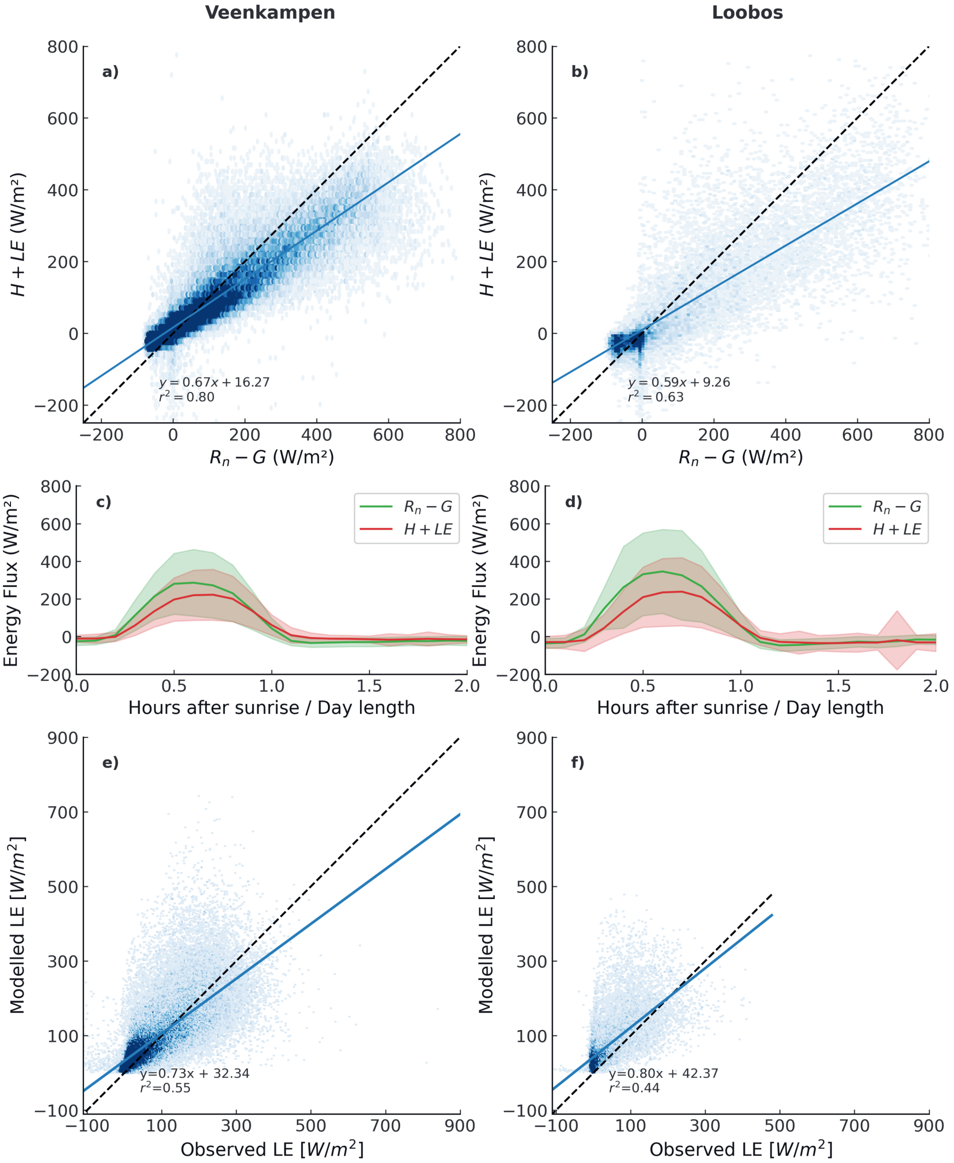

Figure 5.6: Panels a) and b) show the energy balance closure for all observations, while panels c) and d) present the observed average daily cycles of surface fluxes over Veenkampen and Loobos. Panel e) and f) show *LE* estimates from PM with constant r_c, using direct measurements of the air temperature at the surface.

particularly in summer, where errors can reach 10–30% (Twine et al., 2000; Hirschi et al., 2017). Hollinger and Richardson (2005) found that uncertainty in H and LE scales with flux magnitude. In forested environments, this may be attributed to the intermittent nature of turbulence; large, dominant eddies (so-called sweeps) responsible for most of the transport are relatively rare within a standard half-hour averaging period (Raupach et al., 1996).

Alternatively, the energy imbalance might result from overestimating available energy, for example, due to underestimating the ground heat flux (Jacobs et al., 2008). Such underestimations could be the result of damping or phase shifts with depth in the ground (Van de Wiel et al., 2003; Heusinkveld et al., 2004) or the vegetation layer (Van Der Linden et al., 2022). On top of that, (especially tall) vegetation can store heat during the day and release it at night (Lindroth et al., 2010).

For Figure 5.6 e-f LE is described by $LE = -\frac{\rho c_p}{\gamma}\frac{e_a - e_s(T_{air,s,obs})}{r_a + r_c}$ to evaluate the effect of energy *im*balance and test the performance of PM without it. Since we use a direct measurement of the air temperature at the surface, we do not need to approximate it using energy balance closure. Without the energy balance closure assumption, the asymptotic (capping) behaviour disappears. The surface temperature observations do not have a set maximum, and the predicted LE can reach up to 700 and 500 W/m^2 (Fig. 5.6a and b). However, large scatter remains for both locations ($r^2 = 0.55$ for grass and $r^2 = 0.44$ for forest).

Representative surface temperature

Next, we investigate the difference between the (modelled) in-canopy air conditions and the actual conditions *in* the stomata. Since Penman derives T_s from H, (implicitly) the assumption is introduced that the near-surface temperature profile is logarithmic into the vegetation layer, ignoring the roughness sublayer (Sect. 5.1). Secondly, the air is assumed to be saturated at that surface temperature. This means that the latent heat flux is driven by the difference in moisture content between the air at a reference height and fully saturated air at the estimated surface temperature.

Figure 5.7a–b compares modelled and observed surface temperatures. The in-canopy air temperature ($T_{air,s,obs}$) was approximated using (un-)ventilated thermocouples placed within the canopy, and the modelled value is calculated following the Monin-Obukov Similarity theory (MOST). Over grass, the modelled temperature at the roughness height for heat transfer ($T_{air,s,most}$) can differ significantly from the observed air temperature at 10 cm height. During unstable conditions ($L < 0$), the observed surface temperatures are higher than the logarithmic predictions. This can be the result of a measurement error in the surface temperature observations, since in low wind, sunny conditions, a passively ventilated Stevenson screen is prone to overheating (Harrison, 2010). In contrast, forests show smaller differences between air temperatures measured above and within the canopy. This is due to their higher aerodynamic roughness and better mixing of the air. Shade provided by the trees also limits radiation errors in the measurements.

The in-canopy temperature is also higher during the day as it is closely coupled to the vegetation temperature. Under high incoming radiation and low wind speeds, vegetation can be several degrees warmer than the ambient air (Monteith & Unsworth, 1990). In fact, in some situations, the plant temperature can exceed the air temperature by up

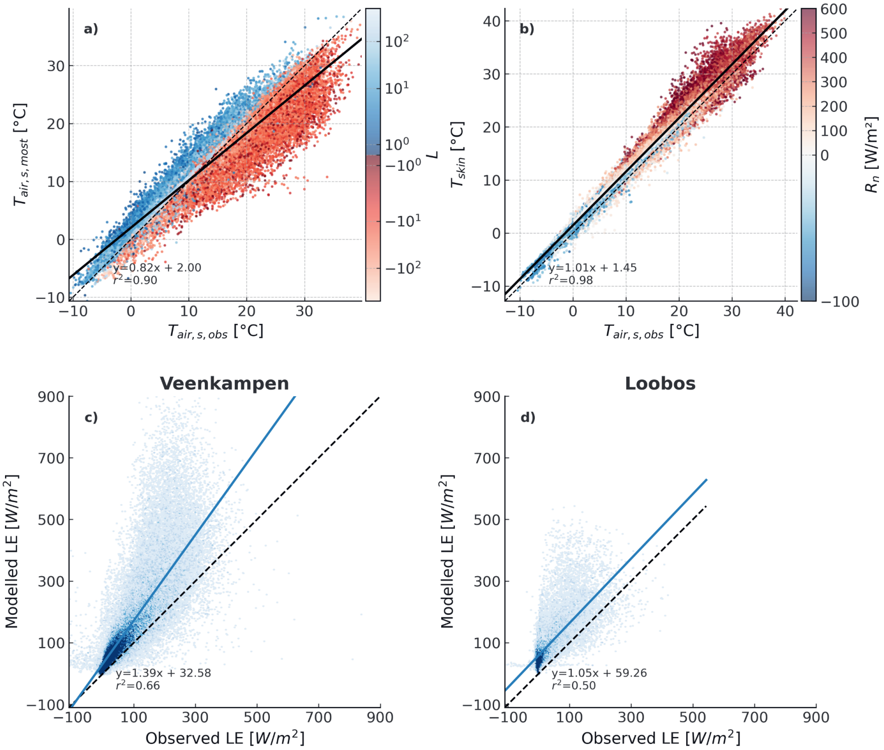

Figure 5.7: Panel a) gives an estimate of the surface temperature as derived using MOST, compared to the measured air temperature at 10 cm at Veenkampen. These observed air temperatures are compared to the observed skin temperature in panel b. Panel c) and d) show *LE* estimates from PM with constant r_c, using direct measurements of the skin temperature. The skin temperature is derived using the Stefan-Boltzmann law with an emissivity of 0.98.

to 10 K (Fig. 5.7 b). This discrepancy is again smaller in forests, where foliage provides self-shading and greater roughness promotes air mixing (Moene & van Dam, 2014).

The Penman-Monteith model applies the big-leaf approach (Deardorff, 1978), which represents vegetation as a single homogeneous layer with no vertical variation, using bulk properties for the entire canopy. Advances in computational resources and improved observations of canopy structure have renewed interest in multi-layer canopy models, which explicitly resolve vertical gradients within the canopy. These models come with significant computational costs while providing only marginal improvements in the representation of latent heat fluxes despite their increased complexity (Bonan et al., 2021). Ershadi et al. (2015) evaluated three different ways of implementing canopy structure into PM and tested this for 20 different flux towers. No modelling structure consistently outperformed the others. This raises the question of whether, in addition to accurately representing variations within the canopy, part of the issue also stems from proper characterisation of the conditions at the leaf scale.

When we use vegetation temperature (estimated from outgoing longwave radiation) to model *LE*, this results in a strong overestimation, especially over grass (Fig. 5.7c and d). This raises questions about whether the assumption of 100% saturation is valid, and whether that is also the case in near-canopy air. It remains uncertain whether the air in the stomata (Wong et al., 2022), leaf boundary layer, and the canopy layer is fully saturated. If the surface air is not saturated, this could explain the overestimations of *LE*. Accurately resolving this would require direct humidity measurements near the leaf surface. Vilà-Guerau de Arellano et al. (2020) show such measurements in a winter wheat canopy that indicate a substantial difference in humidity between the air in and above the canopy.

5.5. CONCLUSION AND RECOMMENDATIONS

In this study, we critically compared the Penman-Monteith model to eddy-covariance measurements at a grass and forest site in the Netherlands. By analysing deviations between the model and observations, we identified under which conditions the largest discrepancies occur, and identified avenues for improvement.

Through statistical analyses of the deviations, we found a difference in the characteristics of the deviations over grass and forest. The systematic bias of Penman-Monteith over grass is mainly caused by regression error, i.e. the deviations are mostly overestimations in situations of large fluxes. Over the forest, the systematic deviations are caused by an average bias, indicative of consistent overestimation of the flux independent of the flux size. The introduction of stomatal resistance models (Jarvis-Stewart and A-gs) does not result in a conclusive improvement of the agreement between the model and observations, suggesting that the disagreement is not solely a result of stomatal behaviour.

Over grassland, the Penman-Monteith model tends to overestimate the latent heat flux especially in the afternoon, when the sun is warming the surface. These moments are prone to decoupling between the vegetation and the overlying air. When we compared the surface temperatures to the MOST predictions, we found that MOST underestimates the temperature near the surface also during the day, since it does not take into account this separate vegetation layer. Sunlight heats the vegetation, and since the wind speeds are relatively low inside the canopy layer, a thick leaf boundary layer can form. This boundary layer insulates the vegetation from the canopy air, trapping heat and moisture. As a result, the air above the canopy may remain relatively cool, ventilated, and unsaturated compared to the vegetation. This is the air that is sampled by the eddy covariance measurement. For this reason, using Penman-Monteith with the conditions inside the stomata (i.e. vegetation temperature and 100% saturation) will not lead to improvement but instead result in even larger overestimations of the latent heat flux.

Another area for improvement lies in the stomatal resistance models. Penman-Monteith accounts for wind speed and atmospheric stability through r_a. However, we also expect an additional effect on the leaf boundary layer, which should be included in r_c. Under high radiation and low wind, the leaf boundary layer grows thicker (Monteith & Unsworth, 1990). This would not only limit heat exchange, but also water vapour transport from the stomata. This resistance could be represented by differentiating between free and forced convection regimes, as is done in leaf energy balance models (Boekee et al., 2023).

The effects of daytime decoupling are more pronounced over grassland than forest. Forest canopies, due to their higher roughness, may have a stronger coupling between the canopy and the air above, which helps reduce temperature and humidity gradients. The largest discrepancies between observations and the model over forest occur in summer and the afternoon. This is likely the cause of the eddy-covariance measurements underestimating the *LE* flux, or an overestimation of the available energy by missed energy storage in the vegetation or an underestimation of the ground heat flux.

Moreover, since aerodynamic resistance is relatively lower over forests, accurately modelling stomatal resistance and scaling it up to represent canopy resistance becomes more critical for correct *LE* flux estimations. Simple upscaling methods, such as using leaf area index (LAI) methods, tend to underestimate canopy resistance (r_c), as parts of the canopy do not actively contribute to the measured fluxes.

To validate these hypotheses, high-resolution temperature and humidity measurements within and just above the vegetation layer are needed. A promising technique for capturing such small-scale variability, particularly over short canopies, is Distributed Temperature Sensing (DTS), as demonstrated by Boekee et al. (2024) and Ter Horst (2025, in review). Once studied in more depth, the decoupling can be integrated in Penman-Monteith by applying roughness sublayer corrections in r_a, and more robust upscaling for r_c. As such, this study concludes that there is a need for a better understanding of variations at the canopy and at the microscale to improve our latent heat flux models.

6

SYNTHESIS

This dissertation is written in the context of spring frost damage in fruit orchards, with a focus on understanding the atmospheric and vegetative interactions that underpin two common protective strategies: 1) wind machines and 2) surface manipulation.

Whether frost damage will occur to a blossom flower depends on its exact temperature. If temperature falls but one degree below a critical threshold, it may die. A single cloud passing by at the right moment may save it. A beautiful example is given in Figure 6.1, where only the upward-facing grapevine buds took damage. Being only millimetres apart, the air temperature difference between the top and bottom of the branch is tiny. However, since the upward-facing buds are exposed to the clear skies, they may cool radiatively to below the air temperature. The bottom-facing buds are protected by the emitted longwave radiation from the surface that keeps them warm.

Naturally, when farmers try to protect their crops, they aim to stay on the safe side, protecting also the most exposed buds and flowers from damage. This requires us not only to understand the air dynamics close to the surface, but also the interactions within the canopy. In the grapevine example, the *air* temperature difference above and below the branch may have been small, but for the buds, the difference in *plant* temperatures was lethal. These differences between air and vegetation temperatures are the focus of Chapter 2 and 3.

Ideally, orchard soils absorb solar radiation during the day and release stored heat at night, helping to mitigate frost risk. However, bare soil is impractical in orchards due to the need for machinery access, making the use of cover crops, such as grass or Dutch clover between tree rows, common practice. A cover crop acts as an insulation layer between the soil and the air, hindering the heat release during the night. The height and density of the cover crop influence its insulating properties.

To understand the effects of cover crops on frost in orchards, we need to understand the roughness sublayer over short vegetation, which has remained poorly studied due to a lack of high-resolution measurement techniques. To better understand how temperature dynamics in an orchard depend on cover crop height, we first studied a simplified system where a grass layer is the only canopy. Heat and water exchange over a short canopy are

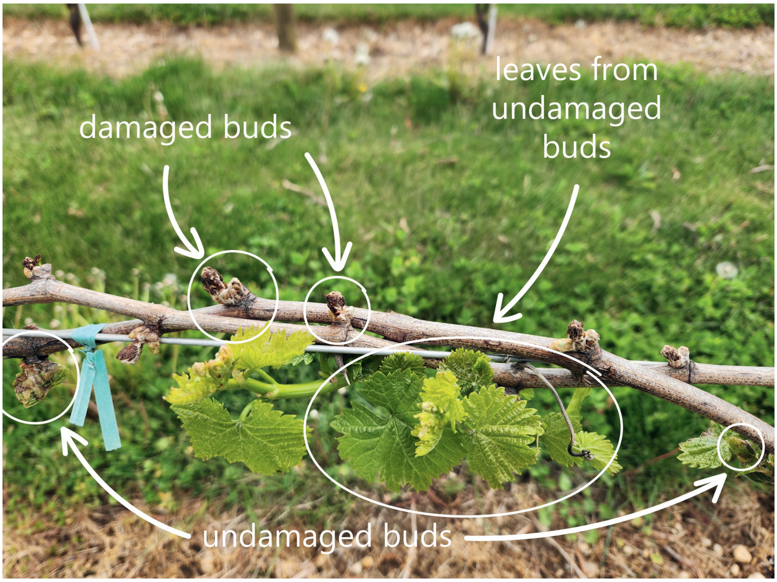

Figure 6.1: Picture of grapevines on Long Island (NY, USA) that experienced frost damage. Only the buds on the upper-facing side of the cane took damage, while the downward-facing buds survived. Also, note that grass is removed directly underneath the vines to enhance energy release from the soil at night. Photo by Jason Londo.

therefore the focus of Chapter 4 and 5.

The next sections will first summarise the main findings per chapter, and then provide the main insights that can be gained from the thesis as a whole.

6.1. MAIN FINDINGS

Chapter 2 examines how wind machine operation affects plant and air temperature in a pear orchard. Using DTS (Distributed Temperature Sensing), we measured both vertical and horizontal temperature profiles in a pear orchard at very high spatial and temporal resolution.

During a radiative frost night (clear skies, low wind), we observed the development of a clear canopy layer prior to wind machine operation. Above the canopy, the temperature increases sharply, but inside the canopy layer the temperature becomes uniform. Outgoing longwave radiation cools the soil and vegetation at the surface. This cold surface cools the air above it. Since there is little wind, the atmosphere is stable, and the cold air remains between the trees.

We showed the dual effect of a wind machine upon operation: 1) the mixing of the stratified air above into the canopy layer and 2) the erosion of the leaf boundary layer to facilitate plant-air heat exchange. The wind machine creates a jet that mixes warm air down to the canopy. However, the foliage reduces the plume penetration towards the ground. Multiple rotations (~ 15) were needed to reach stable mixing, and at this point only the upper 30% to 60% of the canopy layer was well-mixed, depending on the distance to the wind machine. As the foliage becomes denser throughout the season, these effects become stronger.

Over every rotation cycle, leaves that radiatively cooled below air temperature are warmed up to air temperature, as strong advective warming repeatedly dominates over radiative cooling. Thinner flower petals closely follow air temperature, in contrast to thicker shoots that show a strongly dampened response, as they act as heat reservoirs and retain warmth from daytime heating.

Chapter 3 explores the physiological effects of sub-zero temperature on plants. As daytime temperatures rise in spring and dormancy is broken, fruit trees begin to lose their cold hardiness: their natural resistance to freezing conditions. This is why a spring frost can cause severe damage to sensitive tissues, such as buds and flowers.

The temperature range within which freezing causes irreversible damage is called the critical temperature range. This range is commonly determined using differential thermal analysis (DTA): a technique that detects freezing exotherms (i.e. the release of heat during ice formation) in small tissue samples. However, because DTA is laboratory-based and not suitable for field applications, it has limitations for in situ monitoring.

We explored the potential of high-resolution thermal cameras for in situ monitoring. Experiments conducted in a controlled freezing chamber with samples of apple cultivars demonstrated that thermal cameras can detect freezing exotherms in buds, leaves, and flowers. While our small sample size introduced considerable variability and hindered statistically robust conclusions, the results demonstrated the potential of this technique. We recommend further exploration of thermal imaging for in situ monitoring of critical freezing temperatures. For instance, thermal cameras could be employed to study how different cover crop treatments influence freezing behaviour across multiple trees.

These cover crops were the motivation behind **Chapter 4**. Typically, logarithmic temperature profiles derived for the atmospheric surface layer are extrapolated down to the ground, into the roughness surface layer. However, in this layer, the flow is distorted by the vegetation elements. Using a DTS array, we measured the sharp temperature gradients near the surface and revealed that the temperature profiles in the lowest 1 – 2 m are not logarithmic, but instead exhibit near-linear behaviour.

Building on this finding, we drew inspiration from the Van Driest formulation, which describes the transition from logarithmic to linear behaviour in velocity profiles near smooth surfaces. We developed an analogous model to describe temperature gradients near rough, vegetated surfaces. The model introduces a new length scale that represents the size of the smallest turbulent eddies near the surface and links directly to the vegetation dimensions. The model provides an improved, more robust, description of near-surface temperature profiles.

Stepping away from the logarithmic descriptions of temperature in the canopy layer will also affect our predictions of the surface heat and moisture fluxes. In **Chapter 5** we therefore take a critical look at our predictions of latent heat fluxes.

One of the most used evaporation models is the Penman-Monteith model (PM), which distinguishes itself by its physics-based approach and use of a limited number of commonly available meteorological variables. PM builds on the assumption of logarithmic momentum, heat and moisture profiles near the surface.

In Chapter 5 we compare the PM model to long-term eddy-covariance evaporation measurements for two sites: grassland and forest. We show that overestimations of PM relative to observations occur most frequently during high radiation, high temperature, and low humidity conditions. We identified possible pathways for future improvement.

First, the discrepancy between the model and the observations can be attributed to a bias in the observations. EC measurements are known to be prone to underestimating high fluxes, especially over tall canopies.

Second, at the canopy level PM does not include the decoupling between the vegetation and overlying air. These effects are stronger over grass than over forest, as forest may (due to its higher roughness) have stronger coupling between canopy and above-canopy air. Moisture and heat may remain trapped inside the canopy-layer. As a result, the air above the canopy may remain relatively cool, ventilated, and unsaturated compared to the vegetation. These above-canopy conditions are driving the fluxes measured by the eddy-covariance, while PM is based on the conditions inside the canopy layer.

Finally, open questions remain about the conditions at leaf level: 1) are the stomata 100% saturated, 2) do stomatal conductance models capture diurnal variation correctly, and 3) is the leaf-boundary layer conductance sufficiently included?

6.2. INSIGHTS AND IMPLICATIONS

A recurring topic in the four chapters of this thesis is the difference between vegetation and air temperature and the implications thereof. While the first two chapters focus on the direct consequences for an applied problem, the last two chapters highlight the importance for accurate modelling of surface-atmosphere interactions. I believe that this difference is often overlooked in models, and that may be a direct result of how '*surface temperature*' is measured.

An example of this ambiguity can be found when we compare some of the results of Chapter 4 and 5. Chapter 4 showed that the temperature profiles according to the Monin-Obukov Similarity Theory tend to underestimate/overestimate the surface temperature during respectively stable/unstable conditions during our field campaign. However, in Chapter 5, we show the opposite for 10 years of data from the same location. Underlying this seemingly contradictory statement are the different measurement techniques, as visualised in Figure 6.2.

In Chapter 4 we take the surface temperature to be the *air* temperature measured with DTS at the top of the grass layer. Since DTS is sensitive to radiative biases, it may overestimate the air temperature during the day, and underestimate it during the night. Luckily, since the cable is relatively thin and white, these biases are limited. In Chapter 5 the surface temperature more closely resembles the *vegetation* temperature. Here, it is measured using a thermistor covered by a passively ventilated, radiative shield. The sensor is placed at 10 cm, at the top of the grass. When the passive ventilation is insufficient, the thermistor may give a more representative measurement of the air temperature inside the grass canopy than of the "undisturbed" air above it. Since the grass is heated radiatively, its temperature (i.e. the tissue temperature) is higher than the air temperature. As such, the shielded thermistor may overestimate air temperatures during the day and underestimate them during the night. The same applies to the skin temperature as measured with the pyrgeometer, which is a direct measurement of the surface temperature (instead of the air). Lastly, MOST defines the surface temperature as the air temperature at height z_{0h}, i.e. below the grass height, as if there were no vegetation. Due to its logarithmic shape, during

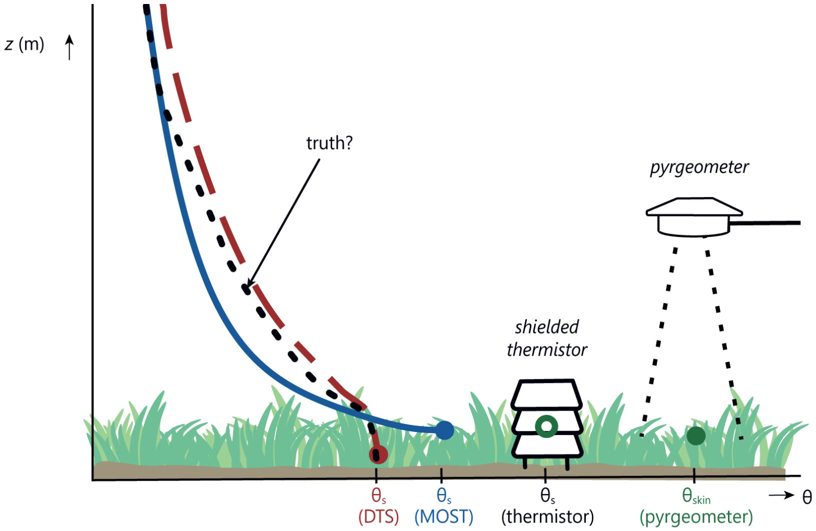

Figure 6.2: Different measurement techniques for the surface temperature and their typical daytime bias compared to each other. The black line represents a best guess of the potential air temperature near the surface.

the day this will give a higher temperature than the air temperature measured with DTS, but a lower temperature than the vegetation temperatures measured with the thermistor.

To accurately predict frost damage or evapotranspiration (and to protect crops), we thus need to be aware of these differences in what the instruments are measuring. This means identifying the specific temperature that truly matters, whether it's the average canopy skin temperature, the temperature of a single leaf, or the average air temperature within the canopy (Hicks & Eash, 2021). Achieving this requires a deeper understanding of the microclimate within a short canopy, rather than relying on crude resistance laws.

6.3. OUTLOOK

To get an accurate estimate of the conditions of the vegetation, we do not only need to measure the air temperature, but also radiation, wind speed, humidity and CO_2 within the canopy. These variations in micro-climate have been studied over the last decades for *tall* canopies, such as boreal forest (e.g. Harman & Finnigan, 2007, 2008) or Amazonian rainforest (e.g. González-Armas et al., 2024). Based on that, various radiation extinction models have been developed, ranging from simple exponential formulations for light penetration into the canopy (Ronda et al., 2001), to more complex models that account for leaf area index and solar zenith angle (ECMWF, 2024), and even detailed ray-tracing approaches (Vos et al., 2010). Heat and moisture exchange is solved by applying resistance laws and solving energy balances for different vegetation layers (Monteith & Unsworth, 1990), while momentum exchange is typically solved using drag laws (Brunet, 2020). Based on this (in combination with stomata models, incorporating plant hydraulics), multilayer models have been developed for tall canopies (Bonan et al., 2021).

While they have delivered valuable insights for tall canopies, I believe that for low canopies, multilayer models may not be the best way forward for land surface models. Here, a better description of temperature, humidity and wind inside the canopy may be achieved with simple improvements of the parameterisations. The first steps in this direction have already been taken for heat in terms of diffusion analogies (Van Der Linden et al., 2022). As a result of solar radiation, the temperature at the top of the grass shows a strong diurnal cycle with an amplitude that can be in the order of 20-30 K. Just below the grass, in the soil, this amplitude is already reduced by 10 degrees. On top of that, heat storage in the vegetation results in a phase lag and frequency-dependent damping. In the current resistance-based models, these damping and lagging effects are ignored. By taking inspiration from soil models, Van Der Linden et al. (2022) showed that a diffusion model can be used to describe the energy transport through grass more accurately.

Such diffusion models (combined with radiation models) could then be applied to resolve air temperatures inside the grass layer. Fine-scale measurements are crucial to validate these models. For temperature, we have developed a parametric DTS setup to measure at the mm-scale (Figure 6.3) (ter Horst et al., 2025). Note that this can be applied to measure fine-scale temperature variations inside the canopy layer, as compared to the harp in Chapter 4. DTS has the potential to also be used for moisture (Schilperoort et al., 2018) and wind measurements (van Ramshorst et al., 2020), but other micro-sensors (e.g. as used in the CloudRoots campaign (Vilà-Guerau de Arellano et al., 2020)) may be easier to use.

With a better understanding of the microclimate within vegetation, we may be able to address some of the unresolved questions remaining at the end of this thesis. For example: How is nighttime heat release influenced by grass height? What humidity gradient truly drives transpiration; can we assume a saturated leaf surface? Answering these questions could improve our ability to protect crops not only from abiotic stresses like frost and water scarcity but also from biotic stresses such as pathogen outbreaks, which are closely tied to humidity levels within the canopy. In the long term, this knowledge hopefully contributes to more sustainable agricultural practices, helping to meet the rising food demand in a changing world.

Figure 6.3: DTS coil to measure near-surface air temperatures above and inside the grass layer. Photo by Tijn ter Horst.

A

APPENDICES

A.1. CHAPTER 2

A.1.1. PARAMETERIZATION OF HEAT TRANSFER: A CONCEPTUAL BACKGROUND

The regime transitions between free and forced convection are often described in terms of (rigid) thresholds based on a Richardson criterion (Section 2.2.2), but are not sharply defined in literature. For example, Parkhurst et al. (1968) sets the limits for 5% departure from pure free or forced convection at $0.1 < \mathrm{Ri} < 16$. Monteith and Unsworth (1990) states that mixed convection is probable for $0.1 < \mathrm{Ri} < 10$. As such the 'threshold' are mere indicators of transition based on empirical evidence and they will vary strongly with the dimensions of the plant surface and the turbulent conditions of the air. Table A.1 shows an example of how the Richardson number can be used to define boundaries between the different convection regimes, and how the Nusselt number is parameterised for those different scenarios. In reality, regime transitions are smoother.

As a simpler alternative that allows for a smoother (i.e. more natural) transition between the regimes, here we present a conceptual picture based on a mechanistic approach. By introducing a free-convection type of velocity scale, we show how the Nusselt number can be calculated directly as to avoid the use of different formulations in the free and forced convection regimes.

FREE CONVECTION VELOCITY SCALE

In a situation with no background wind, air movement results from the air density difference between the relatively warm/cold air above the leaf surface and the surrounding air (i.e free convection). The *apparent* gravity force g^* on an air parcel over a leaf surface can be calculated by correcting the gravity force F_g for the buoyant force F_B [N]:

$$F_g = F_B \tag{A.1}$$

$$\rho_{air} V a = (\rho_{plant} - \rho_{air}) V g \tag{A.2}$$

where ρ_{air} is the density of air outside of the leaf boundary layer [kg m^{-3}], V is the volume of an air parcel [m^3] and a is its acceleration [m s^{-2}]. ρ_{plant} is the air density within the leaf boundary layer, and g is the gravitational acceleration of 9.81 m s^{-2}. This gives the apparent gravity g^* [m s^{-2}].

$$g^* = a = g\frac{\rho_{plant} - \rho_{air}}{\rho_{air}} = g\frac{T_{plant} - T_{air}}{T_{air}} \tag{A.3}$$

The typical velocity scale w^{free} for free convection can then be derived from the apparent gravity and the typical length scale L ($L = \frac{1}{2}g^* t^2$):

$$w^{free} = tg^* = \sqrt{2Lg^*} \tag{A.4}$$

When we take the squared ratio of the buoyant velocity scale to the wind speed, we notice that this is equal to twice the Richardson number.

$$\left(\frac{w^{free}}{u}\right)^2 = \frac{2Lg^*}{u^2} = \frac{\frac{g\cdot L^3\cdot\frac{(T_{plant}-T_{air})}{T_{air}}}{\nu^2}}{(\frac{uL}{\nu})^2} = \frac{2Gr}{Re^2} = 2Ri \tag{A.5}$$

So, this suggests that the Grashof number can also be seen as the square of a characteristic Reynold number for w^{free}. This vision can be appreciated from Table A.1 where the powers in the Grashof formulations are roughly half of the Reynolds powers. As such, instead of using the *different* parameterisations for Nu based on Re and Gr, we introduce a parameterisation based on a *single* Reynolds number. To this end, we will base Reynolds number Re^* on the refreshment velocity m^*, which combines the background velocity and w^{free}.

$$m^* = \sqrt{(w^{free})^2 + u^2} \tag{A.6}$$

This new view reduces the need for the different formulations (tab. A.1) to one equation, suitable for all quasi-laminar regimes ($\mathrm{Re}^* < 2\cdot 10^4$):

$$\mathrm{Nu} = 0.6\cdot(\mathrm{Re}^*)^{0.5} \tag{A.7}$$

and one for all turbulent regimes ($\mathrm{Re}^* > 2\cdot 10^4$):

$$\mathrm{Nu} = 0.032\cdot(\mathrm{Re}^*)^{0.8} \tag{A.8}$$

Here we select the original parametrisation for laminar and turbulent flow. Perhaps, the complexity could be further reduced when both regimes are merged into a single formulation for all Reynolds regimes. This follows from the fact that the lower coefficient in Equation A.8 is partly compensated by a higher power. However, designated laboratory experiments are needed in order to investigate this from a parameter perspective. Here we restrict ourselves to the conceptual view, rather than to finding the most optimal parameters.

Finally, we notice that in the analysis aspects of branch and leaf vibration as a result of the wind are not taken into account explicitly. In reality however, those effects are likely to be important. Below, it will be motivated that those physical effects do have an effect on the characteristic length scale choices made.

Table A.1: Original flow regime criteria given in Monteith and Unsworth (1990) as to calculate the Nusselt number under different conditions. Where the table is based on rigid criteria, here a smoother alternative is given.

			Nu=
free convection	$Ri > 10$	$T_{plant} \leq T_{air}$	$0.13 \cdot Gr^{0.33}$
		$T_{plant} > T_{air}$	$0.50 \cdot Gr^{0.25}$
forced convection	$Ri < 0.1$	$Re \leq 2 \cdot 10^{-4}$	$0.60 \cdot Re^{0.5}$
		$Re > 2 \cdot 10^{-4}$	$0.32 \cdot Re^{0.8}$
mixed convection	$0.1 < Ri < 10$		$\left(Nu_{free}^{3.5} + Nu_{forced}^{3.5}\right)^{1/3.5}$

TYPICAL LENGTH SCALE

Note that due to every flower's, leaf's or shoots' unique shape it is hard to define a typical length scale used to calculate w^{free}. For a sphere, cylinder or flat plate the diameter or length in the direction of the wind would be a logical choice. For an irregularly shaped leaf fluttering in the wind, the characteristic dimension L can be anything between the thickness and the maximum length of the leaf. We expect typical length scales to be between 0.5 – 0.8 times the maximum leaf dimension (Schuepp (1993) and Parkhurst et al. (1968)). Figure A.1 shows three different scenarios to explain this statement. During conditions of forced or mixed convection, there is a slight background wind, and leaves are usually streamlining along the flow, like in Figure A.1a (though often vibrating as well). For leaves that are not streamlining, anabatic effects and flow detachment will start to play a role, elongating the acceleration time (Fig. A.1b). For situations of no flow, Kitamura et al. (2015) and Graefe et al. (2022) show that for respectively horizontal (fig A.1c) or (vertically) inclined leaves (fig A.1d), the typical length is chosen along the steepest ascent of the leaf surface and thus also in the order of magnitude of the leaf length. For this reason in the analysis above the maximum leaf length is taken as the characteristic length scale (rather than e.g. leaf thickness).

A.1.2. MODEL ITERATION PARAMETERS

The values for the typical length scale and thickness should be interpreted with care. They do not represent the actual shape of the plant organ, but are used to determine the surface/volume ratio and are representative of the typical length scale (see also Appendix. A.1.1).

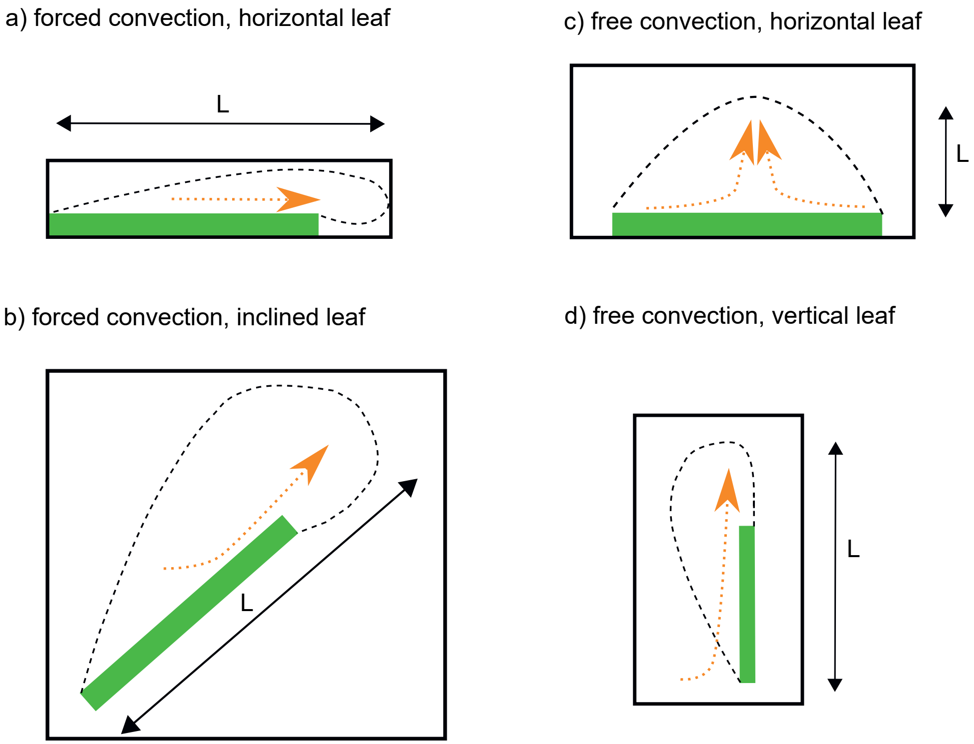

Figure A.1: Different scenarios for flow along a leaf. Panel a) and b) show forced convection scenarios with horizontal or inclined leaf. Panel c) and d) show free convection for horizontal or vertical leaves. The orange arrow illustrates a possible flow path. While the black arrow illustrates a typical length scale.

Table A.1: Parameters used for modelling the plant tissue temperature. Exact values of constant α [-], thickness of the plant organ t_{plant} [mm], representative length scale L [mm], Sky View Factor SVF [-] and wind reduction factor γ [-] were determined through calibration within the given range [minimum.. maximum, number of evenly spaced samples]. ε is the emissivity [-] (same for all organs) and c_p is the heat capacity of the plant tissue [J kg^{-1} K^{-1}].

	Shoot	**Leaf**	**Flower**	**Calibration range**
α	22			[0..50; # = 10]
t_{plant}		0.2	0.12	[0.1..1, # =10] for leaf [0.01..1, # = 10] for flower
L	1.2	40	3.4	[0.1..10, # = 10] for shoot [10..100, # = 10] for leaf [0.1..10, # = 10] for flower
SVF	1	0.1	0	[0..1 , # = 11]
γ	1	0.8	1	[0..1 , # = 11]
ε_{air}	0.8			
ε_{plant}	0.96			
ε_{soil}	0.98			
c_{plant}	$4.2 \cdot 10^6$	$2.0 \cdot 10^6$	$0.5 \cdot 10^6$	

A.2. CHAPTER 4

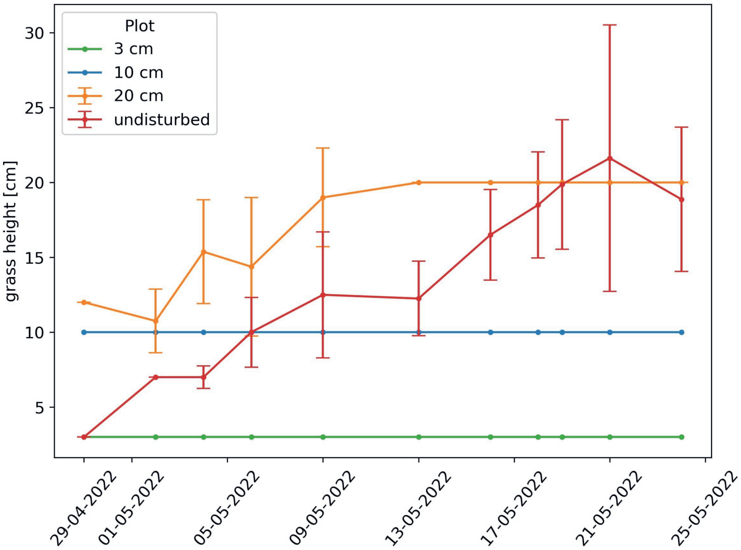

Figure A.2: Grass height as measured over time, with uncertainty bars giving the standard deviation for the growing grass based on 8 measurements. There is no standard deviation measured for the 3 cm and 10 cm plots, as the grass was kept at a constant height.

A.2.1. DERIVATION NORMALISED MODELS

In the next section, we study the behaviour of the Monin–Obukov Similarity Theory, the Van Driest model, and a simple and complex RSL correction for tall canopies. We derived the appropriate length scales to normalise the models by studying the limit behaviour near the surface. Next, the limits of the normalised models and their derivatives were studied. This shows how the adapted Van Driest model and the RSL corrections have the same limit of 1 near the surface but differ in their second derivative.

NORMALISED MONIN–OBUKOV EQUATION

For the normalisation, we used the following normalised variables:

$$\hat{\theta} = \frac{\theta}{\theta_*}, \hat{z} = \frac{z}{L_s}, \hat{L} = \frac{L_{ob}}{L_s} \tag{A.9}$$

This gives:

$$\frac{\partial \hat{\theta}}{\partial \hat{z}} \frac{\kappa \hat{z}}{1} = \Phi_h \left(\frac{\hat{z}}{\hat{L}} \right), \tag{A.10}$$

NORMALISED VAN DRIEST EQUATION

The Van Driest equation is given by Donda et al. (2014) as:

$$u_*^2 = \left[\frac{(A\kappa z)^2 \frac{\partial u}{\partial z}}{\Phi_n \left(\frac{z}{L_{ob}} \right)^2} + \nu \right] \frac{\partial u}{\partial z} \tag{A.11}$$

Rewriting gives:

$$u_* = \left[\frac{(A\kappa z)^2 \frac{\partial u}{\partial z}}{u_* \Phi_m \left(\frac{z}{L_{ob}} \right)^2} + (\nu / u_*) \right] \frac{\partial u}{\partial z} \tag{A.12}$$

Taking the limit at the surface gives the scaling parameters u_* and ν / u_*.

$$\lim_{z \to 0} u_* = [0 + (\nu / u_*)] \lim_{z \to 0} \frac{\partial u}{\partial z} \tag{A.13}$$

$$\lim_{z \to 0} \frac{\partial u}{\partial z} = \frac{u_*}{(\nu / u_*)} \tag{A.14}$$

For a rough surface, we replaced the viscous length scale u_* / ν with L_s. This gives:

$$u_* = \left[\frac{(A\kappa z)^2 \frac{\partial u}{\partial z}}{u_* \Phi_h \left(\frac{z}{L_{ob}} \right)^2} + L_s \right] \frac{\partial u}{\partial z} \tag{A.15}$$

Replacing momentum by heat:

$$\theta_* = \left[\frac{(A\kappa z)^2 \frac{\partial\theta}{\partial z}}{\theta_* \Phi_h \left(\frac{z}{L_{ob}}\right)^2} + L_s \right] \frac{\partial\theta}{\partial z} \tag{A.16}$$

Replacing θ and z for their normalised values:

$$1 = \left[\frac{(A\kappa \hat{z})^2 \frac{\partial\hat{\theta}}{\partial\hat{z}}}{\Phi_h^2(\frac{\hat{z}}{\hat{L}})} + 1 \right] \frac{\partial\hat{\theta}}{\partial\hat{z}} \tag{A.17}$$

This can be solved with the quadratic formula, which has only one physical solution:

$$\frac{\partial\hat{\theta}}{\partial\hat{z}} = \frac{-1 + \sqrt{1 + 4\left(\frac{A\kappa\hat{z}}{\Phi_H\left(\frac{\hat{z}}{\hat{L}}\right)^2}\right)^2}}{2\left(\frac{A\kappa\hat{z}}{\Phi_H\left(\frac{\hat{z}}{\hat{L}}\right)^2}\right)^2} \tag{A.18}$$

The normalised gradient is always positive; in stable situations, both the gradient and θ_* are positive, while in unstable situations, a negative θ_* corresponds to a negative gradient, which then results in a positive normalised gradient.

To derive the limit at the surface, we applied a Taylor expansion, relying on the binomial series: $(1+x)^{1/2} = 1 + \frac{1}{2}x - \frac{1}{8}x^2 + \frac{1}{16}x^3 - ...$

$$\frac{\partial\hat{\theta}}{\partial\hat{z}} = \frac{-1 + 1 + 2\left(\frac{A\kappa\hat{z}}{\Phi_H\left(\frac{\hat{z}}{\hat{L}}\right)^2}\right)^2 - \left(\frac{A\kappa\hat{z}}{\Phi_H\left(\frac{\hat{z}}{\hat{L}}\right)^2}\right)^4}{2\left(\frac{A\kappa\hat{z}}{\Phi_H\left(\frac{\hat{z}}{\hat{L}}\right)^2}\right)^2} = 1 - \frac{1}{2}\left(\frac{A\kappa\hat{z}}{\Phi_H\left(\frac{\hat{z}}{\hat{L}}\right)^2}\right)^2 \tag{A.19}$$

Using the standard Φ_H-relation (see Sect. 4.2), the limit of $z \to 0$, for $\frac{\partial\hat{\theta}}{\partial\hat{z}}$ goes to 1. The second derivative becomes:

$$\frac{\partial^2\hat{\theta}}{\partial\hat{z}^2} = -\left(\frac{A\kappa\hat{z}}{\Phi_H\left(\frac{\hat{z}}{\hat{L}}\right)^2}\right) \tag{A.20}$$

So, the limit of the curvature for $z \to 0$ thus goes to 0.

NORMALISED DE RIDDER EQUATION

De Ridder (2010) presents a simple bulk transfer model to account for RSL effects over tall canopies. The model for neutral conditions is given by:

$$\frac{\partial\theta}{\partial z} = \frac{\theta_*}{\kappa z}\left(1 - e^{\mu z/z_*}\right) \tag{A.21}$$

We can recognise a correction term $\left(1 - e^{\mu z/z_*}\right)$. We translated this into a length-scale type expression, that scales height with z_* as a new length scale, similar to our L_s approach.

Here z_* represents the height of the roughness sublayer and $\mu \approx 0.95$ is an empirical constant. We merged these into $\gamma = \mu / z_*$.

Using Taylors' expansion this gives:

$$\frac{\partial \theta}{\partial z} = \frac{\theta_* \gamma z - \frac{\theta_* \gamma^2 z^2}{2} + \frac{\theta_* \gamma^3 z^3}{6} + \dots}{\kappa z} = \frac{\theta_* \gamma - \frac{\theta_* \gamma^2 z}{2} + \frac{\theta_* \gamma^3 z^2}{6} + \dots}{\kappa} \tag{A.22}$$

Taking the limit at the surface gives the scaling parameters:

$$\lim_{z \to 0} \frac{\partial \theta}{\partial z} = \frac{\theta_* \gamma}{\kappa} \tag{A.23}$$

This gives a length scale $L_R = \kappa / \gamma = \kappa z_* / \mu$.

The non-dimension equation then becomes:

$$\frac{\theta_*}{L_R} \frac{\partial \hat{\theta}}{\partial \hat{z}} = \frac{\theta_*}{\kappa \hat{z} L_R} \left(1 - e^{-L_R \hat{z} L_R}\right) = \frac{1}{\kappa z} \left(1 - e^{-\hat{z}}\right) \tag{A.24}$$

To derive the limit, we applied Taylors' expansion:

$$\frac{\partial \hat{\theta}}{\partial \hat{z}} = \frac{\kappa \hat{z} - \frac{\kappa^2 \hat{z}^2}{2} + \frac{\kappa^3 \hat{z}^3}{6} + \dots}{\kappa z} = 1 - \frac{\kappa z}{2} + \frac{\kappa^2 z^2}{6} + \dots \tag{A.25}$$

The limit of $z \to 0$ is at 1.

The second derivative becomes:

$$\frac{\partial^2 \hat{\theta}}{\partial \hat{z}^2} = \frac{\kappa}{2} + \frac{\kappa^2 z}{3} + \dots \tag{A.26}$$

The limit of the curvature for $z \to 0$ thus goes to $\frac{1}{2}\kappa$.

NORMALISED HARMAN AND FINNIGAN EQUATION

The model dominating the field of canopy-layer turbulence is the Harman and Finnigan model (Harman and Finnigan (2007, 2008)). Harman and Finnigan provide a continuous model for RSL correction $\phi(z/L_s)$ with an exponential shape that asymptotically approaches 1 at 2 – 3 times the roughness sublayer height. This model has been implemented in the Community Land Model, and showed a substantially improved prediction of the surface exchange over several surface types, among which is grassland (Bonan et al. (2018) and Oleson et al. (2010)). An important feature of the Harman and Finnigan model is that they introduce the virtual displacement height (d_v), which scales with u_*^2, and lowers the displacement height compared to the origin.

In a very simplified form, this model can be written as:

$$\frac{\partial \theta}{\partial z} = \frac{\theta_*}{\kappa (z + d_v)} \Phi_h \left(\frac{z}{L_{ob}} \right) \tag{A.27}$$

Taking the limit at the surface gives the scaling parameters:

$$\lim_{z \to 0} \frac{\partial \theta}{\partial z} = \frac{\theta_*}{\kappa d_v} \tag{A.28}$$

This gives us the length scale $\kappa d_v = L_{HF}$, and temperature scale θ_*.

If we normalise this equation using a length scale L_{HF}, the equation (for neutral conditions) becomes:

$$\frac{\theta_*}{L_{HF}}\frac{\partial\hat{\theta}}{\partial\hat{z}} = \frac{\theta_*}{\kappa(\hat{z}L_{HF}+d_v)} \tag{A.29}$$

$$\frac{\theta_*}{L_{HF}}\frac{\partial\hat{\theta}}{\partial\hat{z}} = \frac{\theta_*}{\kappa d_v+\kappa\hat{z}L_{HF}} \tag{A.30}$$

$$\frac{\partial\hat{\theta}}{\partial\hat{z}} = \frac{L_{HF}}{\kappa d_v+\kappa\hat{z}L_{HF}} \tag{A.31}$$

Using $L_{HF} = \kappa d_v$, this gives:

$$\frac{\partial\hat{\theta}}{\partial\hat{z}} = \frac{1}{1+\kappa\hat{z}} \tag{A.32}$$

So, the limit of $z \to 0$ is at 1.

The second derivative becomes:

$$\frac{\partial^2\hat{\theta}}{\partial\hat{z}^2} = \frac{-\kappa}{(1+\kappa\hat{z})^2} \tag{A.33}$$

The limit of the curvature for $z \to 0$ thus goes to $-\kappa$.

A.3. CHAPTER 5

A.3.1. RELATIVE FREQUENCY DISTRIBUTIONS JARVIS-STEWARD AND A-GS

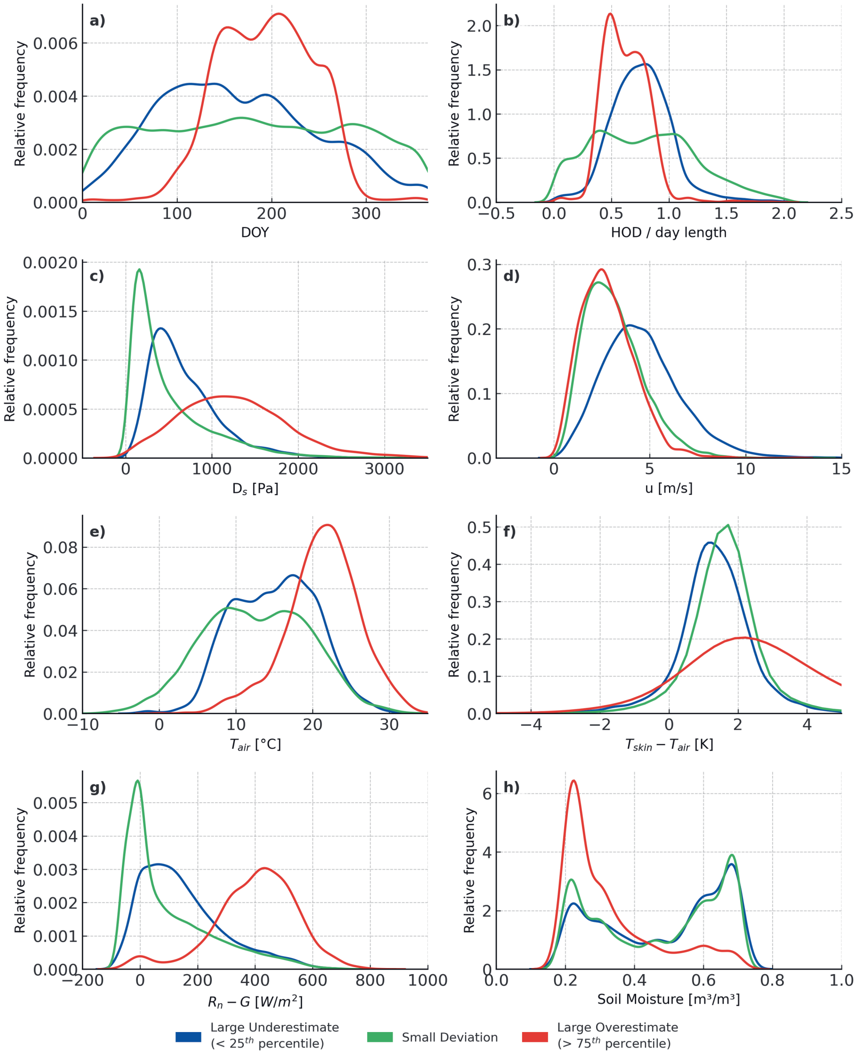

Figure A.3: Relative frequency distributions in relation to timing (DOY, HOD) and six different environmental variables, for 3 categories of error (model - observations) size over grass using Jarvis-Stewart. Large underestimates are those below the 25th percentile of all underestimates, while large overestimates exceed the 75th percentile of all overestimates. Small deviations fall between the 75th percentile of underestimates and the 25th percentile of overestimates.

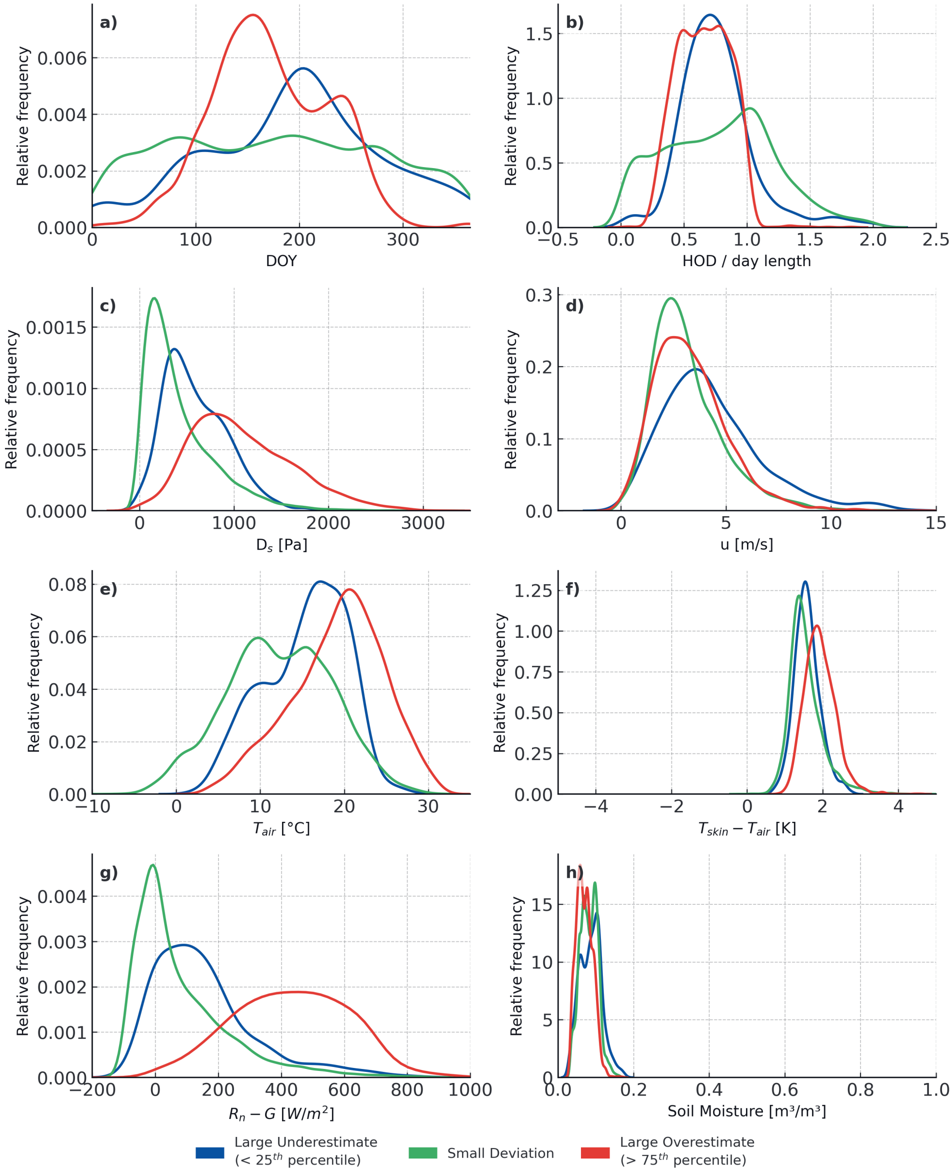

Figure A.4: Relative frequency distributions in relation to timing (DOY, HOD) and six different environmental variables, for 3 categories of error (model - observations) size over forest using Jarvis-Stewart. Large underestimates are those below the 25th percentile of all underestimates, while large overestimates exceed the 75th percentile of all overestimates. Small deviations fall between the 75th percentile of underestimates and the 25th percentile of overestimates.

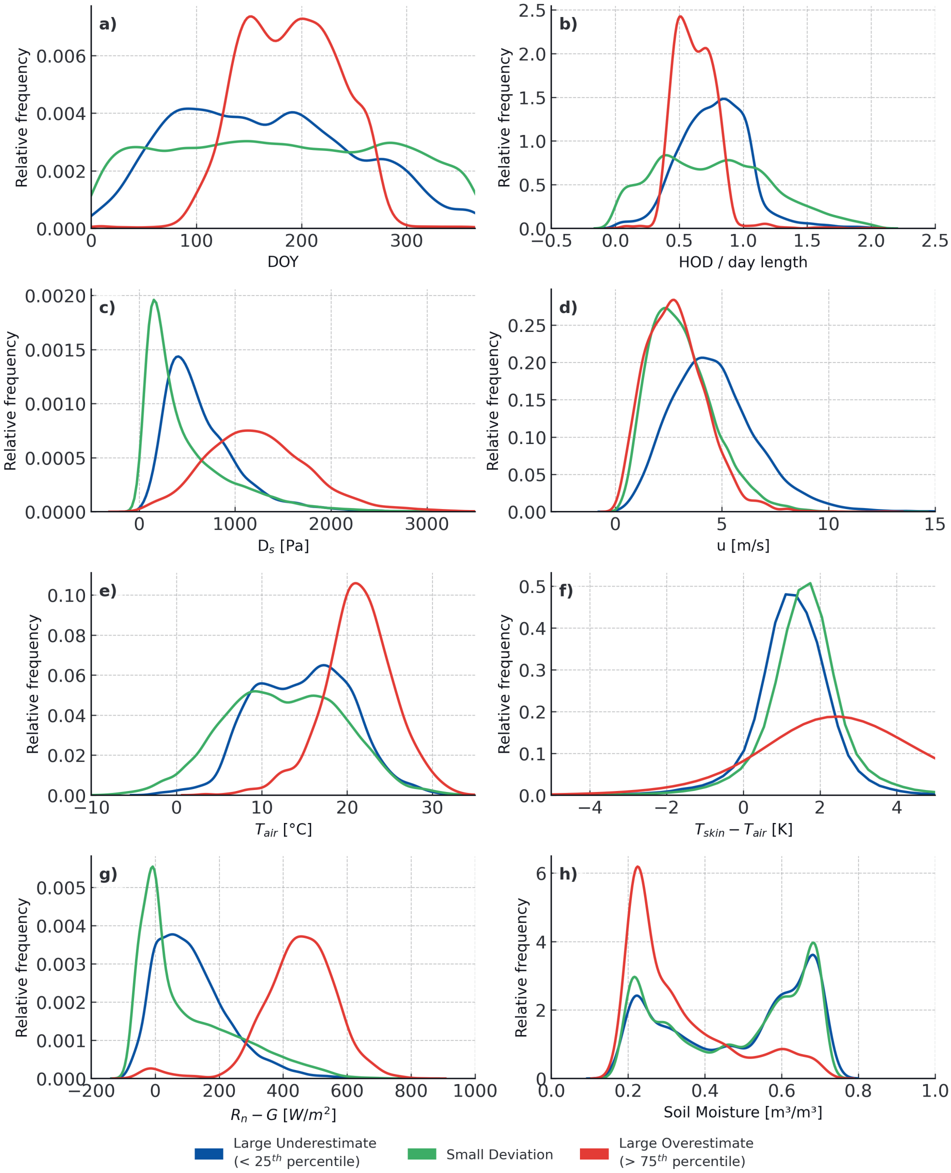

Figure A.5: Relative frequency distributions in relation to timing (DOY, HOD) and six different environmental variables, for 3 categories of error (model - observations) size over grass using A-gs. Large underestimates are those below the 25th percentile of all underestimates, while large overestimates exceed the 75th percentile of all overestimates. Small deviations fall between the 75th percentile of underestimates and the 25th percentile of overestimates.

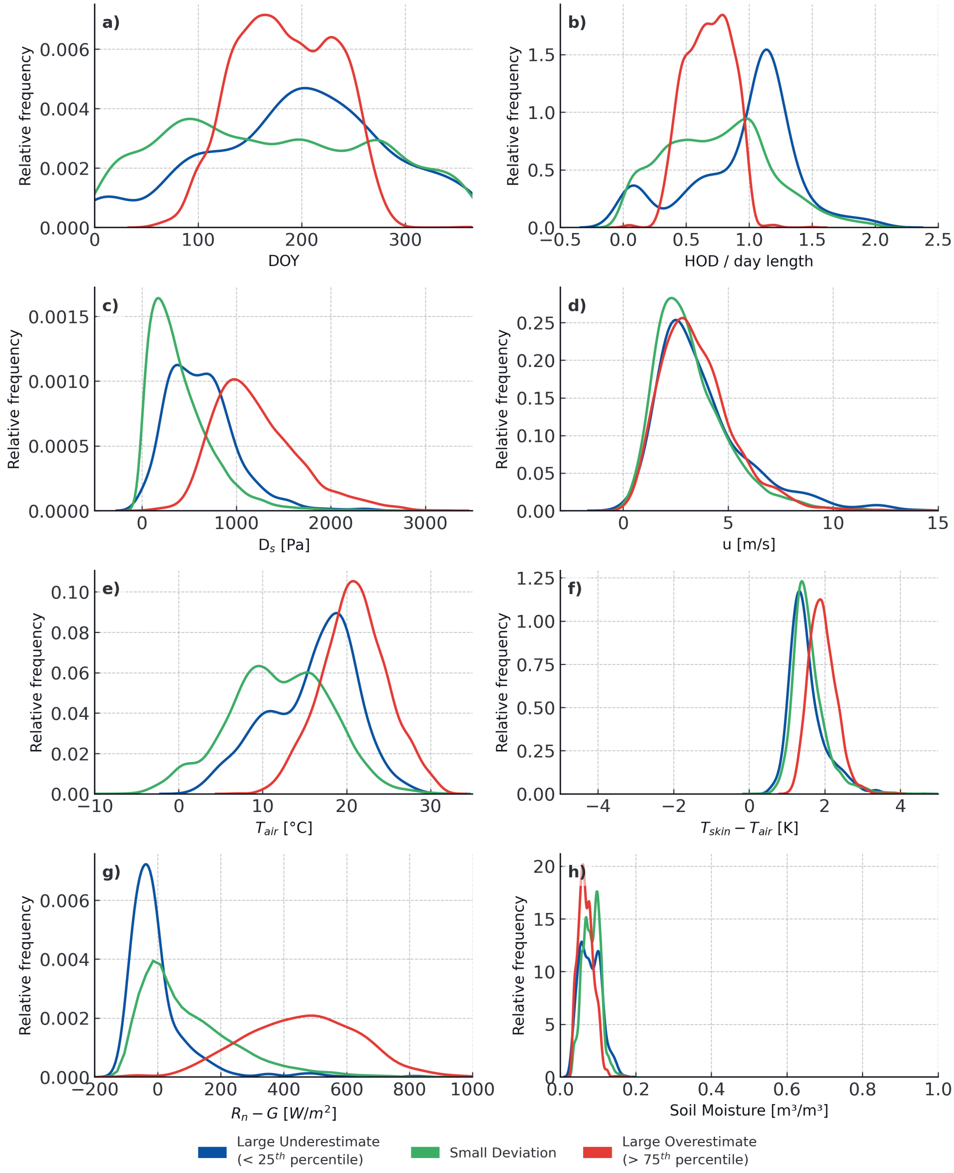

Figure A.6: Relative frequency distributions in relation to timing (DOY, HOD) and six different environmental variables, for 3 categories of error (model - observations) size over forest using Jarvis-Stewart. Large underestimates are those below the 25th percentile of all underestimates, while large overestimates exceed the 75th percentile of all overestimates. Small deviations fall between the 75th percentile of underestimates and the 25th percentile of overestimates.

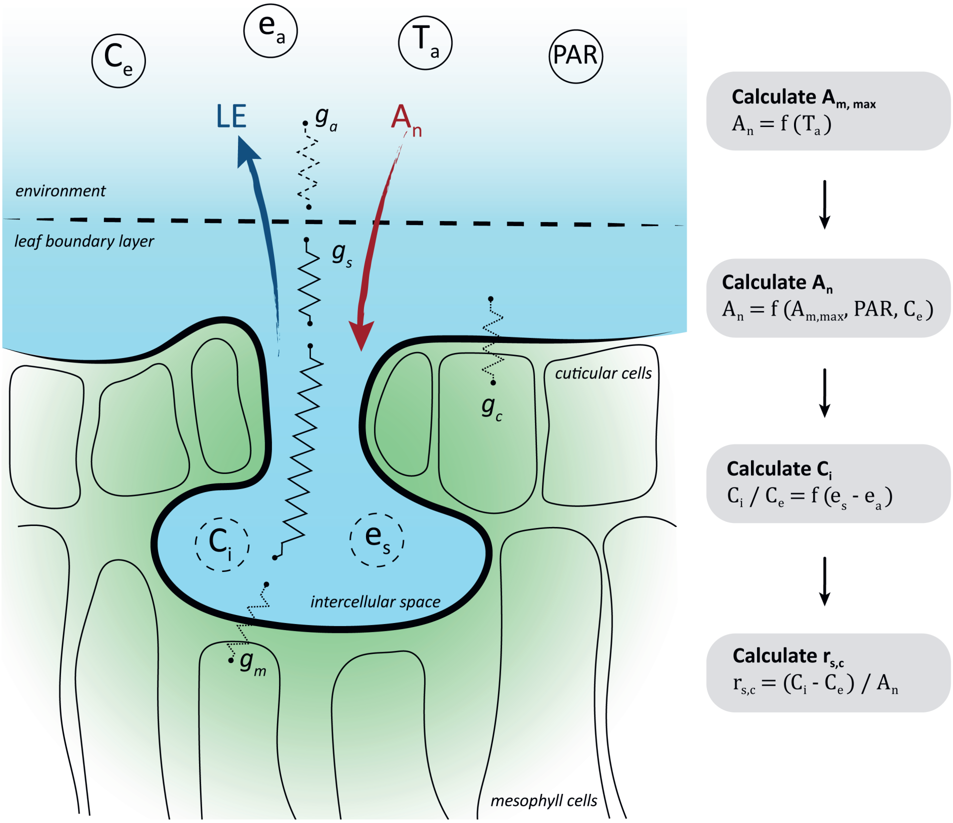

Figure A.7: A scheme showing the A-gs model. Full circled variables have to be measured, while the dotted circled variables are modelled. Note that the stomatal resistance is illustrated as two arrows. This illustrates that the stomatal resistance is actually the sum of the stomatal and leaf boundary layer conductance.

A.3.2. GOUDRIAAN PHOTOSYNTHESIS MODEL

The A-gs model applies the photosynthesis model by Goudriaan (1977). This model derives the stomatal resistance to water vapour from an estimated CO_2 flux. It is visualised in Fig. A.7, and the model parameters can be found in tab. A.2.

The CO_2 flux is influenced by several environmental factors. To estimate it, we first calculate the expected CO_2 flux under optimal conditions, when both CO_2 concentration and light availability are ideal (step 1). Next, we adjust this value to account for the actual environmental conditions, specifically the measured CO_2 concentration and light intensity. This correction provides an estimate of the net assimilation rate (A_n) (step 2).

Stomatal conductance can then be determined using a resistance analogy. It is calculated by dividing the net assimilation rate (A_n) by the difference between the CO_2 concentration inside the leaf and the CO_2 concentration in the surrounding air (step 4). The external CO_2 concentration is directly measured, while the internal CO_2 concentration is expressed as a fraction of the external value (step 3). This fraction depends on the vapour pressure deficit (D_s), which influences the plant's ability to regulate gas exchange.

Step 1: Calculate CO_2 flux under optimal conditions

Under optimal conditions, the maximum assimilation rate $A_{m,max}$ is only temperature dependent.

The maximum assimilation rate is the maximum photosynthetic activity, it is computed as:

$$A_{m,max} = A_{m,max,25} \cdot Q_{10,A_m}^{0.1(T_{surf}-25)} \Big/ \left[(1+e^{0.3(T_{1Am,max}-T_{surf})})(1+e^{0.3(T_{surf}-T_{2Am,max})})\right] \tag{A.34}$$

Here, the compensation point (Γ) is the CO_2 concentration at which A_n becomes zero for a fully lit leaf. It is calculated as:

$$\Gamma = \Gamma_{25} \cdot Q_{10,\Gamma}^{0.1(T_{surf}-25)}. \tag{A.35}$$

Step 2: Estimate the actual CO_2 flux based on radiation and CO_2

In low radiation conditions, the net assimilation is controlled by the amount of photosynthetically active radiation. When radiation intensifies, net assimilation saturates at level A_m that is CO_2 dependent.

This assimilation rate (A_m) is computed as:

$$A_m = A_{m,max}\left(1 - e^{-g_m \frac{C_i - \Gamma}{A_{m,max}}}\right) \tag{A.36}$$

The mesophyll conductance (g_m) describes the conductivity from the stomatal cavity to the mesophyll cells, where the carbon fixation happens. It is given by:

$$g_m = g_{m25} \cdot Q_{10,g_m}^{0.1(T_{surf}-25)} \Big/ \left[(1+e^{0.3(T_{1gm}-T_{surf})})(1+e^{0.3(T_{surf}-T_{2gm})})\right]. \tag{A.37}$$

The radiation and CO_2 response are described by a smooth exponential for the net assimilation (A_n):

$$A_n = (A_m + R_d)\left(1 - e^{-\varepsilon \frac{PAR}{A_m + R_d}}\right) - R_d \tag{A.38}$$

where R_d is the dark respiration ($R_d = A_m/9$) and with the quantum efficiency (ε) is computed as:

$$\varepsilon = \varepsilon_0 \frac{C_i - \Gamma}{C_i + 2\Gamma}. \tag{A.39}$$

Step 3: Estimate internal CO_2 concentrations based on D_s

The CO_2 concentration (C_i) inside the stomatal cavity is calculated using a coupling factor (f) and atmospheric CO_2 concentration (C_s):

$$C_i = fC_s + (1-f)\frac{\Gamma}{C_s} \tag{A.40}$$

here f depends on the vapour pressure deficit D_s through:

$$f = f_0\left(1 - \frac{D_s}{D_{max}}\right) + f_{min}\frac{D_s}{D_{max}}. \tag{A.41}$$

The minimum coupling factor depends on the cuticular and mesophyll conductances, and is species-dependent:

$f_{min} = g_c/(g_c + g_m)$.

STEP 4: DERIVING STOMATAL RESISTANCE FROM THE FLUX

The stomatal resistance for CO_2 (g_{sC}) can then be calculated through a resistance analogy as:

$$r_{sC} + r_a = \frac{C_s - C_i}{A_n}. \tag{A.42}$$

This can be translated to the stomatal resistance for H_2O by correcting for the molecular weight.

$$r_{sH_2O} = r_{sC}/1.6 \tag{A.43}$$

Variable / Parameter	Description	Unit	Short Grass	Evergreen Needleleaf
C_i	Internal CO_2 concentration	ppm	-	-
C_s	Atmospheric CO_2 concentration	ppm	-	-
f	Coupling factor	-	-	-
f_0	Initial coupling factor	-	0.65	-
f_{min}	Minimum coupling factor	-	-	-
D_s	Vapour pressure deficit (VPD)	Pa	-	-
D_{max}	Maximum vapour pressure deficit	kg kg^{-1}	-	0.124
g_m	Mesophyll conductance	mm s^{-1}	-	-
A_n	Net assimilation rate	mg m^{-2} s^{-1}	-	-
A_m	Assimilation rate	mg m^{-2} s^{-1}	-	-
$A_{m,max}$	Maximum assimilation rate	mg m^{-2} s^{-1}	-	-
$A_{m,max,25}$	Max assimilation rate at 25°C	mg m^{-2} s^{-1}	3	2.2
R_d	Dark respiration rate	mg m^{-2} s^{-1}	-	-
ε	Quantum yield efficiency	mg CO$_2$ / J PAR	-	-
ε_0	Reference quantum yield efficiency	mg CO$_2$ / J PAR	0.0142	-
PAR	Photosynthetically active radiation	W m^2	-	-
Γ	Compensation point	ppm	-	-
Γ_{25}	Compensation point at 25°C	ppm	42	42
T_{surf}	Surface temperature	°C	-	-
$T_{1Am,max}$	Lower temperature limit for A_m	°C	8	8
$T_{2Am,max}$	Upper temperature limit for A_m	°C	38	38
T_{1gm}	Lower temperature limit for g_m	°C	5	5
T_{2gm}	Upper temperature limit for g_m	°C	36	36
Q_{10,A_m}	Temp. sensitivity coefficient for A_m	-	2	2
$Q_{10,\Gamma}$	Temp. sensitivity coefficient for Γ	-	2	2
Q_{10,g_m}	Temp. sensitivity coefficient for g_m	-	2	2
g_{m25}	Mesophyll conductance at 25°C	mm s^{-1}	1.3	0.8
g_c	Cuticular conductance	mm s^{-1}	0.2	0.2
g_{sC}	Stomatal conductance for CO_2	mm s^{-1}	-	-
g_{sH_2O}	Stomatal conductance for H_2O	mm s^{-1}	-	-
r_{sH_2O}	Stomatal resistance to H_2O	s m^{-1}	-	-
R_0	Reference respiration rate	mgCO$_2$m^{-2} s^{-1}	0.080	0.360

Table A.2: Gas exchange variables and model parameters for short grass and evergreen needleleaf vegetation types.

BIBLIOGRAPHY

Hopkins, W. G., Hüner, N. P., et al. (1995). *Introduction to plant physiology*. Wiley New York.

Jarvis, P. G. (1976). The interpretation of the variations in leaf water potential and stomatal conductance found in canopies in the field. *Philosophical Transactions of the Royal Society of London. B, Biological Sciences*, *273*(927), 593–610.

Stewart, J. B. (1988). Modelling surface conductance of pine forest. *Agricultural and Forest meteorology*, *43*(1), 19–35.

Van Heerwaarden, C. C., & Teuling, A. J. (2014). Disentangling the response of forest and grassland energy exchange to heatwaves under idealized land–atmosphere coupling. *Biogeosciences*, *11*(21), 6159–6171.

Snyder, R. L., & De Melo-abreu, J. (2005). *Protection: fundamentals, practice and economics*. FAO.

Prasad, P. V., Bheemanahalli, R., & Jagadish, S. V. K. (2017). Field crops and the fear of heat stress—opportunities, challenges and future directions. *Field Crops Research*, *200*, 114–121.

Djalovic, I., Kundu, S., Bahuguna, R. N., Pareek, A., Raza, A., Singla-Pareek, S. L., Prasad, P. V., & Varshney, R. K. (2024). Maize and heat stress: Physiological, genetic, and molecular insights. *The Plant Genome*, *17*(1), e20378.

Châtelet, É. (1740). *Institutions de physique*. Paris.

Fara, P. (2011). *International women's day: Émilie du châtelet*. Retrieved April 30, 2025, from www.blog.oup.com/2011/03/chatelet/#:~:text=%C3%89milie%20du%20Ch%C3%A2telet%2C%20wrote%20Voltaire,and%20freedom%20that%20she%20craved.

Lavoisier, A. L. (1789). *Traite elementaire de chimie*. Paris.

Wallis, J. (1670). *Mechanica: Sive, de motu, tractatus gemetricus*. London.

Ohm, G. S. (1827). *Die galvanische kette: Mathematisch*. TH Riemann.

Monin, A. S., & Obukov, A. M. (1954). Basic laws of turbulent mixing in the surface layer of the atmosphere. *Tr. Akad. Nauk SSSR Geophiz. Inst.*, *24*, 163–187.

Monteith, J. L., & Unsworth, M. (1990). *Principles of environmental physics: Plants, animals, and the atmosphere*. Academic Press. https://doi.org/https://doi.org/10.1016/C2010-0-66393-0

Stull, R. B. (2012). *An introduction to boundary layer meteorology* (Vol. 13). Springer Science & Business Media.

Jacobs, A. F. G., Heusinkveld, B. G., & Holtslag, A. A. (2008). Towards closing the surface energy budget of a mid-latitude grassland. *Boundary-Layer Meteorology*, *126*, 125–136.

Rotach, M. W., & Holtslag, A. A. M. (2025). *Ideal and real atmospheric boundary layers*. Academic Press.

Foken, T. (2006). 50 years of the monin–obukhov similarity theory. *Boundary-Layer Meteorology, 119*, 431–447.

American Meteorological Society. (1959). *Glossary of meteorology*. Retrieved April 30, 2025, from www.glossary.ametsoc.org/wiki/Welcome

Dyer, A. J. (1974). A review of flux-profile relationships. *Boundary-Layer Meteorology, 7*, 363–372.

Moene, A., & van Dam, J. C. (2014). *Transport in the Atmosphere-Vegetation-Soil Continuum*. Cambridge University Press.

Penman, H. L. (1948). Natural evaporation from open water, bare soil and grass. *Proceedings of the Royal Society of London. Series A. Mathematical and Physical Sciences, 193*(1032), 120–145.

Monteith, J. L. (1965). Evaporation and environment. *Symposia of the society for experimental biology, 19*, 205–234.

Jongen, H. J., Vulova, S., Meier, F., Steeneveld, G.-J., Jansen, F., Tetzlaff, D., Kleinschmit, B., Haacke, N., & Teuling, A. (2024). Attributing urban evapotranspiration from eddy-covariance to surface cover: Bottom-up versus top-down. *Water Resources Research, 60*(9), e2024WR037508.

Rannik, Ü., Sogachev, A., Foken, T., Göckede, M., Kljun, N., Leclerc, M., & Vesala, T. (2012). The eddy covariance method: A practical guide to measurement and data analysis.

Raupach, M. R., Thom, A. S., & Edwards, I. (1980). A wind-tunnel study of turbulent flow close to regularly arrayed rough surfaces. *Boundary-Layer Meteorology, 18*, 373–397.

Barlow, J., & Coceal, O. (2008). *A review of urban roughness sublayer turbulence* (tech. rep.). Met Office.

Harman, I. N., & Finnigan, J. (2007). A simple unified theory for flow in the canopy and roughness sublayer. *Boundary-Layer Meteorology, 123*, 339–363.

Harman, I. N., & Finnigan, J. (2008). Scalar concentration profiles in the canopy and roughness sublayer. *Boundary-Layer Meteorology, 129*, 323–351.

World Meteorological Organization. (2023). *Guide to instruments and methods of observation*. Geneva.

Thomas, C. K., Kennedy, A. M., Selker, J. S., Moretti, A., Schroth, M. H., Smoot, A. R., Tufillaro, N. B., & Zeeman, M. J. (2012a). High-resolution fibre-optic temperature sensing: A new tool to study the two-dimensional structure of atmospheric surface-layer flow. *Boundary-Layer Meteorology, 142*, 177–192.

Hartog, A. H. (2017). *An introduction to distributed optical fibre sensors*. CRC press.

Bolognini, G., & Hartog, A. H. (2013). Raman-based fibre sensors: Trends and applications. *Optical Fiber Technology, 19*(6), 678–688.

Raman, C. V. (1928). A new radiation. *Indian Journal of physics, 2*, 387–398.

Dai, Y., Boekee, J., Schilperoort, B., ten Veldhuis, M.-C., & Van de Wiel, B. J. H. (2023). Wind machines for frost damage mitigation: A quantitative 3d investigation based on observations. *Agricultural and Forest Meteorology, 338*, 109522.

Sigmund, A., Pfister, L., Sayde, C., & Thomas, C. K. (2017). Quantitative analysis of the radiation error for aerial coiled-fiber-optic distributed temperature sensing deployments using reinforcing fabric as support structure. *Atmospheric Measurement Techniques*, *10*(6), 2149–2162.

Zeller, M. L., Huss, J. M., Pfister, L., Lapo, K. E., Littmann, D., Schneider, J., Schulz, A., & Thomas, C. K. (2021). The ny-Ålesund turbulence fiber optic experiment (nytefox): Investigating the arctic boundary layer, svalbard. *Earth System Science Data*, *13*(7), 3439–3452.

International Organisation of Vine and Wine. (2021). 2021 Wine production - Press Release. https://www.oiv.int/

Dupont, S., & Patton, E. G. (2012). Influence of stability and seasonal canopy changes on micrometeorology within and above an orchard canopy: The CHATS experiment. *Agricultural and Forest Meteorology, 157*.

Kalma, J., Laughlin, G., Caprio, J., & Hamer, P. (2012). *The bioclimatology of frost: its occurrence, impact and protection*. Springer.

Barlow, K. M., Christy, B. P., O'Leary, G. J., Riffkin, P. A., & Nuttall, J. G. (2015). Simulating the impact of extreme heat and frost events on wheat crop production: A review. *Field Crops Research, 171*.

Perry, K. B. (1998). Basics of frost and freeze protection for horticultural crops. *HortTechnology, 8*, 10–15.

Atam, E., Hong, S. W., & Arteconi, A. (2020). Thermofluid modelling of large-scale orchards for optimal design and control of active frost prevention systems. *Energies*, *13*(2).

Heusinkveld, V. W., Antoon van Hooft, J., Schilperoort, B., Baas, P., Veldhuis, M. c. t., & van de Wiel, B. J. (2020). Towards a physics-based understanding of fruit frost protection using wind machines. *Agricultural and Forest Meteorology, 282-283*.

Ghaemi, A. A., Rafiee, M. R., & Sepaskhah, A. R. (2009). Tree-Temperature Monitoring for Frost Protection of Orchards in Semi-Arid Regions Using Sprinkler Irrigation. *Agricultural Sciences in China*, *8*(1), 98–107.

Anconelli, S., Facini, O., Marletto, V., Pitacco, A., Rossi, F., & Zinoni, F. (2002). Micrometeorological test of microsprinklers for frost protection of fruit orchards in Northern Italy. *Physics and Chemistry of the Earth, Parts A/B/C, 27*(23-24), 1103–1101.

O'connell, N. V., & Snyder, R. L. (1999). Cover crops, mulch lower night temperatures in citrus. *California Agriculture*, *53*(5), 37–40.

Donaldson, D. R., Snyder, R. L., Elmore, C., & Gallagher, S. (1993). Weed Control Influences Vineyard Minimum Temperatures. *American Journal of Enology and Viticulture*.

Ribeiro, A., Melo-Abreu, J., Gonalves, D. A., & Snyder, R. L. (2002). Temperature response to the onset of wind machine operation. *Proceedings of the VII Congress of the European Society for Agronomy*, 317–318.

Leyden, R. F., & Rohrbaugh, P. W. (1963). Protection of citrus trees from cold damage. *Proc. Amer. Soc. Hort. Sci.*

Ribeiro, A. C., De Melo-Abreu, J. P., & Snyder, R. L. (2006). Apple orchard frost protection with wind machine operation. *Agricultural and Forest Meteorology, 141*(2-4), 71–81.

Battany, M. C. (2012). Vineyard frost protection with upward-blowing wind machines. *Agricultural and Forest Meteorology, 157*, 39–48.

Kimura, K., Yasutake, D., Nakazono, K., & Kitano, M. (2017). Dynamic distribution of thermal effects of an oscillating frost protective fan in a tea field. *Biosystems Engineering*, *164*, 98–109.

Quamme, H. A. (1978). Mechanism of supercooling in overwintering peach flower buds. *Journal of the American Society for Horticultural Science*, *103*.

Ashworth, E., Davis, G. A., & Wisniewski, M. E. (1989). The formation and distribution of ice within dormant and deacclimated peach flower buds. *Plant, Cell & Environment*, *12*.

Landsberg, J., Butler, D., & Thorpe, M. (1974). Apple bud and blossom temperatures. *Journal of Horticultural Science*, *49*, 227–239.

Leuning, R., & Cremer, K. (1988). Leaf temperatures during radiation frost part i: Observations. *Agricultural and Forest Meteorology*, *42*, 121–133.

Beyá-Marshall, V., Herrera, J., Santibáñez, F., & Fichet, T. (2019). Micro-climate modification under the effect of stationary and portable wind machines. *Agricultural and Forest Meteorology*, *269*, 351–363.

Thomas, C. K., Kennedy, A. M., Selker, J. S., Moretti, A., Schroth, M. H., Smoot, A. R., Tufillaro, N. B., & Zeeman, M. J. (2012b). High-resolution fibre-optic temperature sensing: A new tool to study the two-dimensional structure of atmospheric surface-layer flow. *Boundary-Layer Meteorology*, *142*, 177–192.

Hamer, P. (1985). The heat balance of apple buds and blossoms. part i: Heat transfer in the outdoor environment. *Agricultural and Forest Meteorology*, *35*, 339–352.

Hamer, P. (1986). The heat balance of apple buds and blossoms. part ii: The water requirements for frost protection by overhead sprinkler irrigation. *Agricultural and Forest Meteorology*, *37*, 159–174.

Leuning, R. (1988). Leaf temperatures during radiation frost part ii: A steady-state theory. *Agricultural and Forest Meteorology*, *42*, 135–155.

Watson, I., & Johnson, G. (1987). Graphical estimation of sky view-factors in urban environments. *International Journal of Climatology*, *7*, 193–197.

Raschke, K. (1960). Heat transfer between the plant and the environment. *Annual Review of Plant Physiology*, *11*, 111–126.

Schuepp, P. (1993). Tansley review no. 59: Leaf boundary layers. *New Phytologist*, 477–507.

Roth-Nebelsick, A. (2001). Computer-based analysis of steady-state and transient heat transfer of small-sized leaves by free and mixed convection. *Plant, Cell & Environment*, *24*, 631–640.

Bailey, B., & Meneses, J. (1995). Modelling leaf convective heat transfer. *ISHS Acta Horticulturae*, *399*, 191–198.

Parkhurst, D., Duncan, P., Gates, D., & Kreith, F. (1968). Wind-tunnel modelling of convection of heat between air and broad leaves of plants. *Agricultural Meteorology*, *5*, 33–47.

Van Der Linden, S. J. A., Kruis, M. T., Hartogensis, O. K., Moene, A. F., Bosveld, F. C., & Van de Wiel, B. J. (2022). Heat transfer through grass: A diffusive approach. *Boundary-Layer Meteorology*, *184*(2), 251–276.

Patton, E. G., Horst, T. W., Sullivan, P. P., Lenschow, D. H., Oncley, S. P., Brown, W. O., Burns, S. P., Guenther, A. B., Held, A., & Karl, T. (2011). The canopy horizontal array turbulence study. *Bulletin of the American Meteorological Society*, *92*, 593–611.

Freundorfer, A., Lapo, K., Schneider, J., & Thomas, C. K. (2021). Distributed sensing of wind direction using fiber-optic cables. *Journal of Atmospheric and Oceanic Technology*, *38*, 1871–1883.

Alveringh, D., Bijsterveld, D. G., van den Berg, T. E., Veltkamp, H.-W., Batenburg, K. M., Sanders, R. G., Lötters, J. C., & Wiegerink, R. J. (2022). A miniature microclimate thermal flow sensor for horticultural applications. *2022 IEEE Sensors*, 1–4.

Charrier, G., Ngao, J., Saudreau, M., & Améglio, T. (2015). Effects of environmental factors and management practices on microclimate, winter physiology, and frost resistance in trees. *Frontiers in Plant Science*, *6*, 259.

Wahid, A., Gelani, S., Ashraf, M., & Foolad, M. R. (2007). Heat tolerance in plants: An overview. *Environmental and experimental botany*, *61*(3), 199–223.

Raison, J. K., Berry, J. A., Armond, P. A., & Pike, C. S. (1980). *Membrane properties in relation to the adaptation of plants to temperature stress*. Wiley.

Aryal, B., & Neuner, G. (2010). Leaf wettability decreases along an extreme altitudinal gradient. *Oecologia*, *162*, 1–9.

Wisniewski, M., Fuller, M., Glenn, D. M., Gusta, L., Duman, J., & Griffith, M. (2002). *Extrinsic ice nucleation in plants*. Springer.

Fuller, M. P., Hamed, F., Wisniewski, M., & Glenn, D. M. (2003). Protection of plants from frost using hydrophobic particle film and acrylic polymer. *Annals of applied biology*, *143*(1), 93–98.

Wisniewski, M., Gusta, L., & Neuner, G. (2014). Adaptive mechanisms of freeze avoidance in plants: A brief update. *Environmental and Experimental Botany*, *99*, 133–140.

Ashworth, E. N., & Kieft, T. L. (1992). Measurement of ice nucleation in lichens using thermal analysis. *Cryobiology*, *29*(3), 400–406.

Hewett, E. W., Young, K., Proebsting, E. L., & Mills, H. H. (1978). Modification of critical freezing temperatures in fruit buds by elevated tissue water content. *HortScience*.

Alden, J., & Hermann, R. K. (1971). Aspects of the cold-hardiness mechanism in plants. *The Botanical Review*, *37*, 37–142.

Khanizadeh, S., Buszard, D., & Zarkadas, C. G. (1992). Effect of crop load on hardiness, protein and amino acids content of apple flower buds at the wintering stage and the begining of the growth. *Journal of Plant Nutrition*, *15*(11), 2441–2455.

Flinn, C. L., & Ashworth, E. N. (1995). The relationship between carbohydrates and flower bud hardiness among three forsythia taxa. *Journal of the American Society for Horticultural Science*.

Rodrigo, J. (2000, August). Spring frosts in deciduous fruit trees. Morphological damage and flower hardiness.

Lu, S., & Rieger, M. (1993). Effect of temperature preconditioning on ovary freezing tolerance of fully opened peach flowers. *Journal of Horticultural Science*, *68*(3).

Proebsting, E. L., & Mills, H. H. (1978). Low temperature resistance of developing flower buds of six deciduous fruit species. *Journal of American Horticultural Society*, (103), 192–198.

Miranda, C., Santesteban, L. G., & Royo, J. B. (2005). Variability in the relationship between frost temperature and injury level for some cultivated Prunus species. *HortScience*, *40*(2), 357–361.

Salazar-Gutiérrez, M. R., Chaves, B., & Hoogenboom, G. (2016). Freezing tolerance of apple flower buds. *Scientia Horticulturae*, *198*, 344–351.

Matzneller, P., Götz, K. P., & Chmielewski, F. M. (2016). Spring frost vulnerability of sweet cherries under controlled conditions. *International Journal of Biometeorology*, *60*(1), 123–130.

Yu, D. J., & Lee, H. J. (2020). Evaluation of freezing injury in temperate fruit trees. *Horticulture, Environment, and Biotechnology*, *61*, 787–794.

Ashworth, E. N., Davis, G. A., & Anderson, J. A. (1985). Factors affecting ice nucleation in plant tissues. *Plant Physiology*, *79*(4), 1033–1037.

Taschler, D., & Neuner, G. (2004). Summer frost resistance and freezing patterns measured in situ in leaves of major alpine plant growth forms in relation to their upper distribution boundary. *Plant, Cell & Environment*, *27*(6), 737–746.

Pearce, R. S., & Fuller, M. P. (2001). Freezing of barley studied by infrared video thermography. *Plant physiology*, *125*(1), 227–240.

Hacker, J., & Neuner, G. (2008). Ice propagation in dehardened alpine plant species studied by infrared differential thermal analysis (idta). *Arctic, Antarctic, and Alpine Research*, *40*(4), 660–670.

Frederiks, T. M., Christopher, J., Harvey, G. L., Sutherland, M. W., & Borrell, A. K. (2012). Current and emerging screening methods to identify post-head-emergence frost adaptation in wheat and barley. *Journal of Experimental Botany*, *63*(15), 5405–5416.

Charrier, G., Nolf, M., Leitinger, G., Charra-Vaskou, K., Losso, A., Tappeiner, U., Améglio, T., & Mayr, S. (2017). Monitoring of freezing dynamics in trees: A simple phase shift causes complexity. *Plant Physiology*, *173*(4), 2196–2207.

Chapman, P., & Catlin, G. (1976). Growth stages in fruit trees-from dormant to fruit set. *New York's Food and Life Sciences Bulletin*.

Physick, W. L., & Garratt, J. R. (1995). Incorporation of a high-roughness lower boundary into a mesoscale model for studies of dry deposition over complex terrain. *Boundary-Layer Meteorology*, *74*(74), 55–71.

Holtslag, A., Svensson, G., Baas, P., Basu, S., Beare, B., Beljaars, A., Bosveld, F., Cuxart, J., Lindvall, J., Steeneveld, G., et al. (2013). Stable atmospheric boundary layers and diurnal cycles: Challenges for weather and climate models. *Bulletin of the American Meteorological Society*, *94*(11), 1691–1706.

Beljaars, A. C. M., & Holtslag, A. A. M. (1991). Flux parameterization over land surfaces for atmospheric models. *Journal of Applied Meteorology*, *30*(3), 327–341.

Duynkerke, P. G. (1992). The roughness length for heat and other vegetation parameters for a surface of short grass. *Journal of Applied Meteorology and Climatology*, *31*(6), 579–586.

Sun, J. (1999). Diurnal variations of thermal roughness height over a grassland. *Boundary-Layer Meteorology*, *92*, 407–427.

Best, M. J., & Hopwood, W. P. (2001). Modelling the local surface exchange over a grass-field site under stable conditions. *Quarterly Journal of the Royal Meteorological Society*, *127*(576), 2033–2052.

Van Driest, E. R. (1956). On turbulent flow near a wall. *Journal of the aeronautical sciences*, *23*(11), 1007–1011.

von Kármán, T. (1930). Mechanische ähnlichkeit und turbulenz. *Nachrichten von der Gesellschaft der Wissenschaften zu Göttingen, Fachgruppe 1 (Mathematik), 5*, 58–76.

Prandtl, L. (1905). Uber flussigkeitsbewegung bei sehr kleiner reibung. *Verhandl. 3rd Int. Math. Kongr. Heidelberg (1904), Leipzig.*

Kundu, P. K., Cohen, I. M., & Dowling, D. R. (2016). *Fluid mechanics* (Vol. 6). Elsevier.

De Ridder, K. (2010). Bulk transfer relations for the roughness sublayer. *Boundary-Layer Meteorology*, *134*, 257–267.

Ryder, J., Polcher, J., Peylin, P., Ottlé, C., Chen, Y., van Gorsel, E., Haverd, V., McGrath, M. J., Naudts, K., & Otto, J. (2016). A multi-layer land surface energy budget model for implicit coupling with global atmospheric simulations. *Geoscientific Model Development*, *9*(1), 223–245.

Chen, Y., Ryder, J., Bastrikov, V., McGrath, M. J., Naudts, K., Otto, J., Ottlé, C., Peylin, P., J. Polcher, J., & Valade, A. (2016). Evaluating the performance of land surface model orchidee-can v1. 0 on water and energy flux estimation with a single-and multi-layer energy budget scheme. *Geoscientific Model Development*, *9*(9), 2951–2972.

Bonan, G. B., Patton, E. G., Harman, I. N., Oleson, K. W., Finnigan, J. J., Lu, Y., & Burakowski, E. A. (2018). Modeling canopy-induced turbulence in the earth system: A unified parameterization of turbulent exchange within plant canopies and the roughness sublayer (clm-ml v0). *Geoscientific Model Development*, *11*(4), 1467–1496.

Thom, A. S. (1971). Momentum absorption by vegetation. *Quarterly Journal of the Royal Meteorological Society*, *97*(414), 414–428.

Viterbo, P., & Beljaars, A. C. (1995). An improved land surface parameterization scheme in the ecmwf model and its validation. *Journal of Climatology*, *8*(11), 2716–2748.

Mitchell, K. (2005). *The community noah land-surface model (lsm) - user's guide*. Version 2.7.1.

Clark, D., Harris, P., Pryor, M., & Hendry, M. (2010). *Joint uk land environment simulator - user's guide*. Version 2.2.

Meier, R., L, D. E., Bonan, G. B., Lawrence, D. M., Hu, X., Duveiller, G., Prigent, C., & Seneviratne, S. I. (2022). Impacts of a revised surface roughness parameterization in the community land model 5.1. *Geoscientific Model Development*, *15*(6), 2365–2393.

Zhang, Y., Narayanappa, D., Ciais, P., Li, W., Goll, D., Vuichard, N., De Kauwe, M. G., Li, L., & Maignan, F. (2022). Evaluating the vegetation–atmosphere coupling strength of orchidee land surface model (v7266). *Geoscientific Model Development*, *15*(24), 9111–9125.

Garratt, J. R., & Hicks, B. B. (1973). Momentum, heat and water vapour transfer to and from natural and artificial surfaces. *Quarterly Journal of the Royal Meteorological Society*, *99*(422), 680–687.

Garratt, J. R., & Francey, R. J. (1978). Bulk characteristics of heat transfer in the unstable, baroclinic atmospheric boundary layer. *Boundary-Layer Meteorology*, *15*, 399–421.

Brutsaert, W. (1982). *Evaporation into the atmosphere: Theory, history and applications*. Springer.

Andreas, E. L. (1987). A theory for the scalar roughness and the scalar transfer coefficients over snow and sea ice. *Boundary-Layer Meteorology*, *38*, 159–184.

Blyth, E. M., & Dolman, A. J. (1995). The roughness length for heat of sparse vegetation. *Journal of Applied Meteorology*, 583–585.

Zilitinkevich, S. (1995). Non-local turbulent transport: Pollution dispersion aspects of coherent structure of connective flows. *Transactions on Ecology and the Environment*, *9*, 53–60.

Verhoef, A., De Bruin, H. A. R., & Van Den Hurk, B. J. J. M. (1997). Some practical notes on the parameter kb- 1 for sparse vegetation. *Journal of Applied Meteorology*, *36*(5), 560–572.

Massman, W. J. (1999). A model study of kbh- 1 for vegetated surfaces using 'localized near-field'lagrangian theory. *Journal of Hydrology*, *223*(1-2), 27–43.

Blümel, K. (1999). A simple formula for estimation of the roughness length for heat transfer over partly vegetated surfaces. *Journal of Applied Meteorology*, *38*(6), 814–829.

Chaney, N. W., Herman, J. D., Ek, M. B., & Wood, E. F. (2016). Deriving global parameter estimates for the noah land surface model using fluxnet and machine learning. *Journal of Geophysical Research: Atmospheres*, *121*(22), 13–218.

Rigden, A., Li, D., & Salvucci, G. (2018). Dependence of thermal roughness length on friction velocity across land cover types: A synthesis analysis using ameriflux data. *Agricultural and Forest Meteorology*, *249*, 512–519.

Garratt, J. R., Hicks, B. B., & Valigura, R. A. (1993). Comments on" the roughness length for heat and other vegetation parameters for a surface of short grass. *Journal of Applied Meteorology*, *32*(7), 1301–1303.

Su, Z., Schmugge, T., Kustas, W. P., & Massman, W. J. (2001). An evaluation of two models for estimation of the roughness height for heat transfer between the land surface and the atmosphere. *Journal of Applied Meteorology and Climatology*, *40*(11), 1933–1951.

Hicks, B. B., & Eash, N. S. (2021). On the effective surface temperature of a natural landscape: Infrared or not infrared. *Boundary-Layer Meteorology*, *180*(2), 353–362.

Monin, A. S., & Yaglom, A. M. (1973). *Statistical fluid mechanics, volume i: Mechanics of turbulence* (Vol. 1). The MIT press.

Donda, J. M. M., Van Hooijdonk, I. G. S., Moene, A. F., Jonker, H. J. J., van Heijst, G. J. F., Clercx, H. J. H., & van de Wiel, B. J. H. (2014). Collapse of turbulence in stably stratified channel flow: A transient phenomenon. *Quarterly Journal of the Royal Meteorological Society*, *141*(691), 2137–2147.

Raupach, M. R., Finnigan, J. J., & Brunet, Y. (1996). Coherent eddies and turbulence in vegetation canopies: The mixing-layer analogy. *Boundary-Layer Meteorology 25th Anniversary Volume, 1970–1995: Invited Reviews and Selected Contributions to Recognise Ted Munn's Contribution as Editor over the Past 25 Years*, 351–382.

Selker, J., van de Giesen, N., Westhoff, M., Luxemburg, W., & Parlange, M. B. (2006). Fiber optics opens window on stream dynamics. *Geophysical Research Letters*, *33*(24).

Tyler, S. W., Selker, J. S., Hausner, M. B., Hatch, C. E., Torgersen, T., Thodal, C. E., & Schladow, S. G. (2009). Environmental temperature sensing using raman spectra dts fiber-optic methods. *Water Resources Research*, *45*(4).

des Tombe, B., Schilperoort, B., & Bakker, M. M. (2020). Estimation of temperature and associated uncertainty from fiber-optic raman-spectrum distributed temperature sensing. *Sensors*, *20*(8), 2235.

Schulte, R. B., van Zanten, M. C., Rutledge-Jonker, S., Swart, D. P. J., Wichink Kruit, R. J., Krol, M. C., van Pul, W. A. J., & Vilà-Guerau de Arellano, J. (2021). Unraveling the diurnal atmospheric ammonia budget of a prototypical convective boundary layer. *Atmospheric Environment*, *249*, 118153.

Shaw, R. H., & Pereira, A. R. (1982). Aerodynamic roughness of a plant canopy: A numerical experiment. *Agricultural Meteorology*, *26*(1), 51–65.

Wieringa, J. (1993). Representative roughness parameters for homogeneous terrain. *Boundary-Layer Meteorology*, *63*, 323–363.

Mahrt, L. (2009). Characteristics of submeso winds in the stable boundary layer. *Boundary-layer Meteorology*, *130*, 1–14.

Edwards, J. M. (2009). Radiative processes in the stable boundary layer: Part i. radiative aspects. *Boundary-Layer Meteorology*, *131*, 105–126.

Högström, U. L. F. (1996). Review of some basic characteristics of the atmospheric surface layer. *Boundary-Layer Meteorology*, *78*, 215–246.

Raupach, M. R. (1992). Drag and drag partition on rough surfaces. *Boundary-Layer Meteorology*, *60*(4), 375–395.

Jacobs, A. F. G., & Verhoef, A. (1997). Soil evaporation from sparse natural vegetation estimated from sherwood numbers. *Journal of Hydrology*, *188*, 443–452.

Verhoef, A., McNaughton, K. G., & Jacobs, A. F. G. (1997). A parameterization of momentum roughness length and displacement height for a wide range of canopy densities. *Hydrology and Earth System Sciences*, *1*(1), 81–91.

Högström, U., Bergström, H., Smedman, A. S., & Halldinand, A., S Lindroth. (1989). Turbulent exchange above a pine forest, i: Fluxes and gradients. *Boundary-Layer Meteorology*, *49*, 197–217.

LeMone, M. A., Angevine, W. M., Bretherton, C. S., Chen, F., Dudhia, J., Fedorovichi, E., Katsaros, K. B., Lenschow, D. H., Mahrt, L., Patton, E. G., Sun, J., Tjernström, M., & Weil, J. (2019). 100 years of progress in boundary layer meteorology. *Meteorological Monographs*, *59*, 9–1.

Cellier, P., & Brunet, Y. (1992). Flux-gradient relationships above tall plant canopies. *Agricultural and Forest Meteorology*, *58*(1-2), 93–117.

Graefe, J. (2004). Roughness layer corrections with emphasis on svat model applications. *Agricultural and Forest Meteorology*, *124*(3-4), 237–251.

Brunet, Y. (2020). Turbulent flow in plant canopies: Historical perspective and overview. *Boundary-Layer Meteorology*, *177*(2-3), 315–364.

Sauerbier, J. (2024). *Direct numerical simulations of the atmosphere-grass boundary layer* [Master's thesis, Delft University of Technology].

Brutsaert, W. (1975). A theory for local evaporation (or heat transfer) from rough and smooth surfaces at ground level. *Water Resources Research*, *11*(4), 543–550.

Grass, A. J. (1971). Structural features of turbulent flow over smooth and rough boundaries. *Journal of Fluid Mechanics*, *50*(2), 233–255.

Henderson-Sellers, A., McGuffie, K., & Pitman, A. J. (1996). The project for intercomparison of land-surface parametrization schemes (pilps): 1992 to 1995. *Climate Dynamics*, *12*, 849–859.

Chen, T. H., Henderson-Sellers, A., Milly, P. C. D., Pitman, A. J., Beljaars, A. C. M., Polcher, J., Abramopoulos, F., Boone, A., Chang, S., Chen, F., et al. (1997). Cabauw experimental results from the project for intercomparison of land-surface parameterization schemes. *Journal of Climate*, *10*(6), 1194–1215.

Best, M. J., Abramowitz, G., Johnson, H., Pitman, A., Balsamo, G., Boone, A., Cuntz, M., Decharme, B., Dirmeyer, P., Dong, J., et al. (2015). The plumbing of land surface models: Benchmarking model performance. *Journal of Hydrometeorology*, *16*(3), 1425–1442.

Abramowitz, G., Leuning, R., Clark, M., & Pitman, A. (2008). Evaluating the performance of land surface models. *Journal of climate*, *21*(21), 5468–5481.

Dirmeyer, P. A., Koster, R. D., & Guo, Z. (2006). Do global models properly represent the feedback between land and atmosphere? *Journal of Hydrometeorology*, *7*(6), 1177–1198.

Renner, M., Kleidon, A., Clark, M., Nijssen, B., Heidkamp, M., Best, M., & Abramowitz, G. (2021). How well can land-surface models represent the diurnal cycle of turbulent heat fluxes? *Journal of Hydrometeorology*, *22*(1), 77–94.

Wang, Y. P., Kowalczyk, E., Leuning, R., Abramowitz, G., Raupach, M. R., Pak, B., van Gorsel, E., & Luhar, A. (2011). Diagnosing errors in a land surface model (cable) in the time and frequency domains. *Journal of Geophysical Research: Biogeosciences*, *116*(G1).

ECMWF. (2024). Part iv: Physical processes. *IFS Documentation Cycle Cy48r1*.

Boekee, J., van der Linden, S. J., ten Veldhuis, M.-C., Verouden, I. E., Nollen, P. J., Dai, Y., Jongen, H. J., & van de Wiel, B. J. (2024). Rethinking the roughness height: An improved description of temperature profiles over short vegetation. *Boundary-Layer Meteorology*, *190*(7), 31.

Wong, S. C., Canny, M. J., Holloway-Phillips, M., Stuart-Williams, H., Cernusak, L. A., Márquez, D. A., & Farquhar, G. D. (2022). Humidity gradients in the air spaces of leaves. *Nature Plants*, *8*(8), 971–978.

Goudriaan, J. (1977). *Crop micrometeorology: A simulation study*. Wageningen University; Research.

Farquhar, G., & Wong, S. (1984). An empirical model of stomatal conductance. *Functional Plant Biology*, *11*(3), 191–210.

Ball, J. T., Woodrow, I. E., & Berry, J. A. (1987). A model predicting stomatal conductance and its contribution to the control of photosynthesis under different environmental conditions. *Progress in photosynthesis research: volume 4 proceedings of the VIIth international congress on photosynthesis providence, Rhode Island, USA, august 10–15, 1986*, 221–224.

van der Molen, M., Barten, J., Snellen, H., Peters, W., & Vilà-Guerau de Arellano, J. (2024). MAQ-Observations v1.0: Loobos [Last accessed 2025-02-01].

Heusinkveld, B., Barten, J., Fry, J., van der Molen, M., Nursanto, R., Ronda, R., & Snellen, H. (2024). MAQ-Observations v1.0: Veenkampen [Last accessed 2025-02-01].

Damour, G., Simonneau, T., Cochard, H., & Urban, L. (2010). An overview of models of stomatal conductance at the leaf level. *Plant, Cell & Environment*, *33*(9), 1419–1438.

Jones, H. G., & Sutherland, R. (1991). Stomatal control of xylem embolism. *Plant, Cell & Environment*, *14*(6), 607–612.

Gutschick, V., & Simonneau, T. (2002). Modelling stomatal conductanceof field-grown sunflower under varying soil water content and leafenvironment: Comparison of three models of stomatal response toleaf environment and coupling with an abscisic acid-based modelof stomatal response to soil drying. *Plant, Cell & Environment*, *25*(11), 1423–1434.

Buckley, T., Mott, K., & Farquhar, G. (2003). A hydromechanical and biochemical model of stomatal conductance. *Plant, Cell & Environment*, *26*(10), 1767–1785.

Byrne, K. A., Kiely, G., & Leahy, P. (2005). Co2 fluxes in adjacent new and permanent temperate grasslands. *Agricultural and Forest Meteorology*, *135*(1-4), 82–92.

Cisneros Vaca, C., van der Tol, C., & Ghimire, C. P. (2018). The influence of long-term changes in canopy structure on rainfall interception loss: A case study in speulderbos, the netherlands. *Hydrology and Earth System Sciences*, *22*(7), 3701–3719.

Noilhan, J., & Planton, S. (1989). A simple parameterization of land surface processes for meteorological models. *Monthly weather review*, *117*(3), 536–549.

Collatz, G. J., Ball, J. T., Grivet, C., & Berry, J. A. (1991). Physiological and environmental regulation of stomatal conductance, photosynthesis and transpiration: A model that includes a laminar boundary layer. *Agricultural and Forest Meteorology*, *54*(2-4), 107–136.

Ronda, R., De Bruin, H., & Holtslag, A. (2001). Representation of the canopy conductance in modeling the surface energy budget for low vegetation. *Journal of Applied Meteorology and Climatology*, *40*(8), 1431–1444.

Jacobs, C. M. J. (1994). *Direct impact of atmospheric co2 enrichment on regional transpiration*. Wageningen University; Research.

Jacobs, C. M. J., Van den Hurk, B., & De Bruin, H. (1996). Stomatal behaviour and photosynthetic rate of unstressed grapevines in semi-arid conditions. *Agricultural and Forest Meteorology*, *80*(2-4), 111–134.

Robeson, S. M., & Willmott, C. J. (2023). Decomposition of the mean absolute error (mae) into systematic and unsystematic components. *PloS ONE*, *18*(2), e0279774.

Kelliher, F. M., Leuning, R., Raupach, M. R., & Schulze, E.-D. (1995). Maximum conductances for evaporation from global vegetation types. *Agricultural and Forest Meteorology*, *73*(1-2), 1–16.

Twine, T. E., Kustas, W., Norman, J., Cook, D., Houser, P., Meyers, T., Prueger, J., Starks, P., & Wesely, M. (2000). Correcting eddy-covariance flux underestimates over a grassland. *Agricultural and Forest Meteorology*, *103*(3), 279–300.

Hirschi, M., Michel, D., Lehner, I., & Seneviratne, S. I. (2017). A site-level comparison of lysimeter and eddy covariance flux measurements of evapotranspiration. *Hydrology and Earth System Sciences*, *21*(3), 1809–1825.

Hollinger, D., & Richardson, A. (2005). Uncertainty in eddy covariance measurements and its application to physiological models. *Tree Physiology*, *25*(7), 873–885.

Van de Wiel, B., Moene, A., Hartogensis, O., De Bruin, H., & Holtslag, A. (2003). Intermittent turbulence in the stable boundary layer over land. part iii: A classification for observations during cases-99. *Journal of the atmospheric sciences*, *60*(20), 2509–2522.

Heusinkveld, B. G., Jacobs, A. F. G., Holtslag, A. A. M., & Berkowicz, S. M. (2004). Surface energy balance closure in an arid region: Role of soil heat flux. *Agricultural and Forest Meteorology*, *122*(1-2), 21–37.

Lindroth, A., Mölder, M., & Lagergren, F. (2010). Heat storage in forest biomass improves energy balance closure. *Biogeosciences*, *7*(1), 301–313.

Harrison, R. G. (2010). Natural ventilation effects on temperatures within stevenson screens. *Quarterly Journal of the Royal Meteorological Society*, *136*(646), 253–259.

Deardorff, J. W. (1978). Efficient prediction of ground surface temperature and moisture, with inclusion of a layer of vegetation. *Journal of Geophysical Research: Oceans*, *83*(C4), 1889–1903.

Bonan, G. B., Patton, E. G., Finnigan, J. J., Baldocchi, D. D., & Harman, I. N. (2021). Moving beyond the incorrect but useful paradigm: Reevaluating big-leaf and multilayer plant canopies to model biosphere-atmosphere fluxes–a review. *Agricultural and Forest Meteorology*, *306*, 108435.

Ershadi, A., McCabe, M., Evans, J., & Wood, E. F. (2015). Impact of model structure and parameterization on penman–monteith type evaporation models. *Journal of Hydrology*, *525*, 521–535.

Vilà-Guerau de Arellano, J., Ney, P., Hartogensis, O., De Boer, H., Van Diepen, K., Emin, D., De Groot, G., Klosterhalfen, A., Langensiepen, M., Matveeva, M., et al. (2020). Cloudroots: Integration of advanced instrumental techniques and process modelling of sub-hourly and sub-kilometre land–atmosphere interactions. *Biogeosciences*, *17*(17), 4375–4404.

Boekee, J., Dai, Y., Schilperoort, B., Van de Wiel, B. J., & ten Veldhuis, M.-C. (2023). Plant–atmosphere heat exchange during wind machine operation for frost protection. *Agricultural and Forest Meteorology*, *330*, 109312.

González-Armas, R., Vilà-Guerau de Arellano, J., Mangan, M. R., Hartogensis, O., & De Boer, H. (2024). Impact of canopy environmental variables on the diurnal dynamics of water and carbon dioxide exchange at leaf and canopy level. *Biogeosciences*, *21*(10), 2425–2445.

Vos, J., Evers, J. B., Buck-Sorlin, G. H., Andrieu, B., Chelle, M., & De Visser, P. H. (2010). Functional–structural plant modelling: A new versatile tool in crop science. *Journal of experimental Botany*, *61*(8), 2101–2115.

ter Horst, C. G., Vis, G. A., Jongen-Boekee, J., ten Veldhuis, M.-C., Hut, R. W., & van de Wiel, B. J. (2025). An adaptable dts-based parametric method to probe near-surface vertical temperature profiles at millimeter resolution. *EGUsphere*, *2025*, 1–25.

Schilperoort, B., Coenders-Gerrits, M., Luxemburg, W., Jiménez Rodríguez, C., Cisneros Vaca, C., & Savenije, H. (2018). Using distributed temperature sensing for bowen ratio evaporation measurements. *Hydrology and Earth System Sciences*, *22*(1), 819–830.

van Ramshorst, J. G., Coenders-Gerrits, M., Schilperoort, B., van de Wiel, B. J., Izett, J. G., Selker, J. S., Higgins, C. W., Savenije, H. H., & van de Giesen, N. C. (2020).

Revisiting wind speed measurements using actively heated fiber optics: A wind tunnel study. *Atmospheric Measurement Techniques*, *13*(10), 5423–5439.

Kitamura, K., Mitsuishi, A., Suzuki, T., & Kimura, F. (2015). Fluid flow and heat transfer of natural convection adjacent to upward-facing, rectangular plates of arbitrary aspect ratios. *International Journal of Heat and Mass Transfer*, *89*, 320–332.

Graefe, J., Grosch, R., & Bitterlich, M. (2022). The boundary layer conductance of inclined elliptical leaves under free convection. *Agricultural and Forest Meteorology*, *317*, 108884.

Oleson, K. W., Lawrence, D. M., Bonan, G. B., Flanner, M. G., Kluzek, E., Lawrence, P. J., Dai, A., Decker, M., Dickinson, R., Feddema, J., Heald, C. L., Hoffman, F., Lamarque, J. F., Mahowald, N., Niu, G. Y., Qian, T., Randerson, J., Running, S., Sakaguchi, K., … Zeng, X. (2010). *Technical description of version 4.0 of the community land model (clm)* (tech. rep.). NCAR. University Corporation for Atmospheric Research.

ACKNOWLEDGEMENTS

Over the past five years, spring has looked very different for me each year. I have spent it in the freezing cold in Krabbendijke, hunched in a van at midnight together with Dai. I spent it in the burning sun in Wageningen, gluing cables together with Mariska. A year ago I spent it in Geneva, New York, driving a pick-up truck through an apple orchard with Jason. Finally, this year I spent it sipping coffee in Denver with Marie-Claire. My PhD and life have been closely intertwined over the last few years, thanks to the experiences and friends my work has brought me. In these acknowledgements, I therefore want to thank everyone for the last 5 years of my life.

Maybe you have read the whole thesis before you arrived here, or maybe you're more like me and skipped forward to this bit. I can't blame you, we save the best for last. In case you missed it, I invite you to flip back the pages to the quote I use to open my thesis. *Be kind.* I consider myself exceptionally lucky with the kind people who surrounded me throughout my PhD.

First and foremost I want to thank my academic family: Marie-Claire, Bas and Dai. Marie-Claire, wat ben jij een geweldig voorbeeld voor mij. Ik bewonder je kalme, down-to-earth houding en schijnbare ongrijpbaarheid voor stress. De afgelopen jaren heb ik de kans gekregen je steeds beter te leren kennen, vooral tijdens onze reizen naar de VS. Ik hoop dat we nog vaak samen koffie zullen drinken.

Bas, als er iemand wordt omschreven als die enthousiast rondrendende man op mijn bruiloft, dan kan het niet anders dan dat dat over jou gaat. Jouw enthousiasme werkt aanstekelijk, en wat heb ik veel van jou geleerd! Jouw sceptische kijk op bestaande concepten is one-of-a-kind. Ik heb een paar keer een compliment gekregen dat het duidelijk is dat jij mijn supervisor bent, en ik ben daar heel trots op!

Dai, my academic twin! I was, and always will be, so impressed by your skills. My PhD wouldn't have been the same without you. So happy to have someone who was on the project with me to remember all the stupid details I forgot. But over time, you became a friend more than a colleague, and I will forever cherish the memories of our travels together.

A big thanks too for everyone who joined the Fruitfrost family over the years: Iris, Tijn, Sabine, Gijs, Steven, Bart, Inger and Mariska. Work is so much more fun when you do it together.

I thank Bas and Marie-Claire for valuing the importance of travel during a PhD trajectory. I tried my best to spend as much as possible of the seemingly endless travel budget, but somehow there was still some left in the end. So for that reason, this PhD has been written in many places: Delft, Wageningen, Andelst, Geneva and Karlsruhe.

I started my Delft career in COVID times. But, David, Fransje, Bart, Jerom, Monica, Chelsea, Ties, Luuk, Bas en Gijs you made the (home)office a warm place from day one. We got our first chance to bond during the EGU in Vienna, and from that week onwards, I felt I was part of a group in Delft. Later I met Julia, Tessel, Nathalie, Muhammad, and many more. Thanks for making Delft the lively place it is now. Also to the staff, Remko, Miriam, Erik and Arjan thanks for always making a chat in the hallway and your interest in me and my work.

To the people in Geneva: Jason, Hannah, Phil, Davis, Jane and Tori. Thank you hosting me and for showing me that Americans are the nicest people. Geneva will always have a warm spot in my heart.

To the people in Wageningen. Thank you for always welcoming me back, even though you had no reason to. For proving that a Wageninger always comes back to Wageningen (or in my case, never really leaves).

A big thank you to all my friends, but especially Eveline, Sam, Roosmarijn and Fabio. Eveline, where would I be without you by my side. Thank you for listening to me complain and hype about everything in life. Sam, thanks for sharing your love for plants and academia with me. Roosmarijn and Fabio, thank you for all the dinners you cooked me when I tried to escape the rush hour. You made the commuting to Delft so much more enjoyable!

Kim and Christoph, thank you for sharing the highs and lows of life with Harro and me. Whether that meant sweatpants and binge-watching with take-out on Friday night, or getting dressed up for a wedding or two. Kim, my academic journey would be woefully incomplete without you by my side. Even though we started our PhDs at different universities, it still feels the same as all those computer practicals we did together during our bachelor's and master's. Christoph, thank you for keeping up with all our complaints and gossip about academia. Even though we don't often talk one-on-one (apart from the yearly happy birthday texts), I love our instant philosophical conversations when we do. I know you both will always be there for me, and I will always be there for you.

To my parents, thank you for believing in me, without expecting me to. You always found a perfect balance in support. To my extended family, thank you for showing me the value of tradition and what it's like to have brothers (and a dog).

Harro, als jij me niet had aangemoedigd was ik nooit aan deze PhD begonnen. Zoveel avonturen en uitdagingen die ik gaandeweg ben aangegaan, had ik zonder jouw duwtjes in de rug niet gedurfd. De afgelopen 5 jaar hadden er compleet anders uitgezien. In de eenzame tijden van COVID was jij mijn kantoorgenoot. Als ik na een lange autorit vol files thuis kwam uit Delft, zorgde jij ervoor dat er eten op tafel stond. En toen ik besloot naar de VS te willen reizen, zat jij naast me in het vliegtuig. Als ik even geen vertrouwen meer had in mijn eigen werk, las je het voor me door en stak me niet alleen een hart onder de riem, maar gaf ook kritische feedback. Dankjewel voor het vasthouden van mijn hand en het duwtje in de rug dat je me hebt gegeven tijdens dit avontuur.

CURRICULUM VITÆ

Judith JONGEN - BOEKEE

27-03-1997	Born in Roosendaal, The Netherlands.

EDUCATION

2018 – 2020	Master of Science Earth & Environment Wageningen University and Research *Cum Laude*
2015 – 2018	Bachelor of Science Soil, Water, Atmosphere Wageningen University and Research *Cum Laude*
2009 – 2015	High School Mollerlyceum, Bergen op Zoom *Cum Laude*

Experience

2025 →	Researcher Surface Observations Royal Netherlands Meteorological Institute (KNMI), De Bilt
2024 →	Freelance scientific illustrator
2024	Visiting Researcher Cornell AgriTech, Geneva (USA)
2020 – 2025	PhD Candidate Delft University of Technology, Delft
2020	Research Intern Geophysical Institute, University of Bergen, Bergen (Norway)
2018 – 2020	Forecasting assistant DTN, Wageningen

Awards

2025	AMS 25th BLT symposium: best student presentation 3rd place
2025	AMS Denver Summit: best student presentation 1st place
2025	BBOS presentation award public and jury vote
2021	DeepWind’2021 digital conference poster award

LIST OF PUBLICATIONS

FIRST AUTHOR PUBLICATIONS

3. **Jongen-Boekee, J.**, van de Wiel, B. J. & ten Veldhuis, M. C., Diagnosing LE: when Penman-Monteith and eddy-covariance disagree. Quarterly Journal of the Royal Meteorological Society *(In Preparation)*

2. **Boekee, J.**, van der Linden, S. J., ten Veldhuis, M. C., Verouden, I. E., Nollen, P. J., Dai, Y., Jongen, H. J., & van de Wiel, B. J. (2024). Rethinking the Roughness Height: An Improved Description of Temperature Profiles over Short Vegetation. Boundary-Layer Meteorology, 190(7), 31.

1. **Boekee, J.**, Dai, Y., Schilperoort, B., Van de Wiel, B. J., & ten Veldhuis, M. C. (2023). Plant–atmosphere heat exchange during wind machine operation for frost protection. Agricultural and Forest Meteorology, 330, 109312.

CO-AUTHOR PUBLICATIONS

6. Heim, R. H. J., Prikaziuk, E., Schlerf, M., Gerhards, M., van der Tol, C., Slippers, B., Gold, K., **Jongen-Boekee, J.**, ten Veldhuis, M., Kaiser, E., Saeys, W., Jacobs, A., van der Ploeg, M., Kramer, D., Kappas, M., Graß, R., Hammond, W., van den Berg, T., Agri-SenseNet – A concept for a European stress detection network using a closed sensor feedback loop and differential diagnosis. New Phytologist *(In Preparation)*

5. ter Horst, C. G., Vis, G. A., **Jongen-Boekee, J.**, ten Veldhuis, M. C., Hut, R. W., & van de Wiel, B. J. (2025). An Adaptable DTS-based Parametric Method to Probe Near-surface Vertical Temperature Profiles at Millimeter Resolution. EGUsphere, 2025, 1-25.

4. Arheimer, B., Cudennec, C., Castellarin, A., Grimaldi, S., Heal, K. V., Lupton, C., **Boekee, J.**, ... & Xia, J. (2024). The IAHS Science for Solutions decade, with Hydrology Engaging Local People IN one Global world (HELPING). Hydrological Sciences Journal, 69(11), 1417-1435.

3. Dai, Y., van Hooft, A., Patton, E. G., **Boekee, J.**, van der Linden, S., ten Veldhuis, M. C., & van de Wiel, B. J. (2024). Integrated large-eddy simulation for modeling plant-tissue warming induced by wind machines in an orchard canopy. Agricultural and Forest Meteorology, 356, 110175.

2. van Hateren, T. C., Jongen, H. J., Al-Zawaidah, H., Beemster, J. G., **Boekee, J.**, Bogerd, L., ... & Zwartendijk, B. W. (2023). Where should hydrology go? An early-career perspective on the next IAHS Scientific Decade: 2023–2032. Hydrological Sciences Journal, 68(4), 529-541.

1. Dai, Y., **Boekee, J.**, Schilperoort, B., ten Veldhuis, M. C., & Van de Wiel, B. J. (2023). Wind machines for frost damage mitigation: A quantitative 3D investigation based on observations. Agricultural and Forest Meteorology, 338, 109522.